

UCLA

UCLA Previously Published Works

Title

Stimulation of the hepatoportal nerve plexus with focused ultrasound restores glucose homeostasis in diabetic mice, rats and swine

Permalink

<https://escholarship.org/uc/item/3w48p6zz>

Journal

Nature Biomedical Engineering, 6(6)

ISSN

2157-846X

Authors

Cotero, Victoria
Graf, John
Miwa, Hiromi
[et al.](#)

Publication Date

2022-06-01

DOI

10.1038/s41551-022-00870-w

Peer reviewed



Published in final edited form as:

Nat Biomed Eng. 2022 June ; 6(6): 683–705. doi:10.1038/s41551-022-00870-w.

Stimulation of the hepatoportal nerve plexus with focused ultrasound restores glucose homeostasis in diabetic mice, rats and swine

Victoria Cotero¹, John Graf¹, Hiromi Miwa², Zall Hirschstein³, Khaled Qanud⁴, Tomás S. Huerta⁴, Ningwen Tai⁵, Yuyan Ding⁵, Kevin Jimenez-Cowell^{5,6}, Jacquelyn N. Tomai⁴, Weiguo Song⁴, Alex Devarajan⁴, Tea Tsaava⁴, Radhika Madhavan¹, Kirk Wallace¹, Evelina Loghin¹, Christine Morton¹, Ying Fan¹, Tzu-Jen Kao¹, Kainat Akhtar³, Meghana Damaraju³, Linda Barenboim³, Teresa Maietta³, Jeffrey Ashe¹, Kevin J. Tracey⁴, Thomas R. Coleman⁴, Dino Di Carlo², Damian Shin³, Stavros Zanos⁴, Sangeeta S. Chavan⁴, Raimund I. Herzog⁵, Chris Puleo^{1,✉}

¹General Electric (GE) Research, 1 Research Circle, Niskayuna, NY, USA.

²University of California, Los Angeles, Los Angeles, CA, USA.

³Albany Medical College, Albany, NY, USA.

⁴Feinstein Institutes for Medical Research, Manhasset, NY, USA.

⁵Yale School of Medicine, New Haven, CT, USA.

⁶German Cancer Research Center (DKFZ), Heidelberg, Germany.

✉ **Correspondence and requests for materials** should be addressed to Chris Puleo., puleo@ge.com.

Author contributions

V.C. performed chronic stimulation experiments in ZDF and DIO models, data analysis and short-term stimulation experiments involving chemical lesioning and in vivo blocking; H.M. performed the in vitro stimulation experiments and data analysis; Z.H., K.A., M.D., L.B. and T.M. performed in vivo electrical recording experiments and contributed to data analysis; K.Q., J.N.T. and W.S. performed swine model experiments and data analysis; T.S.H., A.D. and T.T. performed western diet model experiments; N.T., Y.D. and K.J.-C. performed rodent H/E clamp experiments; J.G. performed transcriptomic and metabolomic analyses, data presentation and statistical analysis across manuscript data; R.M. performed analysis of electrical nerve recording data; K.W., T.-J.K. and Y.F. installed, set-up and calibrated ultrasound equipment and contributed experimental results from the mechanical piston stimulation data; E.L. and C.M. assisted in sample collection, storage and analysis of DIO and ZDF biological samples; J.A., K.J.T., T.R.C., D.D.C., D.S., S.Z., S.S.C., R.I.H. and C.P. designed the research and experiments, performed data analysis, edited and co-wrote sections of the manuscript; C.P. wrote the manuscript, including the assembly of sections from the collaborating institutions.

Code availability

The source codes used for the data analyses of the study are available on request.

Competing interests

V.C., J.G., R.M., K.W., E.L., C.M., Y.F., T.-J.K., J.A. and C.P. are employees of General Electric and declare that GE has filed US and international patent applications describing methods, devices and systems for precision organ-based ultrasound neuromodulation. H.M., Z.H., K.Q., T.S.H., N.T., Y.D., K.J.-C., J.-N.T., A.D., T.T., K.A., M.D., L.B., T.M., K.J.T., T.R.C., D.D.C., D.S., S.Z., S.S.C. and R.I.H. have received research funding from GE to investigate the effects of ultrasound on metabolism. W.S. declares no competing interests.

Additional information

Extended data is available for this paper at <https://doi.org/10.1038/s41551-022-00870-w>.

Supplementary information The online version contains supplementary material available at <https://doi.org/10.1038/s41551-022-00870-w>.

Peer review information *Nature Biomedical Engineering* thanks Gin-Shin Chen, Harald Stauss and the other, anonymous, reviewer(s) for their contribution to the peer review of this work. Peer reviewer reports are available.

Reprints and permissions information is available at www.nature.com/reprints.

Abstract

Peripheral neurons that sense glucose relay signals of glucose availability to integrative clusters of neurons in the brain. However, the roles of such signalling pathways in the maintenance of glucose homeostasis and their contribution to disease are unknown. Here we show that the selective activation of the nerve plexus of the hepatic portal system via peripheral focused ultrasound stimulation (pFUS) improves glucose homeostasis in mice and rats with insulin-resistant diabetes and in swine subject to hyperinsulinemic-euglycaemic clamps. pFUS modulated the activity of sensory projections to the hypothalamus, altered the concentrations of metabolism-regulating neurotransmitters, and enhanced glucose tolerance and utilization in the three species, whereas physical transection or chemical blocking of the liver–brain nerve pathway abolished the effect of pFUS on glucose tolerance. Longitudinal multi-omic profiling of metabolic tissues from the treated animals confirmed pFUS-induced modifications of key metabolic functions in liver, pancreas, muscle, adipose, kidney and intestinal tissues. Non-invasive ultrasound activation of afferent autonomic nerves may represent a non-pharmacologic therapy for the restoration of glucose homeostasis in type-2 diabetes and other metabolic diseases.

The development of new tools to interface with and modulate the nervous system has been a long sought-after goal within the neuro-engineering field¹. Advances in these tools (for example, smaller and more energy-efficient electronics, and improved implant materials) have transformed neuroscience, and led to a better understanding of how the peripheral nervous system interacts with and coordinates cellular and physiological function within organ systems. A recent example has been the elucidation of the important role of the nervous system in sensing and regulating immune functions^{2–4}, including discovery of reflex-like neuroimmune pathways, such as the cholinergic anti-inflammatory pathway⁵. These discoveries have led to first-in-human trials⁶ in the emerging field of bioelectronic medicine, in which nerve stimulators are deployed to modulate organ function, even in diseases that have traditionally been deemed non-neurological disorders, such as rheumatoid arthritis and irritable bowel syndrome^{7–9}. These applications of nerve stimulation rely on the anatomically and physiologically specific roles that nerve reflexes play in maintaining homeostasis within organ systems^{8,10}. While pharmacological agents are developed to target specific molecular mechanisms, they lack anatomical and/or functional specificity, which often results in off-target effects and limit clinical use.

Despite the rapid advancement of the field of bioelectronic medicine over the last decade, substantial challenges remain for clinical translation^{7,8,10,11}. First, although electrical implants have become miniaturized, surgical implantation remains a risk compared with pharmaceutical alternatives. Historically, this has limited the patient populations in which bioelectronic medicines can be tested and applied. Second, non-implant-based and less-invasive peripheral nerve stimulation methods, such as transcutaneous electrical nerve stimulation (TENS) and transcutaneous magnetic stimulation (TMCS), have limited precision, delivering electromagnetic fields to large areas of tissue (that is, across multiple nerve fields), and are limited to relatively superficial stimulation depths (from millimetres to a few centimetres). Third, new technologies, such as magnetic nanoparticles¹² and opto-^{1,13} or sono¹⁴-genetics are potentially more precise in terms of stimulating smaller nerve fields but come with substantial translational hurdles due to the need for genetic modification

and/or nanoparticle injection. Technologies that minimize these risks while providing better control over the anatomical and spatial precision of the stimulated nerve fields are needed to further advance bioelectronic medicine and expand clinical translation and testing. Recently, we have demonstrated that precision (for example, mm-scale) and image-targeted pulsed ultrasound stimuli are capable of modulating peripheral nerve pathways^{11,15–19}. Within the spleen, peripheral focused ultrasound stimuli (pFUS) non-invasively activated the cholinergic anti-inflammatory pathways (CAP) and reduced cytokine output to the same extent as an invasive vagus nerve stimulator (VNS)¹⁵. Furthermore, while cervical VNS (that is, the stimulation of axons within the cervical implantation site innervating many organs) produced notable off-target effects in non-immune functions (including cardiovascular and metabolic markers), the targeted splenic pFUS did not¹⁵.

For decades, researchers have electrically stimulated brain–liver nerve pathways to better understand their function; however, past experiments have shown complex and conflicting effects on blood glucose levels and metabolism^{20–23}. One set of cervical VNS studies demonstrated that acute stimulation of afferent and efferent pathways innervating the liver caused severe hyperglycaemia in rodent models, without affecting the overall secretion of insulin and glucagon^{21,23}. This observed hyperglycaemia was associated with modulation of hepatic glycogenolysis and post-prandial hepatic glucose production. In contrast, chronic VNS in rodent models of diabetes resulted in notable weight loss and reduced hepatic glucose production, coinciding with an alteration in the parasympathetic tone²². In large animals, access to larger abdominal vagus nerve fibres (compared to rodents) enabled vagal stimulation within the abdominal cavity, rather than the cervical VNS, resulting in increased whole-body/non-hepatic glucose uptake and improved insulin sensitivity²⁰. Direct electrical stimulation of hepatic branches of the vagus nerve has yielded more conflicting results²⁴, where stimulation of hepatic branches with a 70 ms pulsed stimulus resulted in increased circulating glucose with decreased insulin levels, while 25 ms pulses resulted in increased glucose and insulin levels. Measures of liver glycogenesis and glycogenolysis demonstrated a local hepatic effect of VNS effect in these studies, which however were confounded by off-target effects on other metabolic organs, such as the pancreas.

Here we show that image-targeted pFUS at the porta hepatis (that is, the anatomical location of the hepatoportal nerve plexus) results in a reproducible lowering of hyperglycaemia in multiple rodent models of type-2 diabetes (T2D). Furthermore, chronic stimulation (that is, the application of pFUS for 3 min daily) results in increased glucose uptake and in glycogen accumulation in peripheral tissue (in particular, in skeletal muscle), and an overall improvement in glucose tolerance and insulin sensitivity. Stimulation at this site (known to contain glucose and metabolic sensory neurons) results in substantial improvement in measures of hypothalamic insulin signalling and glucose utilization, and is associated with the downregulation of markers of the hypothalamic neuropeptide Y (NPY) pathway. Chemical disruption or surgical disruption (that is, via resection) of the liver–brain nerve pathway blocked the pFUS effect on glucose tolerance, as did the local injection of a transient receptor potential ankyrin 1 (TRPA1)-specific ion-channel blocker before stimulation. TRPA1-dependence was also shown in *ex vivo* cultures of peripheral neurons exposed to ultrasound pulses, demonstrating the importance of this channel in the transduction of the ultrasound stimuli. The pFUS effect on glucose utilization was

demonstrated in rodents and swine using hyperinsulinemic-euglycaemic clamp (HEC). In the swine studies, image targeting to the porta hepatis and application of the pulsed stimuli were performed non-invasively (specifically, via pFUS pulses under the current United States Food and Drug Administration (FDA) limits for diagnostic ultrasound) using a clinically available ultrasound system. These data show that pFUS can be used for image-targeted and anatomically specific neuromodulation to modulate peripheral nerve activity through distinct classes of mechanically sensitive ion channels. When targeted to the liver–brain pathway, this non-invasive ultrasound stimulus prevents or reverses the onset of hyperglycaemia in diabetic models, and thus represents a tool for the potential clinical translation of bioelectronic medicines.

Results and discussion

We used non-invasive pFUS¹⁵ directed at the porta hepatis to modulate neurons within the hepatoportal plexus^{18,25–34} in several animal models of hyperglycaemia and type-2 diabetes (T2D; Fig. 1a and Supplementary Figs. 1–3). The stimulus parameters were based on the dose (that is, ultrasound frequency, pulse repetition period, pulse length and magnitude, and treatment duration) associated with maximal reduction of blood glucose in an acute rat model of hyperglycaemia^{15,18} (Supplementary Fig. 3). We first performed chronic testing of non-invasive pFUS stimulation in non-fasted ZDF (Zucker diabetic fatty) and DIO (diet-induced obesity) rodent models of T2D. Each animal underwent image-guided localization and marking of the porta hepatis, and then received once daily 3 min ultrasound treatments at this site over an extended period of 40 d (details of targeting and stimulation procedure in Methods).

Daily pFUS (Fig. 1b) prevented the onset of hyperglycaemia, attenuated hyperinsulinemia compared with sham-treated controls, and maintained blood glucose at levels comparable to non-diabetic animals in the ZDF rats (Fig. 1b(left); Sprague–Dawley (SD) naïve). Following 20 d of treatment, a subset of treated and sham cohorts were interchanged (Fig. 1b). pFUS decreased circulating glucose in the severely hyperglycaemic animals (previous sham controls), while cessation of treatment resulted in onset of hyperglycaemia within 3 d. No adverse pFUS-induced deviations of serum biomarkers were observed; instead, circulating levels of glucose, T4, cholesterol and amylase all stayed in the normal range compared with sham controls (Supplementary Fig. 4a). Furthermore, pFUS induced a decrease in serum cortisol levels (ZDF sham control: 384.7 ± 17.6 ng ml⁻¹; ZDF-pFUS: 97.6 ± 48.2 ng ml⁻¹; $P = 0.005$, $n = 5$ (Supplementary Fig. 5)). Daily stimulation in a lean Zucker (Fa/fa) control cohort did not result in glycaemic deviation or evidence of hypoglycaemia in non-diabetic controls (Supplementary Fig. 4b). Insulin measurements and homeostatic model assessment of insulin resistance (HOMA-IR) scores demonstrated significant improvement of insulin sensitivity in pFUS-treated ZDF rats (Fig. 1b(right), 1e and Supplementary Fig. 4c,d).

Similar results were also observed in the DIO model where pFUS treatment of hyperglycaemic animals reduced circulating blood glucose (Fig. 1c(left)) within days of treatment. This glycaemic improvement was significant (407.8 ± 14.2 mg ml⁻¹ reduction in glucose at study termination) and was sustained for at least 5 weeks. As with the

ZDF cohorts, pFUS-treated DIO animals showed reduced circulating insulin levels and improved HOMA-IR scores (Fig. 1c(right)). However, there were significant differences in pFUS-induced changes in circulating leptin, GLP, ghrelin and norepinephrine (NE) in the ZDF versus DIO cohorts (Fig. 1d). Leptin was reduced in both models after pFUS (ZDF sham control: 10.4 ± 4.2 ng ml⁻¹; ZDF-pFUS: 4.6 ± 1.8 ng ml⁻¹; DIO sham control: 2.7 ± 0.3 ng ml⁻¹; DIO pFUS: 0.72 ± 0.2 ng ml⁻¹). Circulating GLP was not altered in the ZDF model but increased in the pFUS-treated DIO animals (DIO sham control: 200.3 ± 16.9 pmol l⁻¹; DIO pFUS: 315.7 ± 33.8 pmol l⁻¹). Ghrelin was increased in the ZDF model (ZDF sham control: 36 ± 8.5 pmol l⁻¹; ZDF-pFUS: 52.8 ± 4 pmol l⁻¹) but decreased in the pFUS-treated DIO cohorts (DIO sham control: 43.5 ± 14.8 pmol l⁻¹; DIO pFUS: 6.6 ± 1.9 pmol l⁻¹). Circulating norepinephrine was increased in both models, but to a larger extent in the ZDF (ZDF sham control: 18.7 ± 3.4 pg ml⁻¹; ZDF-pFUS: 58.4 ± 4.8 pg ml⁻¹) versus the DIO (DIO sham control: 41.7 ± 5 pg ml⁻¹; DIO pFUS: 56.6 ± 2.9 pg ml⁻¹) animals.

Previous studies using invasive portal glucose infusions to activate the hepatoportal plexus have demonstrated transient enhancement of muscle glucose uptake^{34–36}. In these previous studies, enhanced glucose uptake in skeletal muscle was mediated by an insulin-independent/adenosine 5' monophosphate-activated protein kinase (AMPK)-dependent pathway, resulting in activation of GLUT4³⁵. Consistent with these previous observations, skeletal muscle samples from pFUS-treated cohorts in the ZDF model demonstrated an increase in AMPK and glucose transporter 4 (GLUT4) activity of $35.8 \pm 9.6\%$ and $65.7 \pm 20.2\%$, respectively, compared with sham controls (Fig. 1e; $P < 0.05$). Glycogen content of the terminal muscle samples was also altered after 4 weeks of daily pFUS, resulting in an increase of $91 \pm 22.3\%$ (Fig. 1e) in the pFUS-treated ZDF animals compared with sham controls. Unlike skeletal muscle, autonomic regulation of glucose uptake in the liver has been previously shown to affect the temporal variability of glycogen synthesis and gluconeogenesis, but not long-term glycogen content^{37–40}. Subsequent reports have shown that this is due to the liver's inherent autoregulatory mechanisms for glucose uptake and the interaction of nerve-mediated regulatory mechanisms with insulin and glucagon signalling³⁷. In this initial experiment, we could not rule out transient effects of pFUS on glucose uptake, storage or production in liver. However, the terminal samples collected did not show significant change in hepatic GLUT2 or AMPK activity, or glycogen content (Fig. 1e).

To further investigate the transient effects of pFUS, we next performed daily treatment on non-fasted ZDF animals while collecting samples for glycogen measurements at 2 h, 24 h and 14 d (post-ultrasound treatment) timepoints, and compared glycogen content in liver and skeletal muscle to sham controls. Supplementary Fig. 6a shows that as in the terminal samples shown in Fig. 1e, 14 d of ultrasound stimulation resulted in a significant increase in the glycogen content in skeletal muscle samples, an increase that was apparent at all timepoints, including after a single treatment. Again, the 24 h and 14 d liver samples showed no difference in glycogen content compared with sham controls. Supplementary Fig. 6b shows that the increase in muscle glycogen is associated with a reduction in glycogen synthase kinase-3 (GSK-3). In addition, increases in GLUT4 and AMPK in skeletal muscle were shown across all timepoints (2 h, 24 h and 2 weeks). No change in insulin receptor substrate 1 (IRS-1) phosphorylation was observed in muscle at 24 h and 14 d timepoints,

again supporting an insulin-independent pathway for the enhancement in muscle glucose uptake and glycogen formation³⁵. At the same time, liver samples showed no difference in GSK-3, IRS-1, AMPK or GLUT2 at 24 h or 2 weeks. However, elevated IRS-1 activity and decreased hepatic glycogen content was observed at the 2 h timepoint, again suggesting a role of the hepatic autonomic system in modulating the temporal variability of glycogen synthesis versus gluconeogenesis (in an insulin-dependent manner), but not the liver's long-term glycogen content³⁷.

In addition to enhancing glucose uptake and minimizing post-prandial glucose excursions, activation of hepatoportal nerve pathways and nutrient sensors have also been implicated in the regulation of food intake^{29,40-43}. Herein, at slowing of the overall rate of weight gain in pFUS-treated (red line) ZDF rats was observed, compared with their sham-stimulated littermates (blue line; Fig. 1f(left)). However, it is unlikely that the pFUS-induced glycaemic control was solely attributable to decreased food intake, as no significant change in food intake occurred during the first 2 weeks of treatment (Fig. 1f(right)) and weight gain still occurred despite the normalization of blood glucose throughout the 4 week study. The trend in weight gain for the DIO cohorts was similar (Fig. 1g(left)); however, the difference between pFUS and sham control cohorts was less pronounced compared with ZDF animals. In addition, while normalization of blood glucose occurred within days after applying pFUS, food intake was slightly higher during the first week of stimulation and pFUS did not result in a sustained decrease in food intake across the entire 4 week period.

To further demonstrate the importance of the glucose-lowering effect of the pFUS treatment, we next performed daily pFUS treatment on age-matched cohorts of ZDF animals for 10 d in combination with pharmaceutical agents, including metformin and liraglutide (details in Methods). Supplementary Fig. 7 shows that the ultrasound treatment provided significantly improved glucose levels at 10 d, even in the presence of these potent pharmaceuticals⁴⁴ when compared with the drug-alone controls. The addition of the pFUS treatment resulted in a $55.4 \pm 2.1\%$ and $56.6 \pm 3.4\%$ reduction in average glucose measures in the metformin and liraglutide co-therapy cohorts, respectively. This corresponded to a decrease in circulating glucose from 323.7 ± 17.3 to 180 ± 10.6 mg dl⁻¹ (for metformin alone), from 341.4 ± 13.7 to 150.7 ± 11.2 mg dl⁻¹ (for metformin+pFUS), from 267.7 ± 10.7 to 135.8 ± 11.3 mg dl⁻¹ (for liraglutide alone) and from 273.5 ± 5.9 to 116.8 ± 7.6 mg dl⁻¹ (for liraglutide+pFUS). These findings show that pFUS treatment of the hepatic nerve plexus added benefit by further lowering daily glucose levels, even in the presence of these potent pharmaceuticals.

Ultrasound stimulation of the hepatic nerve plexus reduces insulin resistance.

Next, glucose tolerance tests (GTTs; Fig. 2) were performed in both the rat ZDF (at age 65 d) and mouse western diet (WD) models of T2D. After a 12 h fast, animals underwent 3 min hepatic pFUS treatment under light anaesthesia (details in Methods). pFUS treatment resulted in significantly lower post-prandial plasma glucose levels, improved glucose tolerance and improved glucose excursion (area under the curve, AUC) compared with sham controls. In the ZDF model, a single ultrasound stimulation of 3 min was shown to improve both circulating glucose and insulin concentrations (Fig. 2a(i-iii)), resulting in improved HOMA-IR scores (Fig. 2a(iv) and Supplementary Fig. 8). Interestingly, although cessation

of the pFUS treatment resulted in renewed onset of hyperglycaemia in the ZDFs within 3 d during the daily treatment above (Fig. 1b(left)), three repeated daily stimulations provided no additional benefit when compared with the single pFUS stimulus in regard to GTT outcomes (Supplementary Fig. 8), further supporting the effectiveness of the ultrasound dose utilized herein.

Daily stimulation was also tested in a modified western diet-induced obesity (WD) mouse model (Fig. 2b(i–iv)). pFUS in the WD model resulted in the maintenance of significantly lower plasma glucose during GTT (Fig. 2b(i,ii) and Extended Data Fig. 1), lower insulin levels (Fig. 2b(iii) and Extended Data Fig. 1) and improved HOMA-IR (Fig. 2b(iv)) after 8 weeks of treatment compared with sham controls. Furthermore, the level of attenuation of hyperglycaemia and hyperinsulinemia during daily treatments in the WD mouse model was consistent at both 8 week and 16 week measurement timepoints, demonstrating effectiveness across the treatment period (Extended Data Fig. 1).

Hepatic pFUS modulates glucose uptake and utilization.

HECs were also performed in multiple rodent models of diabetes (DIO-streptozotocin (STZ)-diabetic and lean STZ-diabetic SD rats; overnight fasted and freely moving, 110 mg ml⁻¹ glucose clamp target using a 30 min insulin bolus of 25 mU kg⁻¹ min⁻¹, followed by 90 min of 15 and 10 mU kg⁻¹ min⁻¹ continuous insulin infusion; Fig. 3a(top),b(top), and Extended Data Figs. 2 and 3). The experiments were performed 24 h following 3 consecutive days of 3-min-duration pFUS treatment. The studies confirmed that pFUS stimulation in days before testing (see experimental timeline in Extended Data Figs. 2 and 3) resulted in improved glucose utilization. In both models, a notable increase in glucose infusion rate (GIR; Fig. 3a(bottom),b(bottom)) was measured compared with sham controls, consistent with the restoration of a more insulin-sensitive phenotype. Catecholamine, corticosterone and glucagon responses during the clamp were also measured in pFUS and sham cohorts (Extended Data Figs. 2 and 3). However, no sustained effect on systemic levels of hormones were apparent to completely explain the increase in glucose utilization (that is, GIR) throughout the clamp procedure. A delayed pFUS-induced rise in glucagon was observed in both animal models at only one timepoint during the clamp, which did not account for the overall differences in GIR already observed from the beginning of the clamp procedure (Extended Data Figs. 2 and 3). As with data presented in Fig. 1e, the effect on GIR in the lean STZ-SD (T1D) model (with longstanding hyperglycaemia and absent endogenous insulin secretion) further suggests that the pFUS effect is at least partially mediated by insulin-independent pathways.

To further translate our findings and specifically determine whether the acute effect of pFUS on glucose utilization was limited to rodents, we proceeded to perform pFUS during HECs in a large-animal model (swine). pFUS was performed immediately upon achieving steady state (110 mg dl⁻¹ glucose) using a 0.5 mU kg⁻¹ min⁻¹ continuous insulin infusion (Fig. 3c(top) and Extended Data Fig. 4). The ultrasound stimulation resulted in an almost immediate trend towards increased GIR (Fig. 3c(bottom)) compared with the sham-stimulated controls. The GIR was shown to increase ~20% by 30 min post-ultrasound.

The large-animal experiments were performed at ultrasound parameters designed to achieve a mechanical index (MI) of ~ 1.77 , with a derated spatial-peak time-average intensity (Ispta.3) of $\sim 503 \text{ mW cm}^{-2}$ at the $\sim 65 \text{ mm}$ depth of the hepatoportal plexus (to remain consistent with the Ispta.3 of $\sim 581 \text{ mW cm}^{-2}$ at the $\sim 5 \text{ mm}$ target depth in the rats). pFUS in the swine model was performed using the clinical GE LOGIQ E10 system with C1-6 abdominal probe. Image guidance for locating the hepatoportal plexus (Extended Data Fig. 4) was accomplished using the research-mode configured elastography setting, which enabled initial targeting using B-mode imaging, and then push-button activation of the pFUS pulses (see Methods for pulse parameter details). The chosen stimulation parameters are within current FDA guidance for diagnostic ultrasound (that is, $<720 \text{ mW cm}^{-2}$ Ispta.3 and $<1.9 \text{ MI}$). Both use of a clinical system capable of targeting pFUS stimulation to specific neuro-anatomical locations and use of relatively low temporal average ultrasound intensity represent an encouraging step towards clinical translation of pFUS therapy.

The hepatic pFUS effect depends on intact liver–brain nerve pathways.

To ascertain whether intact neuronal connections are necessary for metabolic effects of pFUS stimulation, we performed acute ultrasound/GTT experiments after either chemical blockade or physical dissection of the vagus (VGX) and/or the dorsal root ganglion/spinal (DRGX) neuronal pathways to the liver (Fig. 4a). Chemical blocks were performed at the level of the intermediolateral (IML) and the nucleus of the solitary tract (nucleus tractus solitarius, NTS). Overnight-fasted, lightly anaesthetized ZDF rats received injections of a 2% lidocaine solution to the respective target site, and then underwent 3 min pFUS stimulation followed by subsequent glucose tolerance testing. Injection of lidocaine at either site attenuated the pFUS glucose-lowering effect previously observed in ZDF animals, as measured by GTT after a single ultrasound stimulation (Fig. 4b). Blockade of both vagal and spinal mediated pathways at the level of the NTS completely abolished the ultrasound effect on plasma glucose, while blockade of spinal (but not vagal) pathways within the IML resulted in partial attenuation (Fig. 4b).

To rule out any potential pharmacologic effects of lidocaine injections on hormonal responses, we performed confirmatory nerve dissection studies with acute hepatic branch vagotomy and transection of the intermediolateral spinal cord (at the T1 vertebrae level), which both reproduced the attenuation of the glucose-lowering pFUS effect in ZDF (Fig. 4c). Cutting both the vagal (VGX) and IML spinal cord completely abolished the pFUS effect, while blocking only the vagal pathway resulted in partial attenuation (Fig. 4c). These results support previous demonstrations that hepatoportal sensor signalling occurs through both vagus and IML-mediated pathways^{40,43,45–51}. Previous studies using portal glucose infusion and clamps have shown that complete liver denervation entirely blocks the extra post-prandial glucose uptake triggered by hepatoportal glucose sensors, while vagotomy decreased the glucose uptake by $\sim 40\%$ ³⁷. Herein, VGX resulted in a $40.7 \pm 12.6\%$ reduction in the pFUS hepatoportal stimulus effect, while spinal/IML block inhibited the effect almost entirely ($90.7 \pm 18.9\%$).

Furthermore, to characterize central pFUS effects on important molecular components of known nutrient sensing and insulin signalling pathways, we measured insulin receptor

substrate 1 (IRS-1), glucose transporter GLUT4, and glucose-6-phosphate changes in hypothalamic tissue and peripheral blood. In the absence of the chemical blockade, a single pFUS treatment resulted in a significant increase in hypothalamic catecholamine concentrations, reduction in NPY, and increases in IRS-1 and GLUT4 activities (Fig. 4d(top)). Both IML and NTS block centrally attenuated the catecholamine and blocked the NPY response to pFUS (Fig. 4d(top)). Interestingly, there was also a differential effect of IML versus NTS block across catecholamines, with complete inhibition of the pFUS effect on norepinephrine and epinephrine (Epi) after IML block, but only partial attenuation of the catecholamine effect after NTS block. The NTS block completely inhibited the pFUS effects on hypothalamic IRS-1 and GLUT4 activities, while the IML block had no influence on pFUS-induced GLUT4 modulation (Fig. 4d(top)). pFUS did not change hypothalamic AMPK activity (that is, a marker of glucose-inhibited neuron activity); however, blockade of either the IML or NTS resulted in increased AMPK phosphorylation. Peripherally, the largest effect of the NTS block on pFUS responses was on circulating plasma norepinephrine, while IML block resulted in significant changes in circulating glucagon (Fig. 4d(bottom)).

In agreement with these acute measures, terminal hypothalamic samples from ZDF animals treated with pFUS for 20 consecutive days (glucose values reported in Fig. 1b(left)) also demonstrated significant increases in hypothalamic catecholamine levels (NE) (ZDF sham control: 140.9 ± 52.2 ng mg⁻¹; ZDF-pFUS: 273.6 ± 52.9 ng mg⁻¹, $n = 5$, $P < 0.05$), reduction in NPY (sham control: 44.8 ± 14.8 ng mg⁻¹; ZDF-pFUS: 3.3 ± 0.9 ng mg⁻¹, $n = 5$, $P < 0.05$) and increase in IRS-1 and GLUT4 activities compared with sham controls (Fig. 4e). pFUS-induced alterations in other hypothalamic neurotransmitters were consistent with known regulatory or co-modulatory connections to NPY-expressing neurons (Fig. 4e)⁵²⁻⁵⁵. These included increased GABA^{56,57}, decreased glutamate⁵⁸⁻⁶⁰ and increased BDNF^{42,61} concentrations. pFUS modulated central K_{ATP} activity⁶² but not AMPK⁶³, and resulted in modulation of important molecular components of nutrient sensing pathways (for example, IRS-1, GLUT4 and glucose-6-phosphate)⁶⁴⁻⁶⁶.

Hepatic vagotomy was also performed on the DIO-STZ-diabetes model (overnight fasted, freely moving, 110 mg ml⁻¹ target glucose during a 15 mU kg⁻¹ min⁻¹ continuous insulin infusion; Fig. 4f(left, right)). As in Fig. 2, the experiments were performed 24 h following 3 consecutive days of 3-min-duration pFUS treatment. However, in this experiment the clamp was performed 17-18 d following hepatic vagotomy. In these insulin-resistant animals that underwent vagotomy, the pFUS effect on GIR previously observed (see Fig. 2) was abolished. Again, these data agree with previous portal glucose infusion and euglycaemic clamp reports, where hepatic parasympathetic effects were shown to be responsible for modulating extrahepatic tissue glucose clearance (including insulin-independent pathways to skeletal muscle and other peripheral tissues)³⁵, while net hepatic glucose uptake was dependent on functional sympathetic (and not parasympathetic) innervation of the liver and insulin signalling^{37,67,68}.

To further validate pFUS modulation of hypothalamic pathways, we also prepared terminal hypothalamic samples from the ZDF-pFUS and sham cohorts shown in Fig. 1 for paraffin embedding and histochemical analysis (Extended Data Fig. 5). pFUS stimulation at the

porta hepatis was found to alter cFOS expression across several hypothalamic nuclei (Extended Data Fig. 5a,b), including an increase in cFOS+ neurons within the lateral arcuate nucleus (ARC, the site of NPY-inhibited glucose-excited neurons⁶⁹), and in sites of known anorexigenic/catabolic ARC projections^{69–72} to the ventromedial nucleus and paraventricular nucleus (PVN). In agreement, brain-derived neurotrophic factor (BDNF) staining (Extended Data Fig. 5c) showed significant pFUS-induced increase in the anorexigenic protein at these hypothalamic sites, and areas of the hippocampus shown to affect the memory of food intake and feeding motivation^{42,61}. Additionally, GLUT4 staining demonstrated increased translocation in pFUS-versus sham-stimulated ZDF animals (Extended Data Fig. 5d). GLUT4 is primarily expressed in glucose-excited neurons, which are known to respond to insulin receptor signalling as a result of increased insulin, leptin or amino acids associated with feeding⁷³. Furthermore, these hypothalamic GLUT4 neurons have been shown to modulate the glucagon counterregulatory response and are necessary to integrate hormonal and nutritional cues to achieve glucose homeostasis.

Addition of these histochemical and ELISA-based profiling data regarding the hypothalamic response to the pFUS treatment now points towards modulation of glucose-sensitive neural pathways^{49,62,63,66,69,73}. To investigate further, we next obtained electrophysiological recordings from hypothalamic neurons during glucose infusion, with or without pFUS stimulation (Fig. 5a–e). Hepatoportal pFUS modulated firing activity of glucose sensing, but not of glucose-insensitive neurons in the PVN (Fig. 5b(top, middle, bottom) and Supplementary Fig. 9). These measurements were obtained after intraperitoneal (i.p.) administration of glucose (20% glucose via inserted catheter) before ultrasound, which raised plasma glucose in both stimulated (+pFUS) and unstimulated (–pFUS) animals (Fig. 5c). In the absence of pFUS, i.p. glucose resulted in decreased firing rates of glucose-inhibited (GI) and increased activity of glucose-excited (GE) neurons (Fig. 5d,e; green bars). Under the same conditions, pFUS at the porta hepatis site resulted in attenuation of the glucose-induced firing rate change in GE, but not in GI neurons (Fig. 5d,e; yellow bars). Glucose-excited pathways have previously been shown to be critical for the initiation and maintenance of signals of energy sufficiency⁷⁴, with increased activity and firing rates resulting in increased energy expenditure^{41,75,76} and decreased food-seeking behaviours⁴¹. In addition, GE neurons have been found to be hyper-responsive in the db/db leptin receptor deficient and T2D model^{62,65,66}. In agreement with these previous findings, the circulating glucose concentrations of the pFUS-stimulated group were reduced compared with the unstimulated controls (Fig. 5c). This suggests that the hepatoportal pFUS stimulus affects the ratio of GE-versus GI-neuronal activation after a glucose injection through modulation of afferent liver–brain pathways.

The pFUS effect depends on the activity of mechanically activated ion channels.

We have previously shown that low-intensity mechanical ultrasound stimuli are capable of site-specific nerve modulation in both in vivo and in vitro models^{11,15–19}. Here, the mechanical origin of ultrasound neuromodulation was further confirmed using a purely mechanical stimulus (that is, replacing the ultrasound transducer with a mechanical piston-based stimulator; Supplementary Fig. 10), and demonstrating the dependence of ultrasound nerve activation on specific families of mechano-sensitive ion channels^{77,78} (Fig. 6a–e and

Supplementary Fig. 11). Three-dimensional (3D) in vitro cultures of dorsal root ganglia sensory neurons were activated (as measured by calcium indicator dye) using ultrasound pulse parameters and pressures that correspond to those from our in vivo experiments^{18,79}. Blocking of *N*-type calcium channels (ω -conotoxin) or voltage-gated sodium channels (tetrodotoxin) did not attenuate the response to pFUS (Fig. 6d). In contrast, blockade using a non-selective mechano-sensitive ion-channel blocker (that is, GxMTx4) or a specific blocker of transient receptor potential (TRPA1; that is, HC-030031) channel inhibited the pFUS effect (Fig. 6d). To determine whether TRPA1 was also required to achieve the glucose-lowering effect of hepatic pFUS in vivo, GTT studies were repeated after a single local injection of the specific TRPA1 blocker (HC-030031; 8 mg kg⁻¹) at the porta hepatis in a fasted ZDF rat. Confirming the important contribution of this channel, blocking TRPA1 indeed abolished the ability of pFUS treatments to lower blood glucose levels during GTT (Fig. 6e). It is noteworthy that ion channels within the TRP family are expressed on afferent neurons and have been reported to be required for functional glucose and metabolite sensing^{80–84}. Furthermore, it was previously shown that activation of TRPA1 (target of HC-030031) by allyl isothiocyanate improves glucose uptake and insulin signalling in multiple models of T2D by an unknown mechanism⁸⁵, while ablation of TRPV1 and TRPA1 expression (targets of GxMTx4) results in severe insulin or leptin resistance^{82,86}.

Longitudinal multi-omic profiling during pFUS treatment.

To better characterize the systemic response to daily hepatportal pathway pFUS stimulation, we proceeded to perform multi-omic profiling of different metabolic tissues by RNA-seq and metabolomic analyses. For this purpose, we included samples from liver, intestines, kidney, adipose, muscle, pancreas, hypothalamus and plasma in the ZDF and DIO models (Figs. 7 and 8, and Supplementary Figs. 12–20). Tissue samples were processed and analysed by untargeted metabolomics⁸⁷ (plasma and liver) and gene expression profiling^{88–92} (full transcriptome RNA sequencing of all tissues) after 3 d, 4 weeks and 7 weeks of 3 min d⁻¹ pFUS treatment (Supplementary Fig. 12). After the full 7 weeks of pFUS-induced glycaemic regulation (i.e., Fig. 1), significant alteration in gene expression was observed in all measured tissues as compared with sham controls (Fig. 7a,b), with 27.5% (ZDF model $P = 4.1 \times 10^{-4}$) and 28.8% (DIO $P = 1 \times 10^{-10}$) of these previously identified as diabetes risk genes. The top 20 modified diabetes-related genes show notable differences in pFUS effect between the DIO and ZDF models (Fig. 7c,d). Genes most broadly affected across tissues in the ZDF model (Fig. 7c) included the gene encoding Bmal1 (Arntl, endogenous circadian clock gene associated with suppression of diurnal variation in circulating glucose⁹³) and insulin receptor substrate 2 (Irs2). Leptin receptors are present on circadian clock neurons, and deficiencies in leptin signalling (such as those in the ZDF model) are known to affect central clock function^{94–96}. Furthermore, dysregulation of the peripheral circadian transcription factor Bmal1 is associated with altered expression of carbohydrate-regulating proteins (including Irs2⁹⁷) and metabolic dysfunction. The most broadly pFUS-impacted genes in the DIO model (Fig. 6d) include regulators of hepatic glucose metabolism, such as Glut 2, glucokinase and the ATP-binding sulfonyl receptor subunit Sur1⁹⁸, which showed functionally relevant expression changes. In the top 20 pFUS-altered diabetes genes, changes associated with intestinal tissue were more prominent in the ZDF model, while an increased number of affected genes was associated with liver

tissue in the DIO model. The ZDF model is characterized by intestinal enlargement (driven by increased food intake), and elevated biomarkers of insulin resistance within intestinal epithelial cells⁹⁹. In contrast, the DIO model is characterized by fat accumulation, which leads to inadequate fatty acid oxidation, and accumulation of free fatty acids in the liver¹⁰⁰. The unique effects of pFUS in the DIO versus the ZDF models suggest that activation of hepatoportal pathways and modulation of hypothalamic metabolic coordination hold therapeutic potential across multiple risk and pathogenic factors involved in T2D.

Gene sets (Fig. 7e) enriched in the hypothalamic/brain samples by pFUS included those associated with synaptic reorganization and altered voltage-gated potassium channel activity (in agreement with results shown in Figs. 1 and 4). In liver, gene sets enriched by pFUS included those associated with the MYC pathway (known to activate multiple glucose utilization enzymes¹⁰¹) and fatty acid/bile acid metabolism (Supplementary Figs. 13–15). In the intestines, gene expression hallmarks of improved nutrient/vitamin transport and metabolism were apparent; these included notable changes to glycolytic and gluconeogenic gene sets, and markers of improved mitochondrial function. In adipose tissue, markers of suppressed lipolysis were downregulated by pFUS (for example, mTORC1 signalling¹⁰²), and reduction in adipogenic gene sets were observed in liver, intestinal, pancreatic and muscle samples.

By day 3, pFUS-treated ZDFs exhibited expression signatures of an increased capacity for hepatic glucose uptake (that is, *Slc2a2*) and glycogen storage (that is, *Gys2*; *Pygl*), with a decrease in gluconeogenesis (that is, *G6pc*; Fig. 8a and Supplementary Fig. 14b). These signatures of improved glucose metabolism were accompanied by reduced expression of enzymes that catalyse glycerolipid biosynthesis, and upregulation of enzymes that catalyse fatty acid oxidation. The signatures of improved fatty acid oxidation continued through the 4- and 7-week timepoints after hyperglycaemia was already resolved. Metabolomic signatures within the liver and serum validate these transcriptomic observations. Circulating free fatty acids were reduced within 3 d of treatment, and the improvement in dyslipidemia was apparent across fatty acids of all chain lengths and degree of saturation (Fig. 8a,b, and Supplementary Figs. 15b and 16). Within the liver, tricarboxylic acid (TCA) cycle metabolites were decreased, further supporting renewed capability to take up and utilize circulating fatty acids. In addition, circulating 1,5-anhydroglucitol (a metabolite whose reabsorption in the renal tubules is inhibited during glucosuria¹⁰³) concentrations were increased following treatment—a signature of re-established glycaemic control. These circulating biomarkers were also accompanied by increased hepatic concentrations of gluconeogenic precursors (PEP and 3-phosphoglycerate), further validating the decreased expression of gluconeogenic enzymes in the pFUS-treated rodents.

By week 4, additional signatures of the pFUS reversal of metabolic dysfunction were apparent, including hepatic and circulating signatures of improved bile acid and vitamin metabolism¹⁰⁴ (Figs. 7c and 8a,b, and Supplementary Fig. 17). Supplementary Figs. 18–20 contain further evidence of broad pFUS-induced modulation of whole-body metabolism, including modulation of circulating sphingomyelin and ceramide concentrations (lipids associated with insulin resistance and pancreatic beta cell function¹⁰⁵; Supplementary Fig. 18) and reduction in circulating markers of diabetes-induced renal impairment

(phosphatidylcholine and lysophospholipids¹⁰⁶, Supplementary Figs. 19 and 20). These supporting whole-body measurements confirm that the nerve-mediated effects of hepatic pFUS (Figs. 1–6) exert far-reaching potent effects re-establishing metabolic homeostasis across multiple metabolically relevant organs that should be investigated further as a potential non-pharmaceutical treatment in T2D.

Outlook

Our anatomically precise pFUS neuromodulation method¹⁵ enabled daily activation of the hepatoportal plexus and glucose sensing pathway^{29,31,34,35,67} without the need for invasive portal clamps and infusions. Non-invasive stimulation of the hepatic nerve plexus was shown to activate neuronal liver–brain pathways utilized by the body to enhance insulin sensitivity, glucose uptake and energy substrate utilization^{27,28,31,43,55,58,67,107}. Our studies uncovered a critical role of TRPA1-positive nerve fibres in the transmission of information about portal glucose levels in this process. The pFUS-induced effect was found to be dependent on vagus nerve and sympathetic spinal afferent-mediated communication to the hypothalamus, ultimately inhibiting the central NPY system⁵². The resulting hypothalamic modulation of autonomic output to multiple organs resulted in sustained glycaemic control in multiple animal models of impaired glucose metabolism and diabetes. These outcomes are in agreement with previous reports that utilized invasive portal glucose injections to activate hepatoportal glucose and nutrient sensors^{26,29–35}. However, there have previously been no non-invasive methods with which to activate these neural pathways remotely and study their effect across the metabolic system. Here, pFUS activation of these pathways enabled testing and validation in three different species. pFUS stimulation in a large-animal model was performed using a clinical ultrasound system with pulse parameters within current FDA safety limits¹⁵, which will permit clinical translation of this exciting new technology and testing in a clinical context.

Despite the non-invasive nature of pFUS stimuli and potential benefits compared with traditional implant-based approaches to neuromodulation, some translational challenges will need to be addressed for clinical use. Currently, ultrasound imaging is practised by technicians and physicians trained on manual handling and use of the ultrasound probe and system software to achieve quality images and image-based diagnostic measurements. Unlike pharmaceutical treatments or implant-based therapies (both of which enable therapy to take place at home and without supervision), ultrasound neuromodulation tools based on current clinical systems would hinder at-home use, daily application of the therapy or cost-effective clinical testing across large cohorts of patients. However, low-cost wireless ultrasound systems are now available commercially¹⁰⁸. Moreover, wearable ultrasound probes have minimized the need for manual handling of the probe during use¹⁰⁹, and automated anatomical target detection software is now available to enable target tracking in real time using convolution neural-network models¹¹⁰. These advances may enable the development of novel wearable ultrasound systems that can be applied by unskilled users, and further enable use across clinical applications and settings.

Despite our comprehensive datasets in the rodent models of T2D (that is, ZDFs and DIOs) that clearly demonstrate therapeutic nerve-mediated pFUS modulation of metabolism in

the disease state, questions remain. For example, while the variability in GIR between pFUS and sham-stimulated animals remained low in the DIO T2D model (Fig. 3a; that is, consistent with the results across other metabolic measures in T2D models in Figs. 1, 2, 4, 7, and 8), variability was higher in the insulinopenic STZ-T1D rat model (Fig. 3b). Other pharmaceutical-based hypothalamic neuromodulation therapies have also recently demonstrated dependence on an intact insulin pathway to achieve long-lasting versus transient effects on glucose utilization^{111,112}, suggesting that the hypothalamic nerve pathways modulate and refine, but do not replace tissue response to insulin. These results in the T1D model are informative, but do not take away from the potential impact that pFUS may have in T2D models and applications. In addition, while the nerve resection and lidocaine blocking data (Fig. 4) clearly demonstrate the importance of hypothalamic sensory pathways on the effect of hepatoportal pFUS, our work does not yet rule out other contributing effects, including activation of neural reflex or neuroendocrine-mediated effects between the liver and other organs (such as the pancreas)¹¹³.

Both the previous pharmaceutical-based hypothalamic neuromodulation therapies^{111,112} and our pFUS treatment tests in naïve/non-diabetic rodents (Supplementary Fig. 4b) demonstrate that these hypothalamic neural effects on peripheral glucose metabolism are dependent on the current physiological state of the animal (for example, onset of glucose intolerance and/or insulin resistance). That is, pFUS treatment in an animal in a state of normal glucose levels and insulin sensitivity does not result in a further decrease in circulating glucose into hypoglycaemia values (Supplementary Fig. 4b). This may explain the larger variability seen in the GIR values in the healthy swine (Fig. 3c) compared with the T2D model (Fig. 3a). Further supporting this, in healthy swine the pFUS effect was observable only at the steepest part of the GIR versus IIR curve (Extended Data Fig. 4b), and there was no pFUS effect at saturating insulin concentrations or sham controls (Extended Data Fig. 4e). Again, this suggests that the hypothalamic neural effects are dependent on the physiological state of the animal, and levels of circulating glucose and insulin.

These data further support decades of previous work using traditional metabolic assays (such as portal clamps) that have established that neurons within the hepatoportal plexus are activated by transient glucose concentration differences across the hepatic portal vein and hepatic artery, in a concentration-dependent manner^{25,26,29–37,45–48,114,115}. As with the T1D model results, the additional variability in the swine model dataset does not detract from the robust effect of pFUS in our T2D datasets; rather, it highlights the complex interactions between the hypothalamic afferent nerve inputs and the metabolic hormone signals traditionally associated with glucose and energy regulation (insulin and glucagon). Importantly, further development of the pFUS toolkit will allow testing of these interactions in humans, which thus far has been limited by the invasiveness of portal clamps, implanted electrical stimulators, and newer nanoparticle and optogenetic technologies. The robust effects hepatoportal pFUS had on the T2D models studied herein suggest that the hypothalamic role in integrating metabolic sensory neuron versus hormonal signals is important and justifies additional investigation.

Our transcriptomic and metabolomic datasets (Figs. 7 and 8, and Supplementary Figs. 12–20) clearly demonstrate pFUS-induced shifts in overall metabolism that would not be

expected in the T2D models without treatment⁸⁷, including improvements in fatty acid, cholesterol, vitamin and bile acid metabolism. Whether each of these improvements is a direct result of pFUS neuromodulation of nerve pathways that directly affect fat, cholesterol, vitamin and bile acid metabolism, or is simply an indirect result of improved glycaemic control and hormone levels remains an important question for further investigation. Ultimately, the efficacy, safety and duration of glycaemic reduction found using pFUS treatment in clinical trials compared with current pharmaceutical treatments for T2D, will dictate utility in clinical practice.

In summary, our findings confirm that liver–brain neural pathways play an important role in maintaining whole-body glucose homeostasis and that non-invasive portal focused ultrasound stimulation represents an exciting new treatment modality to alter whole-body glucose metabolism and restore glucose homeostasis. We speculate that this new tool could be used as a non-pharmaceutical adjunct or even alternative to current treatments of diabetes.

Methods

Ultrasound stimulation.

1.1 MHz single-element FUS (rodent models).—The 1.1 MHz single-element focused ultrasound system (Supplementary Fig. 2a) is composed of a signal generator (Model 33120A, Agilent Technologies), an RF power amplifier (Model 350L, Electronics & Innovation) and a 1.1 MHz focused single-element ultrasound transducer (Model H102, Sonic Concepts). The transducer is connected to the output of the power amplifier using a matching network (Model H102, Sonic Concepts). The transducer element is 64 mm in diameter and has a 63.2 mm radius of curvature, with a 20-mm-diameter hole in the centre into which a small imaging transducer can be inserted for image guidance (Supplementary Fig. 2b). The transducer is acoustically coupled to the animal through a 6-cm-tall plastic standoff cone filled with degassed water.

The nominal settings of the waveform (Supplementary Fig. 3a (right)) are listed below:

- 1.1 MHz carrier
- 135 mV pk-to-pk signal generator amplitude
- 150 μ s pulse duration
- 5 Hz pulse repetition frequency

The acoustic performance of the system was characterized at an ISO/IEC 17025:2017 accredited laboratory (Acertara Acoustic Labs). Under the above settings, three separate systems were characterized, producing an MI of 1.79 ± 0.10 (mean \pm s.d.), a derated peak negative pressure, $p_{r.3}$ of 1.87 ± 0.11 MPa, a derated spatial-peak pulse-average intensity, $I_{sppa.3}$ of 125.7 ± 15.0 W cm^{-2} and an $I_{spta.3}$ of 94.3 ± 11.2 mW cm^{-2} .

Good linearity (0.9947 R²) of MI was observed over an amplitude range from 100 mV pk-to-pk to 200 mV pk-to-pk. Therefore, acoustic output can reasonably be linearly extrapolated to other amplitudes, pulse durations and pulse repetition frequencies (Supplementary Fig. 3b). The simulated pressure profile has a full width half maximum

amplitude of 1.8 mm laterally and 6 mm in the depth direction using Field II^{116,117} (Supplementary Fig. 3a). The -6 dB diameters at the peak were measured to be 1.45 ± 0.02 mm in the X scan axis and 1.46 ± 0.02 mm in the Y scan axis at the accredited laboratory. The width and depth of the ultrasound focal zone adequately covered the width and depth of the porta hepatis (that is, the size of the portal vein and hepatic artery at the entrance to the liver)¹¹⁸.

Ultrasound system and parameters used during electrophysiology and nerve recording.—The focused ultrasound system used for recording experiments was composed of a signal generator (Model 33120A, Agilent Technologies), an RF power amplifier (Model 350L, Electronics & Innovation) and a custom-made 2.5 MHz focused single-element ultrasound transducer. The transducer element is 19 mm in diameter and has a 25.4 mm radius of curvature. The transducer is connected directly to the output of the power amplifier without a matching network. The transducer is acoustically coupled to the animal using ultrasound gel without a standoff cone.

The nominal settings of the waveform for this system are listed below:

- 2.5 MHz carrier
- 300 mV pk-to-pk signal generator amplitude
- 120 μ s pulse duration (300 carrier cycles)
- 5 Hz pulse repetition frequency

Image target identification methods.—The portal vein of the rat liver was identified using an ultrasound imager. Two methods were employed to identify the target and position of the focused ultrasound transducer. The first method involved placing an ultrasound transducer directly on the skin, identifying the location of the portal vein and removing the ultrasound imaging probe before placing the focused ultrasound transducer in the same location. In this manner, a high-frequency probe (Model L8-18i linear probe, GE Healthcare) was used to provide high-resolution imagery consisting of B-mode imaging where the target was identified by changes in contrast (Supplementary Fig. 2c, left) as well as colour Doppler imaging where the target was identified by the pulsation of blood flow in the portal vein (Supplementary Fig. 2c(right)). The second method involved placing an ultrasound transducer through the opening in the centre of the focused ultrasound transducer while stimulation was being applied. In this manner, a lower-frequency probe (Model M3S phased-array probe, GE Healthcare) was used to obtain images at depth through the 6-cm-tall plastic standoff cone water coupling cone and target identification was obtained by observing changes in contrast.

GE LOGIQ E10 and C1-6 (convex) probe (swine model).—The LOGIQ E10 used in the swine model has identical hardware and base software to the commercially available diagnostic imaging system. The operational mode of the ultrasound system is based on the shear wave elastography (SWE) mode.

The software resource parameter files for the swine-specific ultrasound systems have been configured in research mode to provide the following operational features:

- Configure the SWE push-pulse to produce a single focused transmit beam compared with multiple spatially separated simultaneously transmitted focused beams implemented in the diagnostic SWE mode
- Configure the SWE push-pulse to produce a single focused transmit beam at a fixed depth compared with a variable depth implemented in the diagnostic SWE mode
- Configure the SWE push-pulse waveform to transmit single pulses at a faster pulse repetition rate compared with multiple-pulse bursts at a slower pulse repetition rate implemented in the diagnostic SWE mode
- Configure the SWE push-pulse waveform to a different acoustic MI within the FDA recommendations for ‘Track 3’ submissions compared with the current MI implemented in the diagnostic SWE mode

The configuration was verified by an independent party (Acertara Acoustic Laboratories) by measurement of acoustic output and probe temperature. Systems were verified to conform with the applicable standards for diagnostic ultrasound. Acoustic output was measured in accordance with IEC Standard 60601–2-37: Edition 2.1 2015–06, IEC Standard 62359: Edition 2.1 2017–09 and the FDA recommendations for ‘Track 3’ submissions. Probe temperature was measured in accordance with IEC Standard 60601–2-37: Edition 2.1 2015–06 and IEC Standard 60601–2-5: Edition 3.0 2009–07.

pFUS pulse settings were chosen as follows:

- 2.28 MHz carrier frequency
- 200 μ s pulse length
- ~3.7 Hz pulse repetition rate

Rat models of T2D.

ZDF rat model.—ZDF rats spontaneously develop T2D as a result of a missense mutation (fatty, fa) in the leptin receptor gene (*Lep^r*) and develop moderate hyperglycaemia spontaneously as a result of the insulin resistance and pancreatic insufficiency. Notably, the ZDF rat is profoundly hyperinsulinemic—a demonstration of the state of insulin resistance—before the onset of hyperglycaemia, similar to human diabetics, making this model a valuable tool in the study of T2D.

Adult male ZDF rats (Charles River) were ordered for arrival before 8 weeks of age. All animals were maintained on a high-caloric rodent chow (Purina 5008), and provided with water ad libitum. All rats were housed at 25 °C on a 12 h light/dark cycle and acclimatized with handling for 1 week before experiments were conducted to minimize potential confounding results from stress-induced hormonal fluctuations (for example, cortisol activation of the hypothalamic-pituitary-adrenal axis) capable of altering metabolic pathways. After 8 weeks, ZDF rodents began to exhibit rapid development of the diabetic

phenotype and were then separated into either sham control or pFUS treatment groups for acute oral glucose tolerance tests (OGTT; Fig. 2) or chronic (Fig. 1) ultrasound stimulation.

DIO rat model.—The DIO rodent model makes use of a high-fat/high carbohydrate diet to induce obesity and insulin resistance. Following development of obesity, low-dose STZ was used to induce a moderate level of pancreatic beta cell death (through alkylation of DNA in the islet cells), which impairs insulin secretion similar to that seen in later stage T2D. Adult male Sprague–Dawley rats (Charles River) were ordered to arrive at 8 weeks of age. Upon arrival, animals were placed on a high-fat diet (45% kcal as fat; Research Diet, D12451) and maintained consistently for 8 weeks. Following 8 weeks of a high-fat diet, rats were treated with STZ (30 mg kg⁻¹ in 0.1 M citric acid buffer, pH 4.5 i.p.). Diabetes was confirmed 96 h following STZ injection by evaluating blood glucose levels using a handheld glucometer (Freestyle Freedom Lite; Abbot Diabetes). Rats having blood glucose levels ≥ 280 mg dl⁻¹ (11.1 mM) were considered to be diabetic. Those animals which failed to develop hyperglycaemia were labelled as diet resistant and kept on study as a control.

All procedures performed were done in accordance with the National Institutes of Health (NIH) guidelines under protocols approved by the Institutional Animal Care and Use Committee (IACUC) of GE Research.

pFUS in ZDF and DIO models.—All rats were anaesthetized with 2–4% isoflurane at 1 l min⁻¹ O₂. Rats were then placed on a water-circulating warming pad with a rectal thermometer probe to monitor body temperature to minimize instances of undue hypothermia capable of influencing nerve transduction. The area above the stimulation target was shaved and hair was fully removed with Nair. The porta hepatis was localized using a custom ultrasound imaging device (Vivid E9; GE Healthcare). Passage of the hepatic and portal artery through the target region and localization in the central intraperitoneal fissure of the liver allowed for ready identification of the porta hepatis under ultrasound imaging. This target was visualized as the entrance of the portal vein (that is, the closest imaging plane in which the portal vein was observed before entrance into the liver). The target location was then marked with a permanent marker and a pFUS stimulation probe was placed on the target area (represented in Fig. 1a) for application of either 3 min of ultrasonic stimulus (ZDF-pFUS; 1.1 MHz, 200 mV per pulse, 150 burst cycles, 500 μ s burst period) or sham stimulus where no energy was applied through the transducer, up to once a day. Although not statistically compared, there were no observed differences in glucose reduction in pilot animals treated using image guidance for every stimulus and animals in which the ultrasound transducer standoff was simply placed above the previously marked target on the skin. The depth of the probe with reference to the animal was held constant using a metal stand (holding the focused ultrasound transducer at a fixed height above the laboratory table). Immediately following completion of the pFUS or sham stimuli, animals were allowed to recover from anaesthesia before either (1) returning to the home cage with free access to food and water (chronic studies), (2) administration of a single oral glucose challenge (2 g kg⁻¹ in sterile water; OGTT) by syringe feeding or (3) reduction of isoflurane to 1–2% for chemical and surgical blocking studies. Sham controls included all steps of the

pFUS treatment, except for activation of the pFUS transducer during the 3 min stimulus period (the power to the transducer was turned off).

Blood glucose levels of the rats were monitored daily for chronic studies, before the pFUS scheduled for that day. For acute/GTT studies, blood glucose was measured at 5 min intervals beginning at time 0, before both pFUS and glucose challenge. In chronic studies (Fig. 1), additional blood samples were collected on a weekly basis for the analysis of circulating markers. A final terminal blood sample was collected at the time of euthanasia and used for the evaluation of circulating insulin levels.

pFUS in ZDF with additional pharmaceutical interventions.—At age 63 d, elevated blood glucose ($>200 \text{ mg dl}^{-1}$) was confirmed in ZDF rats. Rats were then separated into individual treatment groups consisting of either metformin, liraglutide or a combination of pharmaceutical therapy with pFUS (for example, metformin + pFUS, liraglutide + pFUS). Metformin hydrochloride and liraglutide were purchase from Cayman Chemical (13118, 24727) and formulated in PBS and DMSO-PBS (5:95) mixture, respectively. All formulations were maintained at pH 7.2 to prevent physiologic pain or gastric intestinal discomfort (depending on administration route) and formulated daily to prevent degradation arising from storage of the aqueous drug solutions. Dosing calculations were determined using the Du Bois formulation for body surface area dosing; however, concentrations are reported here as mg kg^{-1} for consistency. In this study, both metformin and liraglutide were given in low-dose concentrations of 0.1 mg kg^{-1} and 0.05 ug kg^{-1} , respectively. Each pharmaceutical compound was administered before pFUS or sham-ultrasound stimulation for the combined treatment groups (for example, metformin + pFUS, liraglutide + pFUS). Following administration of either drug, animals were anaesthetized and pFUS stimulus applied (as previously described).

Blood glucose determination.—Whole-blood samples were obtained via tail vein sampling and assessed daily for glucose concentration (chronic studies) and 5 min glucose intervals (for acute GTT studies) using a commercially available Freestyle Freedom Lite (Abbott Diabetes) glucometer. The Freestyle Freedom Light metre uses a small blood volume ($0.3 \text{ }\mu\text{l}$) and as such, no additional fluids were needed to recover total volume following blood sampling. Whole-blood glucometer measurements were compared to serum glucose concentrations (measured by Abaxis Vetscan chemical analyzer) on a weekly basis to confirm overall accuracy of whole-blood measurements over time. The accuracy of commercial glucometers designed for human use has been previously characterized¹¹⁹ and found to be appropriate for analysis of whole blood from rodents. However, to further confirm whole-blood glucose concentrations collected by glucometer, measurements were periodically compared to whole-blood chemistry analysis by biochemical analyser (Abaxis VetScan) as part of the comprehensive metabolic panel, with no significant difference observed.

Insulin resistance evaluation.—Glucose and insulin levels were utilized to determine insulin resistance by applying the HOMA-IR formula, defined as $\text{fasting insulin } (\mu\text{U l}^{-1}) \times \text{fasting glucose } (\text{nmol l}^{-1})/22.5$ ¹²⁰.

Blood chemistry analysis.—Whole-blood samples collected from rats were used to assess the overall health of the rodents using an Abaxis Vetscan blood analyser and the associated comprehensive metabolic panel rotors. A detailed protocol for the comprehensive metabolic panel is provided by the manufacturer at <https://www.abaxis.com/sites/default/files/resourcepackages/VetScan%20Comprehensive%20Diagnostic%20Profile%20PI.pdf>.

Tissue preparation for ELISA analysis.—Organ samples (for example, liver, muscle, adipose, brain) were rapidly removed and homogenized using a Fisher brand 850 homogenizer in a solution of PBS containing phosphatase (0.2 mM phenylmethylsulfonyl fluoride, 5 $\mu\text{g ml}^{-1}$ aprotinin, 1 mM benzamidine, 1 mM sodium orthovanadate and 2 μM cantharidin) and protease (1 μl to 20 mg of tissue, Roche Diagnostics) inhibitors. Blood samples were stored with the anti-coagulant EDTA to prevent coagulation of samples. Samples were then stored at $-80\text{ }^{\circ}\text{C}$ until analysis.

- ELISA kits were purchased and used as specified by the vendors listed below:
- Insulin (90060), leptin (90040) and GLP-1 (81507) ELISA kits were purchased from Crystal Chem.
- IRS-1 (F34735), ghrelin (LS-F39413), GLUT4 (LS-F5891), NPY (LS-F5408), POMC (LS-F8723), KATP channel (LS-F8492-1) and AMPK (LS-F36060) ELISA kits were purchased from LS-Bio.
- Glutamate (ab83389), Glycogen (ab65620) and BDNF ELISA kits were purchased from Abcam.
- GABA (E4457) ELISA kit was purchased from Biovision.

High-performance liquid chromatography (HPLC) analyses.—Serum samples were injected directly into the machine with no pre-treatment. Tissue homogenates were initially homogenized with 0.1 M perchloric acid and centrifuged for 15 min, after which the supernatant was separated, and the sample injected into the HPLC. Catecholamines norepinephrine and epinephrine were analysed by HPLC with inline ultraviolet detector. The test column used in this analysis was a Supelco Discovery C18 (15 cm \times 4.6 mm inside diameter, 5 μm particle size). A biphasic mobile phase composed of (A) acetonitrile:(B) 50 mM KH_2PO_4 , set to pH 3 with phosphoric acid, was then buffered with 100 mg l^{-1} EDTA and 200 mg l^{-1} 1-octane-sulfonic acid. Final concentration of the mobile phase mixture was set to 5:95 A:B. A flow rate of 1 ml min^{-1} was used to improve overall peak resolution while the column was held to a consistent $20\text{ }^{\circ}\text{C}$ to minimize pressure compaction of the column resulting from the viscosity of the utilized mobile phase. The UV detector was maintained at a 254 nm wavelength, which is known to capture the absorption for catecholamines including norepinephrine, epinephrine and dopamine.

Tissue glycogen measurements.—For 4 week samples: tissue samples were washed thoroughly in PBS and transferred into a vial of potassium hydroxide (1 mg:4 ul ; 30% w/v). The suspended tissue was then heated in a boiling water bath for 10 min with constant mixing. The sample was then cooled in an ice bath before the addition of ethanol (100%) for a final concentration of 55% ethanol (v/v). The mixture was then vortexed, followed

rapidly by 10 min of centrifugation at $1,700 \times g$. The supernatant was then decanted, and the remaining pellet resuspended in 8 ml filtered distilled water. This solution was then used to measure total glycogen for each tissue type following the manufacturer's instruction (Abcam: <https://www.abcam.com/Glycogen-Assay-Kit-ab65620.html>).

For 2 h, 24 h and 2 week samples: tissue was collected and immediately flash frozen in liquid nitrogen. When all samples had been collected, tissues were weighed, immediately washed with ice-cold PBS and resuspended in 8 ml of ice-cold deionized (DI) distilled H₂O. Samples were then transferred to ice buckets and homogenized using a Fisher brand 850 homogenizer for 10–15 passes, taking care not to heat the samples during homogenization. Following homogenization samples were boiled for 10 min to inactivate enzymes contained within the sample. Samples were then centrifuged at $18,000 \times g$ in a cold microcentrifuge before fluorometric assay as described by Abcam (<https://www.abcam.com/Glycogen-Assay-Kit-ab65620.html>).

OGTT.—For non-chemical or surgical blocking studies (Fig. 2), rats were fasted overnight (12–16 h) before anaesthetization and placement of a tail vein (TIV) catheter to minimize stress response and haemolysis associated with repeat tail vein sampling. Immediately following the placement of the TIV catheter, a baseline blood sample was collected for glucose analysis, after which the animal was prepared for pFUS stimulation as described above and the animal allowed to recover from anaesthesia. Upon recovery, the animal was given a single oral dose of 2 g kg^{-1} glucose solution by oral syringe feeding. Following glucose administration, blood samples were collected at 5 min intervals from the TIV catheter. All procedures were performed following the IACUC guidelines of GE Global Research. The AUC determined by glucose levels at baseline and 90 min after glucose overload was considered for calculation of AUC-OGTT.

Intravenous glucose tolerance tests (IVGTT).—In instances where complete recovery from anaesthesia elicited a notable stress response due to the introduction of a chemical (Fig. 4c) or surgical (Fig. 4d) blocking, the animal was allowed to incubate under low-level anaesthesia (~1–2% isoflurane) for the duration of the GTT study. In these studies, rats were fasted overnight (12–16 h) before anaesthetization (2–4% isoflurane) and placement of a TIV catheter. Immediately following TIV catheter placement, the animals either received a bolus injection of the chemical blocking agent or surgical resection of the designated nerve as described below.

Chemical blocking at the NTS, IML and IVGTT.—For NTS injection, rats were anaesthetized with 2–4% isoflurane and then placed into a stereotactic frame, with the head angled down at approximately 45° . A water-circulating heating pad was placed immediately below the animal to maintain core body temperature throughout the procedure. An incision was then made at the cisterna magna and the skin retracted to expose the dura mater immediately above the 4th ventricle. A 22-gauge needle was then stereotactically inserted through the dura mater at the following coordinates (anterior, 0.3 mm; lateral, ± 0.15 mm; ventral, 0.3 mm) from the calamus scriptorius and 20 nl lidocaine hydrochloride (20 mg kg^{-1}) or phosphate buffer injected over a 30 s period. The needle was removed 2 min post injection and the surgical site closed using absorbable suture material for muscle and

the skin closed with nylon sutures. Animals were allowed a 10 min incubation under 1% isoflurane, before pFUS application and GTT.

For IML injection, rats were placed into a stereotactic frame equipped with a rat spinal unit. The 5th and 12th thoracic vertebrae were identified and then rigidly fixed into the spinal unit. The dorsal surface of the spinal cord was exposed by laminectomy and irrigated with warm (37 °C) paraffin oil to prevent drying of the spinal cord. The IML was identified at the following coordinates: 0.5 mm lateral to the midline and 0.7 mm ventral from the dorsal surface of the spine. A micropipette was then stereotactically inserted into the IML and 20 nl lidocaine hydrochloride (20 mg kg⁻¹) was injected over a 30 s period, delivered by a controlled syringe pump. The pipette was removed 2 min post injection and the surgical site closed using absorbable suture material for muscle and the skin closed with nylon sutures.

Following lidocaine administration, each animal was allowed to incubate under anaesthesia for 10 min (the time of peak block) before undergoing GTT, for which a baseline blood sample was collected from the TIV catheter before pFUS stimulation of 3 min as previous described. Following pFUS, a single injection of glucose (1 mg kg⁻¹; i.v.) was given and blood samples were collected at 5 min intervals from the TIV catheter.

Surgical blocking of vagal and IML neural pathways, and IVGTT.—For surgical transection of the hepatic vagus, the TIV catheter was first put in place, the animal was then laid supine and an incision made along the midline abdomen. The lobes of the liver were then retracted cranially while the stomach was retracted caudally, exposing the diaphragm. The ventral vagus nerve is visible as it exits the diaphragm isolated within the connective tissue. Following transection of the vagus nerve, the abdominal incision was closed with sutures and a baseline blood sample was collected from the TIV catheter before pFUS stimulation of 3 min as previous described. Following pFUS, isoflurane was adjusted to 1–2% and a single injection of glucose (1 mg kg⁻¹; i.v.) was given. Following glucose challenge, whole-blood samples were collected at 5 min intervals from the TIV catheter for glucose analysis. To block the IML spinal pathways, the spinal cord was transected at the T1 vertebra. These animals were anaesthetized with 2–4% isoflurane and then positioned prone on a water-circulating heating pad with stretched anterior and posterior legs. The area between the neck and hindlimbs was shaved of fur and disinfected with 1% chlorhexidine digluconate. A longitudinal incision was made and the muscles overlying the vertebral column were retracted to expose the vertebral column between T1–T5. Under a magnifier, the T1 spinal segment was lifted, and the spinal cord exposed using a spinal hook and thin scissors, then severed at the level of T1. The T1 vertebra was selected as the uppermost vertebra included in the IML, but below vertebrae known to impact vital functions such as cardiac output and respiration.

Tissue collection for protein and metabolomic analysis.—An incision was made starting at the base of the peritoneal cavity extending up and through to the pleural cavity. Tissues collected included whole liver, muscle (gastrocnemius), visceral white fat (abdominal), intestine (jejunum), brain (hypothalamus punch), kidney, pancreas, spleen and whole blood.

Tissue preparation for transcriptomic analysis.—Organ samples (for example, liver, muscle, adipose, brain) were rapidly removed and cut into sections 2 mm in thickness, transferred into pre-filled tubes containing RNA storage buffer (Applied Biosystems) and later stored at 4–5 °C for 24 h. Following 24 h incubations, organ samples were transferred to a clean centrifuge tube and stored at –20 °C before analysis.

Tissue preparation for metabolomic analysis.—Organ samples of ~20 mg was snap frozen in liquid nitrogen and stored at –80 °C before metabolomic analysis. All samples were prepared at Metabolon using their automated MicroLab STAR system from Hamilton Company. Briefly, small molecules were extracted with methanol under vigorous shaking for 2 min (Glen Mills GenoGrinder 2000), followed by centrifugation. The extract was divided into five fractions: two for analysis by two separate reverse phase (RP)/ultra-performance liquid chromatography (UPLC)–MS/MS methods using positive ion mode electrospray ionization (ESI), one for analysis by RP/UPLC–MS/MS using negative ion mode ESI, one for analysis by hydrophilic interaction liquid chromatography (HILIC)/UPLC–MS/MS using negative ion mode ESI, and one reserved for backup. Further methods on untargeted metabolomic analysis are found below.

Immunohistochemistry and histology protocols.—Non-fasted rats were anaesthetized with 2–4% isoflurane at 1 l min⁻¹ O₂. Rats were then placed on a water-circulating warming pad, with a rectal thermometer probe to monitor body temperature to minimize instances of undue hypothermia capable of influencing nerve transduction. The area above the stimulation target was shaved and hair was fully removed with Nair. The porta hepatis was localized using a custom ultrasound imaging device (Vivid E9; GE Healthcare). The target location was then marked with a permanent marker and a pFUS stimulation probe was placed on the target area (represented in Fig. 1a) for application of either 3 min of ultrasonic stimulus (ZDF-pFUS; 1.1 MHz, 200 mV per pulse, 150 burst cycles, 500 μs burst period) or sham stimulus where no energy was applied through the transducer, up to once a day. Immediately following completion of pFUS or sham stimulation, animals were allowed to recover from anaesthesia, with open access to food and water for 1 h observation for signs of discomfort before euthanization and tissue collection.

Tissue extraction and paraffin blocking were performed as follows: tissue (rat brain) samples were immediately placed into 10% formalin and fixed for ~24 h at 4 °C. The tissue samples were then incubated under vacuum and pressure under the following conditions: 70% ethanol, 37 °C, 40 min; 80% ethanol, 37 °C, 40 min; 2 cycles of 95% ethanol, 37 °C, 40 min; 2 cycles of 100% ethanol, 37 °C, 40 min; 2 cycles of xylene, 37 °C, 40 min; and 3 cycles of paraffin, 65 °C, 40 min. Samples were left in paraffin until ready for embedding (not to exceed ~12–18 h). Tissue samples were then embedded into paraffin blocks for sectioning. The blocks were allowed to cool/harden before cutting into 5-μm-thick sections, and sections were floated on a 50 °C water bath for collection. Positively charged slides were used and the tissues were positioned in the same orientation for every slide. Slides were then either air dried overnight at room temperature or placed on a 40 °C slide warmer (for not more than 1 h) to speed up the drying process, and stored at 4 °C.

Formalin-fixed paraffin-embedded (FFPE) tissue samples (rat brains) were baked at 65 °C for 1 h. Slides were deparaffinized with xylene, rehydrated by washes with decreasing ethanol concentrations, and then processed for antigen retrieval. A two-step antigen retrieval method was developed specifically for multiplexing with FFPE tissues, which allowed for the use of antibodies with different antigen retrieval conditions to be used together on the same samples. Samples were then incubated in PBS with 0.3% Triton X-100 for 10 min at ambient temperature before blocking against nonspecific binding with 10% (w/v) donkey serum and 3% (w/v) bovine serum albumin (BSA) in 1× PBS for 45 min at room temperature. Primary antibody cFOS (Santa Cruz-SC52; sc-166940) was diluted to optimized concentration (5 µg ml⁻¹) and applied for 1 h at room temperature in PBS/3% (v/v) BSA. Samples were then washed sequentially in PBS, PBS-Triton X-100, and then PBS again for 10 min, each with agitation. In the case of secondary antibody detection, samples were incubated with primary antibody species-specific secondary donkey IgG conjugated to either Cy3 or Cy5. Slides were then washed as above and stained in DAPI (10 µg ml⁻¹) for 5 min, rinsed again in PBS, and then mounted with antifade media for image acquisition. Whole-tissue images were acquired on a fluorescence microscope (Olympus IX81) at ×10 magnification. Autofluorescence, which is typical of FFPE tissues, needs to be properly characterized and separated from target fluorophore signals. We used autofluorescence removal processes, wherein an image of the unstained sample was acquired in addition to the stained image. The unstained and stained images were normalized with respect to their exposure times and the dark pixel value (pixel intensity value at zero exposure time). Each normalized autofluorescence image was then subtracted from the corresponding normalized stained image. We ensured that the same regions in the stimulated and control samples were imaged.

cFOS analysis and measures of US-induced activation.—pFUS-stimulated and sham animals were rapidly euthanized, and brains removed and fixed in 10% paraformaldehyde for 24 h, after which they were transferred to a 30% sucrose solution and stored at 4 °C before paraffin embedding (detailed in the immunohistochemistry section above). Coronal sections (5–10 µm) were cut by cryostat. Structures were anatomically defined according to an anatomical atlas. Quantification of cFOS positive cells was done with a fixed sample window across at least four sections by an experimenter blinded to the treatment conditions associated with each distinct coronal section. Regions of interest were as follows: paraventricular hypothalamic nucleus, ARC, ventromedial nucleus, dorsal medial nucleus, lateral hypothalamus and mammillothalamic tract (all structures visible in coronal slices taken between Bregma –2.56 to –3.60 mm). The number of cFOS positive cells in each group was expressed as the percentage of cFOS+ cells as compared to sham-stimulated control littermates.

Hepatic injection of TRPA1 blocker and analysis of effect on hepatic pFUS.—Initial pre-study glucose values were collected using the handheld glucometer Freestyle Freedom Lite (Abbot Diabetes). Following glucose measurements, HC-030031 (8 mg kg⁻¹) was administered to the region immediately adjacent to the porta hepatis via an ultrasound-guided percutaneous injection using the GE Vivid E9 imaging system (GE Healthcare). In brief, sonography was used to identify the portal vein relative to the hepatic artery and

common hepatic duct, which serve as anatomical markers for the porta hepatis. Following identification of the porta hepatis, a single 27-gauge needle was guided into the lower portion of the caudate lobe immediately adjacent to the hepatic artery and portal vein, and a small volume (50 μ l) of the blocker solution was administered (with formulation described above). Caution was taken so as not to disrupt the artery or portal vein to reduce blood loss. Animals were then observed for signs of internal blood loss before they were allowed to recover from anaesthesia.

Modified western-diet mouse model.

Animals.—Experiments were performed on male C57BL/6J mice (8 weeks old, Jackson Laboratories). All procedures were performed in accordance with the NIH guidelines under protocols approved by the IACUC of the Feinstein Institutes for Medical Research, Northwell Health.

Experimental design.—C57BL/6J mice (6–8 weeks old, Jackson Laboratories) were fed regular chow for 10 d in a reverse light cycle room, and then switched to a western diet (WD, D12492, 60% kcal from fat + sugar-supplemented water with 55% fructose and 45% sucrose) or its corresponding isocaloric low-fat control diet (10% kcal from fat) for 16 weeks. Mice in the high-fat WD group received sugar-supplemented water (55% fructose, 45% sucrose). After 8 weeks, both the WD-fed mice and the low-fat control diet mice were divided into two groups—either treated with pFUS of the porta hepatis (once daily) or sham-stimulated for the succeeding 8 weeks. A second cohort of mice underwent the same dietary regimen, but only received alternate-day hepatic pFUS during the stimulation period (weeks 9–16). Blood glucose levels of the mice were monitored on a weekly basis. At week 9 (pre-stimulation period) and week 16 (post-stimulation period), insulin levels were evaluated. Before euthanasia, mice were subjected to a glucose tolerance test.

pFUS.—Mice were anaesthetized with 2% isoflurane at 1 l min⁻¹ O₂. Mice were then placed on a water-circulating warming pad with a rectal thermometer probe to maintain body temperature. The area above the stimulation target was shaved and hair was fully removed with Nair. The porta hepatis was localized using an ultrasound imaging system (GE Healthcare). The location was marked with a permanent marker and a focused ultrasound stimulation probe (GE Research) was placed on the target area. The device then delivered 1 min of stimulation (1.1 MHz, 200 mV per pulse, 150 burst cycles, 500 μ s burst period), followed by a 30 s rest period, then a subsequent 1 min of stimulation.

Blood glucose determination.—Blood glucose levels were assessed weekly by cheek bleed and using a Freestyle blood glucose monitoring system (Abbott Diabetes) with Freestyle blood glucose strips following the manufacturer's recommendations. Mice were fasted 3 h before blood glucose assessment. To recover fluid volume after bleeding, mice were given a 100 μ l injection of saline IP.

GTTs.—At the end of the 16 week period, mice from the four experimental groups were subjected to a glucose tolerance test. The mice were fasted overnight (18 h), weighed and injected with glucose (10% D-glucose solution, 1 g kg⁻¹ IP; Sigma). Glucose levels were

determined at 0, 15, 30, 60 and 120 min after glucose administration, in blood from the tail vein, using Freestyle glucose monitoring test strips. Glucose tolerance curves were generated from the continuous data and the AUC was calculated per graph.

Blood collection.—After a morning fast (3–4 h), blood was collected at weeks 9 and 16 using the cheek bleed method. Approximately 300 μl of whole blood was sampled per animal. Blood samples were spun in a centrifuge (10 min at 5,000 r.p.m., then 2 min at 10,000 r.p.m.) and the serum was extracted and frozen for further evaluation.

Serum blood biochemistry tests.—Serum samples were centrifuged from whole blood drawn by cheek bleeding (10 min at 5,000 r.p.m., then 2 min at 10,000 r.p.m.). The samples were then analysed with a Millipore MILLIPLEX panel assay for insulin levels.

Insulin resistance evaluation.—Glucose and insulin levels were utilized to determine insulin resistance by applying the HOMA-IR formula, defined as fasting insulin ($\mu\text{U l}^{-1}$) \times fasting glucose (nmol l^{-1})/22.5¹²⁰.

STZ-treated diabetic rat model and HEC.

Animals.—Male Sprague–Dawley rats were purchased from Charles River Laboratories and housed in the Yale Animal Resource Center at 22–23 °C in humidity-controlled rooms. Animals fed with high-fat diet (HFD, DIO model) or standard rat chow (STZ-T1D model) and water ad libitum were acclimatized to a 12 h light cycle. All animal procedures were approved by the Yale University IACUC.

DIO model.—Male rats (150–161 g) were fed with HFD for 2 weeks (body weight ~300 g) and then underwent vascular surgery for catheter implantation into the left carotid artery (for blood glucose and hormone sampling) and into the right jugular vein (for insulin and glucose infusions). Four days later, a single IP injection of STZ (35 mg kg^{-1} dissolved in 0.1 M sodium citrate) was administered, followed by daily blood glucose monitoring and subcutaneous saline injection to maintain hydration. A week after steady high blood glucose, rats underwent either pFUS or sham ultrasound treatment (see above for US parameters) for 3 consecutive days before study via insulin clamp.

Lean STZ T1D model.—Male rats (250–280 g) were given a single IP injection of STZ (65 mg kg^{-1} dissolved in normal saline). A second dose of STZ was introduced if the blood glucose of rats fell below 400 mg dl^{-1} 24 h after the first injection. At 5 d post STZ injection, diabetic rats were given long-acting protamine zinc insulin subcutaneously for daily treatment to maintain elevated blood glucose levels (300–550 mg dl^{-1}) but avoid blood glucose extremes and ketosis, and the associated loss in body weight. In addition, the rats received daily subcutaneous saline injections, if needed to maintain hydration. After stable diabetes induction and maintenance for 10 d, animals were anaesthetized and underwent aseptic surgery, with vascular catheter implantation into the left carotid artery (for blood glucose and hormone sampling) and into the right jugular vein (for insulin and glucose infusions). Following a 7 d recovery period, all animals underwent either pFUS or sham

ultrasound treatment (see above for US parameters) for 3 consecutive days before study via insulin clamp.

HEC.—The catheters of overnight-fasted rats were connected to infusion pumps in the morning of the study and then left undisturbed to minimize handling stress for at least 60 min before baseline sampling. Euglycaemia was induced via a bolus infusion of human insulin ($0.025 \text{ U kg}^{-1} \text{ min}^{-1}$, Human R U-100; Eli Lilly) for 30 min (DIO model) or 30–50 min (STZ T1D model), followed by a constant infusion ($0.015 \text{ U kg}^{-1} \text{ min}^{-1}$ in the DIO model or $0.01 \text{ U kg}^{-1} \text{ min}^{-1}$ in the STZ T1D model) of human insulin, together with a variable infusion of 20% glucose for the remainder of the clamp. Plasma glucose was measured every 5 to 10 min throughout the study, and levels were gradually lowered to 110 mg dl^{-1} and maintained at this target for the remaining 90 min. Blood samples were collected at baseline and at 30, 60, 90 and 120 min of the clamp. Plasma was separated immediately and snap frozen in liquid nitrogen, then stored either at $-20 \text{ }^{\circ}\text{C}$ (for insulin, glucagon and corticosterone measurement) or $-80 \text{ }^{\circ}\text{C}$ (for catecholamine measurement). The animals were killed at the end of clamp procedure for further endpoint tissue analyses as necessary.

STZ-treated diabetic rat model with hepatic vagotomy and HEC.

Animals.—Male Sprague–Dawley rats were purchased from Charles River Laboratories and housed in the Yale Animal Resource Center at $22\text{--}23 \text{ }^{\circ}\text{C}$ in humidity-controlled rooms. Animals fed with HFD (DIO model) and water ad libitum were acclimatized to a 12 h light cycle. All animal procedures were approved by the Yale University IACUC.

DIO model and vagotomy.—Male rats (150–161 g) were fed with HFD for 2 weeks (body weight $\sim 300 \text{ g}$) and then underwent vascular surgery to implant catheters into the left carotid artery (for blood glucose and hormone sampling) and into the right jugular vein (for insulin and glucose infusions). During the same procedure, animals underwent midline abdominal incision to localize and cut and tie off the hepatic branch of the abdominal vagus nerve. One week later, a single IP injection of STZ (35 mg kg^{-1} dissolved in 0.1 M sodium citrate) was administered, followed by daily blood glucose monitoring and subcutaneous saline injections if needed to maintain hydration. A week after steady high blood glucose, rats underwent either pFUS or sham ultrasound treatment (see above for US parameters) for 3 consecutive days before study via insulin clamp.

HEC.—The catheters of overnight-fasted rats were connected to infusion pumps in the morning of the study and then left undisturbed to minimize handling stress for at least 60 min before baseline sampling. Euglycaemia was induced via a bolus infusion of human insulin ($0.025 \text{ U kg}^{-1} \text{ min}^{-1}$, Human R U-100; Eli Lilly) for 30 min, followed by a constant infusion ($0.015 \text{ U kg}^{-1} \text{ min}^{-1}$) of human insulin together with a variable infusion of 20% glucose for the remainder of the clamp. Plasma glucose was measured every 5 or 10 min throughout the study and levels were gradually lowered to 110 mg dl^{-1} and maintained at this target for the remaining 90 min. Blood samples were collected at baseline and at 30, 60, 90 and 120 min of the clamp. Plasma was separated immediately and snap frozen in liquid nitrogen, then stored either at $-20 \text{ }^{\circ}\text{C}$ (for insulin, glucagon and corticosterone

measurement) or $-80\text{ }^{\circ}\text{C}$ (for catecholamine measurement). The animals were killed at the end of clamp procedure for further endpoint tissue analyses as necessary.

Swine model and HEC.

Animals.—All experimental procedures and protocols were reviewed and approved by New York Medical College IACUC.

Four adult male Yucatan miniature pigs (Exemplar Genetics) weighing 50–55 kg were examined by an attending veterinarian upon arrival to the facility. None of the animals expressed any signs or symptoms of being unhealthy. Animals went through a 5–10 d acclimation period before the HEC¹²¹ experiment. Each animal was randomized and assigned to a different experiment. Due to inter-species variability, animals were subjected to initial hyperinsulinemic-euglycaemic step-clamp procedures where insulin was infused at a fixed different dose ($0.3\text{--}4\text{ mU kg}^{-1}\text{ min}^{-1}$) to establish the appropriate insulin-response curve. After the insulin-response curve was determined, each animal underwent an additional 2–4 HEC procedures to evaluate the effect of non-invasive FUS on insulin sensitivity. Finally, each swine was subjected to a non-survival procedure, during which the porta hepatis was approached surgically and FUS was delivered directly to it.

Sedation and anaesthesia procedures.—For a 12 h period before surgery, the animals were maintained on a no-food and no-fluid regimen. On the day of surgery, the animal was weighed and sedated with Telazol ($2\text{--}4\text{ mg kg}^{-1}$; intramuscular) and transported to the operating room. Once there, 2–4% isoflurane inhalation anaesthetic mixed with oxygen was administered by a mask. In a supine position, an endotracheal tube was placed, and surgical anaesthesia was maintained on isoflurane and oxygen (2–4% induction, 0.5–3% maintenance). Ventilator settings were adjusted to maintain the end-tidal carbon dioxide at $40 \pm 3\text{ mmHg}$. The depth of anaesthesia was monitored by assessing heart rate, blood pressure, respiration, mandibular jaw tone, absence of corneal reflex and absence of withdrawal response to toe pinch. After successful intubation, a catheter was placed in an ear vein and maintenance fluids were administered ($0.9\%\text{ NaCl}$ at $5\text{--}10\text{ ml kg}^{-1}\text{ h}^{-1}$). Electrocardiography and pulse oximetry were also used for monitoring. Body temperature was controlled with a recirculating warming blanket and/or a hot air warmer.

Vascular access procedures.

Infusion port (venous side): With continued surgical level of anaesthesia, the skin of the right or left ear was shaved, cleansed, sterilized and draped with a surgical field. A 20G intravenous catheter was placed in an ear vein, secured and flushed with heparinized saline. The port was connected to a dual infusion pump (Kd Scientific) and used to infuse insulin and glucose.

Blood sample withdrawal port (arterial side): For the carotid artery catheter placement, the animals were anaesthetized as described above. In a dorsal recumbency position, the neck was shaved and prepared with ethanol and betadine surgical scrub to disinfect the area. A right or left ventral incision (6–8 cm) was made 1 cm lateral and parallel to the midline in the cervical region of the neck. Subcutaneous tissue and muscle layers were

bluntly dissected to expose the carotid sheath and incised to expose the carotid artery. The carotid artery was isolated and permanently ligated at the rostral end using a 3–0 silk suture. A tension suture was placed around the caudal end to control the bleeding. A small sharp incision was made through the arterial wall and a catheter (polyethylene, internal diameter 0.04–0.06 inches) was inserted into the lumen and secured in place using 3–0 silk sutures. The skin and the underlying layers were closed, and the catheter tunneled to the intrascapular region. At the end of the procedure, the animal was returned to the Animal Facilities Recovery area by a comparative medicine technician and monitored at least 3 times per day for 72 h. The animal was allowed to recover for 3–5 d and was then randomly assigned to one of the protocol experiments. The patency of catheters was maintained by flushing with heparinized saline at least once a week and up to 3 times a week. A locking solution (200 U heparin per ml saline, 0.9% NaCl) was used to prevent formation of clots and was replaced weekly.

For the percutaneous puncture technique, the skin above the puncture site was shaved, cleansed, sterilized and dressed in a surgical field. Under ultrasonic guidance, a 19G angiographic needle was passed slowly through the skin at a 60° angle to the target vessel. Once blood backflow was detected (single-wall puncture technique), a soft guide wire (0.035 inch) was introduced into the vessel. Under direct vision and firm vessel compression, the needle was removed and exchanged with a 5 Fr introducer sheath over the sliding wire and secured in place. This technique was used in the event of failure of the carotid artery catheter (due to blockage or destruction) during the first clamp procedure and before beginning the infusion.

Survival HEC procedures.—Following the induction of anaesthesia, fasting blood glucose level was measured as the average of three fasting blood samples taken immediately before the clamp (–30, –15 and –5 min). A fast-acting soluble human insulin (Humalog U-100) infusion (0.3–4 mU kg⁻¹ min⁻¹) was initiated at 0 min and glucose (Dextrose, 20%) infusion (20–250 ml h⁻¹ of a 200 mg ml⁻¹ solution) was given 5 min afterwards. The glucose infusion rate was regulated on the basis of frequent plasma glucose measurements (5 min intervals) to keep the pigs within ±10 mg dl⁻¹ of their fasting glucose level. Using an i-stat handheld blood analyser (Abbott), 0.3 ml of heparinized whole blood for each timepoint was used to measure blood glucose. Samples (1 ml in EDTA tubes) for insulin measurement were taken at 15, 30, 60, 90, 120, 150, 180 and 210 min and stored for further analysis.

After establishing the HEC, approximately within 90–100 min, a diagnostic ultrasound (US) system (GE LOGIQ E10) was used to visualize the liver to identify the anatomical biomarkers relevant to the target nerve. In the supine position, the lower chest and upper abdomen was shaved and cleaned for proper imaging. A full sweep of the liver was performed using a GE C1-6 Curved (convex) Array Probe 1–6 (MHz) at the right subcostal region and a full scan was obtained visualizing the gallbladder and the large vessels. Doppler imaging of the portal vein was used to identify the porta hepatis, which is located ~8 cm in depth. Following diagnostic imaging of the liver and identification of the porta hepatis, the same US probe was placed above the target site and used to apply US stimulation with defined frequency and pulse length parameters, for up to 4 min total duration. Mechanical

ventilation was interrupted for a period of 30–45 s to ensure that the target was not being moved. The ultrasound pulse parameters were applied at the research configuration power setting, using 2.28 MHz carrier frequency, 200 μ s pulse length and \sim 3.7 Hz pulse repetition rate. Glucose levels and glucose infusion rates were recorded again as an indication of insulin sensitivity for an additional 90 min post FUS. At the end of the experiment, insulin infusion was stopped, followed by cessation of glucose infusion after 45 min. Consecutive blood samples confirmed the normal glucose level (euglycaemia).

At the end of the experiment, the physiological parameters were monitored, and consecutive blood samples were taken, confirming the normal glucose level (euglycaemia). Then the animal was gradually weaned off the ventilator and extubated, provided that all physiological parameters were within normal limits. Adequate perfusion, normal blood sugar, temperature and physiological signs were evaluated by the veterinary staff. The animal was returned to the Animal Facilities Recovery area by a comparative medicine technician and was monitored continuously until sufficiently recovered. The animal was monitored at least 3 times per day for 72 h, allowed to recover for 3–5 d and then assigned for the next experiment.

Non-survival HEC procedures.—Following the induction of anaesthesia and while maintaining the anaesthesia with isoflurane (2–3%), a midline surgical incision was made (using a sterile technique and appropriate surgical attire) vertically into the skin, extending caudally 10–12 cm from the xiphoid process. Subcutaneous tissue and muscle layer were bluntly dissected, and haemostasis was achieved using diathermy. The peritoneum was identified and carefully opened parallel to the surgical incision. A self-retractor was placed, and the abdominal cavity was exposed. The internal structure/organs were gently moved to visualize a clear field of the liver and its anatomical structures. The liver borders were identified, and the inner surface was carefully lifted upward to gain access, with direct visualization of the site where the major vessels and ducts enter or leave the liver (porta hepatis). Following visualization of porta hepatis, a GE C1–6 probe in a sterile sleeve was placed and separated from the target site using a sterile ultrasound gel pad (\sim 4 cm thickness; Aquaflex). Following the invasive surgical procedure for the US probe placement, animal fasting blood glucose level was measured as the average of three fasting blood samples taken immediately before the clamp (-30 , -15 and -5 min). A fast-acting soluble human insulin (Humalog U-100) infusion ($0.3\text{--}4$ mU kg $^{-1}$ min $^{-1}$) was initiated at 0 min and glucose (Dextrose, 20%) infusion ($20\text{--}250$ ml h $^{-1}$ of a 200 mg ml $^{-1}$ solution) was given 5 min afterwards. The glucose infusion rate was regulated on the basis of frequent plasma glucose measurements (5 min intervals) to keep the pigs within ± 10 mg dl $^{-1}$ of their fasting glucose level. Using an i-stat handheld blood analyser (Abbott), 0.3 ml of heparinized whole blood for each timepoint was used to measure blood glucose. Samples (1 ml in EDTA tubes) for insulin measurement were taken at 15, 30, 60, 90, 120, 150, 180 and 210 min and stored for further analysis.

After establishing the HEC, approximately within 90–100 min, a diagnostic Doppler US system (GE LOGIQ E10) was used to visualize the portal vein and identify the porta hepatis, located approximately 5 cm deep from the US probe. Following diagnostic imaging of the porta hepatis, the same US transducer (GE C1-6) was placed above the target site and used

to apply US stimulation with defined frequency and pulse length parameters, for up to 4 min total duration. Mechanical ventilation was interrupted for a period of 30–45 s to ensure that the target was not being moved. The ultrasound pulse parameters were applied at the research configuration power setting, using 2.28 MHz carrier frequency, 200 μ s pulse length and ~3.7 Hz pulse repetition rate. Glucose levels and glucose infusion rates were recorded again as an indication of insulin sensitivity for an additional 90 min post FUS.

At the end of the experiment, insulin and glucose infusion were stopped. While maintained under general anaesthesia, the swine was euthanized with Euthasol (1 ml per 10 lb body weight) by i.v. injection. Death was confirmed using electrocardiogram and arterial blood pressure signals. Absence of a pulse in both signals confirms cardiac death. After euthanasia, tissue samples were collected for histological and biochemical analyses.

In a series of control experiments, HEC was established as before, but this time the US probe was used in the non-invasive imaging mode to visualize the porta hepatis, and stimulation was not delivered. HEC was subsequently maintained for at least 30 min and changes in insulin sensitivity were quantified by post-sham-stimulation changes in GIR (as with pFUS-stimulated animals).

Direct neural recording in the PVN in rats.

Animals.—All animals used in our study complied with the NIH and Albany Medical College IACUC guidelines. Male Sprague–Dawley rats weighing 225–300 g were purchased from Taconic and had access to food and water ad libitum, except when fasted for 16–18 h before experiments and craniotomy.

pFUS.—All animals were anaesthetized with an IP injection of urethane (1.2–1.5 g kg⁻¹ in saline). The fur in the abdominal area over the liver was removed and ultrasound gel placed on the shaved surface. The hepatic portal vein was located with an ultrasound imaging scanner and handheld transducer, and marked with a black dot in initial experiments. Animals in subsequent experiments had the black dot on the same abdomen location and were positioned on a gel-containing platform so that the black dot on the abdomen was directly at the centre of the gel where the pFUS transducer was positioned. Next, a hypodermic needle was inserted into the IP space.

For craniotomy and in vivo electrophysiological recordings, animals were placed in a stereotactic frame and burr holes were made. Tungsten microelectrodes with an impedance of 300–500 k Ω or 12-channel multi-array linear recording electrodes (Microprobes) were inserted into the right or left PVN. Single-unit neuronal spiking activity was acquired and amplified 10,000 \times , sampled at 40 kHz and band-pass filtered between 300 and 6,000 Hz with a multi-channel acquisition system (OmniPlex, Plexon) as before^{122–125}.

PVN neurons with amplitudes of at least a 2:1 signal-to-noise ratio were identified and monitored for 60 min for a baseline recording. Subsequently, we IP injected 2 ml of 20% glucose or saline into the catheter. One hour of recordings later, we administered pFUS to the hepatic portal vein and another 60 min of single-unit recordings were obtained. As a

control, PVN spiking activity was monitored for 60 min before an IP injection of glucose or saline, with a subsequent post-injection monitoring period of 120 min.

Blood glucose monitoring.—We obtained blood glucose samples from the tail vein every 20 min concomitant with monitoring of PVN neuronal activity. To do so, a small incision was made on the tail and the glucose level was measured using a small handheld device (Verio Onetouch).

Transcardiac perfusion with paraformaldehyde and Nissl cresyl violet staining.—After the experiment, animals were transcardiac-perfused with heparinized saline, followed by 4% paraformaldehyde in PBS. Brains were extracted and then placed in 30% sucrose for cryoprotection. Sections were cut 60 μm thick (HM500 M cryostat, Leica Biosystems) and mounted on slides. Electrode placement was confirmed with cresyl violet for Nissl substance as described elsewhere¹²². Cresyl violet-stained slides were imaged using the PathScan Enabler IV (Electron Microscopy Sciences) and co-registered onto a rat brain atlas¹²⁶ to determine electrode location.

Chemicals and drugs.—All chemicals were purchased from Sigma-Aldrich, unless specified otherwise.

Data analysis and statistics.—We identified PVN neuronal cells by their waveform and confirmed electrode placement in the PVN. For PVN neuronal cell identification, offline cell sorting was performed using a Matlab wave cluster toolkit. Only single units with amplitudes having at least a 2:1 signal-to-noise ratio were sorted on the basis of wavelets and superparamagnetic clustering¹²⁷. Sorted spikes were processed using custom-made Matlab scripts (www.mathworks.com), which concatenated each 20 min electrophysiological recording interval into a single continuous trace, plotted as 1 min moving averages with s.e.m. for the single-unit spiking activity across the entire recording. For between-group analyses, spike rates were normalized by the maximum spike rate in the 3 h recording. To identify glucose-sensitive neurons, the spike rates 1 h pre ('baseline period') and post ('glucose period') glucose injection were compared. Neurons with spike rates greater than the mean \pm 1 s.d. of the baseline period after glucose administration were classified as GE neurons, whereas those with spike rates less than the mean \pm 1 s.d. of the baseline period were classified as GI neurons. Otherwise, PVN cells were classified as insensitive to glucose. Significance of changes in glucose levels and spike rates were calculated using nonparametric Wilcoxon's rank-sum statistical test.

Mechanical vs ultrasound neuromodulation.

Stimulation systems and CAP neuromodulation.—Two stimulation systems were used for the animal study: a single-element high-intensity focused ultrasound (HIFU) system, and a mechanical vibrator (Tira Vib S 502 shaker).

The pre-clinical ultrasound transducer system used was as shown above and previously used for hepatic pFUS. The function generator (Agilent 33210A) was used to generate a tone burst, with a 1.1 MHz centre frequency, 133 μs pulse length, 500 μs (or 200 ms) pulse repetition period and 200 mV peak-to-peak amplitude. The tone burst signal was again

amplified by the power amplifier (E&I 350L). The output of the power amplifier was sent to the input of the HIFU matching network. The polyurethane coupling cone was used as the standoff, and the focus of the HIFU (full width at half maximum (FWHM); ~2 mm wide and 10 mm long, with a measured peak negative pressure of 2.4 MPa) was targeted at the centre of the spleen for this experimental activation of the cholinergic anti-inflammatory pathway. The stimulus was applied for 3 min as reported previously.

The TIRA vibration system (TV 50018) consists of Shaker S 502 and Amplifier BAA 60 (TIRA GmbH). A function generator (Agilent 32210A) was used to generate a sine wave at four specified frequencies (100, 500, 1,000 and 2,000 Hz), with a pulse length of 133 μ s, a pulse repetition interval of 500 μ s and a peak-to-peak voltage of 200 mV. The stimulus frequency was swept across the four values throughout the 3 min stimulation period. The mechanical piston was actuated at peak force (18 N) during the swept actuation (at frequencies 100–2,000 Hz that are associated with the stimulation pulse frequency ranges associated with both transient shear wave elastography and previous reports of ultrasound-based neuromodulation)^{128,129}. Both the ultrasound and TIRA systems were used to stimulate the CAP for the same 3 min treatment period. The focused ultrasound systems provide tissue displacement primarily near the ultrasound focus, while the TIRA vibrator was used to actuate tissue surface displacements that propagate to the focal spot. The TIRA generates displacements at the level of depth associated with the ultrasound focal points (3–5 mm) that are of the same order of magnitude as the tissue displacement generated by the ultrasound system¹⁵. The CAP was chosen as the nerve pathway (for comparison between ultrasound and mechanical actuator-based neuromodulation) as splenic norepinephrine release and the corresponding tumour necrosis factor (TNF) cytokine output enable rapid and quantitative assessment of both nerve pathway activation and downstream neuromodulation effect¹⁵. The lipopolysaccharide (LPS)-induced inflammation model was utilized in experiments, as this is a standard model to rapidly assess the level of cholinergic anti-inflammatory pathway activation based on pharmacologic and device-based intervention.

Pre-clinical induction of inflammation by LPS administration.—Adult male Sprague–Dawley rats (8–12 weeks old, 250–300 g; Charles River Laboratories) were housed at 25 °C on a 12 h light/dark cycle and acclimatized to handling for 1 week before experiments were conducted to minimize potential confounding effects due to stress response. Water and regular rodent chow were available ad libitum. Experiments were performed under protocols approved by the GE Global Research IACUC.

An LD₇₅ dose (lethal dose 75%) of the endotoxin, LPS, from *Escherichia coli* (0111: B4; Sigma) was administered by IP injection to naive adult Sprague–Dawley rats, causing an elevation in concentrations of pro-inflammatory cytokines. Elevation in cytokine concentrations peaked in 4 h but remained elevated as compared with the control for up to 8 h post injection. Tissue and fluid samples were collected at 60 min post LPS administration and US stimulation.

Tissues were collected at the terminal timepoint as follows: an incision was made starting at the base of the peritoneal cavity extending up and through to the pleural cavity.

Organs (for example, spleen) were rapidly removed and homogenized in a solution of PBS containing phosphatase (0.2 mM phenylmethylsulfonyl fluoride, 5 $\mu\text{g ml}^{-1}$ aprotinin, 1 mM benzamidine, 1 mM sodium orthovanadate and 2 μM cantharidin) and protease (1 μl to 20 mg of tissue, Roche Diagnostics) inhibitors. A targeted final concentration of 0.2 g tissue per ml PBS solution was applied in all samples.

Blood samples were stored with EDTA to prevent coagulation, and then stored at $-80\text{ }^{\circ}\text{C}$ until analysis.

Cytokine concentration in tissue and fluid samples was determined by multi-analyte ELISA assay. A detailed protocol for ELISA assay is provided by the manufacturer at <https://www.qiagen.com/us/products/discovery-and-translational-research/functional-and-cell-analysis/elisaassays/multi-analyte-elisarray-kits/#orderinginformation>.

HPLC analyses of circulating neurotransmitters.—Serum samples were injected directly into the machine with no pre-treatment. Tissue homogenates were initially homogenized with 0.1 M perchloric acid and centrifuged for 15 min, after which the supernatant was separated and the sample injected into the HPLC with an inline ultraviolet detector. The test column used in this analysis was a Supelco Discovery C18 (15 cm \times 4.6 mm inside diameter, 5 μm particle size). A biphasic mobile phase composed of (A) acetonitrile:(B) 50 mM KH_2PO_4 , set to pH 3 with phosphoric acid, was then buffered with 100 mg l^{-1} EDTA and 200 mg l^{-1} 1-octane-sulfonic acid. Final concentration of the mobile phase mixture was set to 5:95 A:B.

A flow rate of 1 ml min^{-1} was used to improve overall peak resolution while the column was held to a consistent $20\text{ }^{\circ}\text{C}$ to minimize pressure compaction of the column resulting from the viscosity of the utilized mobile phase. The UV detector was maintained at a 254 nm wavelength, which is known to capture the absorption for catecholamines including norepinephrine.

In vitro TNF analysis in whole blood.—In brief, terminal blood samples were collected into sterile heparin collection tubes (BD, 366480). Individual blood aliquots of 500 μl were transferred into 12 polystyrene tubes containing either 0, 0.1, 1 or 10 ng ml^{-1} LPS. Concentrations of LPS were tested in triplicate by ELISA (described below).

Each polystyrene tube was then mixed by gentle inversion before being secured on a lab rocker. Samples were then transferred to $37\text{ }^{\circ}\text{C}$ for 4 h with constant rocking. After 4 h, samples were removed from the incubator and centrifuged at 6,000 r.p.m. for 5 min. The plasma supernatant was then removed, and TNF concentrations analysed by ELISA. A detailed protocol for ELISA assay is provided by the manufacturer at <https://www.abcam.com/rat-tnf-alpha-elisa-kit-ab100785.html>.

In vitro ultrasound neuromodulation and chemical ion-channel blocking.

Microfluidic device fabrication for production of hydrogel scaffolds.—For 3D culture of peripheral neurons, we used hydrogel particle scaffolds fabricated using previously reported techniques^{18,79,130}. Briefly, a flow-focusing microfluidic device was

used for manufacturing hydrogel spheres that were assembled in a porous scaffold for in vitro neuron growth. Microfluidic devices were fabricated using soft lithography techniques. Master moulds were fabricated on mechanical-grade silicon wafers (University wafer) using KMPR 1050 photoresist (Microchem). Devices were moulded from the masters using poly(dimethyl)siloxane Sylgard 184 kit (Dow Corning). The base and crosslinker were mixed at a 10:1 mass ratio, poured over the mould and degassed before curing overnight at 65 °C. Channels were sealed by treating the poly(dimethyl)siloxane channels and a glass microscope slide (VWR) with oxygen plasma at 500 mTorr and 80 W for 30 s. The channels were functionalized by injecting 100 µl of Aquapel and reacting for 30 s before washing with Novec 7500 (3 M). The channels were dried by air suction and kept in an oven at 65 °C until used.

Hydrogel spheres for neural growth used thiolated hyaluronic acid (HA) as a precursor to enhance neural cell growth. For the synthesis and characterization of HA, sodium hyaluronate (700 kDa, LifeCore Biomedical) was dissolved at 10 mg ml⁻¹ in distilled DI water. The pH of the HA solution was adjusted to 5.5 using 0.1 M HCl. 1-Ethyl-3-(3-dimethylaminopropyl) carbodiimide (EDC) was dissolved in DI water at the appropriate molar ratio (0.25× unless otherwise stated) immediately before addition to HA solution. Molar ratios in all cases are reported with respect to carboxyl groups on glucuronic acid moieties of HA. *N*-hydroxysuccinimide (Acros Organics) was then added at half of the molar ratio of EDC. The pH was then readjusted to 5.5 and the reaction was mixed at room temperature for 45 min. Then, cystamine dihydrochloride (Sigma-Aldrich) was added (0.25× molar ratio), pH was adjusted to 6.25 using 0.1 M NaOH and the reaction continued while stirring at room temperature overnight. Dithiothreitol (Sigma-Aldrich) was added in excess (4× greater than cystamine) at pH 8. The mixture was stirred for 1–2 h to cleave cystamine disulfides and yield thiolated HA (HA-SH). The reaction was quenched by adjusting the pH to 4. HA-SH was purified using dialysis against acidic (pH 4) DI water for 3 d in the dark. Purified HA-SH was filtered through a 0.22 µm filter (EMD Millipore), frozen under liquid nitrogen, lyophilised and stored at –20 °C until use. HA thiolation was confirmed using the colourimetric Ellman's test for free thiols.

Fabrication of microparticles for the hydrogel scaffold.—Hydrogel microparticles that assemble to provide a porous scaffold for in vitro culture of neurons were manufactured from polyethylene glycol (PEG) and HA using a microfluidic flow-focusing droplet generator. HA-SH and 4-arm vinyl sulfone-terminated PEG (PEG-VS) (20 kDa, Laysan Bio) were crosslinked via Michael-type addition between thiol and vinyl sulfone functional groups. HA-SH and PEG-VS were dissolved separately in PBS at pH 7.4. Cysteine-terminated RGD peptide (GCGYGRGDSPG, GenScript Biotech) was conjugated to PEG-VS by reaction at room temperature for 1 h before gel formation to provide additional sites for cell adhesion. These pre-gel solutions were sterile-filtered through a 0.2 µm polyethersulfone membrane in a luer-lok syringe filter, injected into the microfluidic device and pinched off by an oil phase (0.1% Pico-Surf in Novec 7500, SF-000149, Sphere Fluidics). The flow rates were 10 µl min⁻¹ and 50 µl min⁻¹ for aqueous solutions and oil solutions, respectively. Gels were collected from the device into a tube in oil phase and incubated overnight at room temperature in the dark. Microgels in the oil phase were

vortexed with 20% 1H,1H,2H,2H-Perfluoro-1-octanol (Sigma-Aldrich) in Novec 7500 for 10 s. Microgels were then mixed with a 1:1 mixture of HEPES buffer (100× 10 mM HEPES, 40× 10 mM NaCl, pH 7.4) and hexane, followed by five centrifugations at 10,000 r.p.m. to separate microgels from oil. Microgels were incubated in sterile-filtered 70% ethanol solution at 4 °C at least overnight for sterilization. Before experiments, microgels were washed with HEPES buffer five times.

Dissociation and encapsulation of dorsal root ganglion (DRG) cells in the porous scaffold.—Embryonic (day 18) DRG neuron cells from rats were dissociated

from tissue (BrainBits) and incorporated into the microporous hydrogel scaffold. To dissociate DRG neurons, we first prepared a 100 mg ml⁻¹ stock solution of collagenase/dispase in DI water. The stock solution was diluted 1:100 with Hibernate E storage media without calcium and magnesium (BrainBits) for a final working solution of 1 mg ml⁻¹ collagenase/dispase (0.1 U/0.8 U). The primary DRG tissue was placed in cell dissociation solution for 1 h and incubated at 37 °C with gentle swirling every 5 min. Following incubation, tissue was allowed to settle and the cell dissociation solution was removed, leaving the tissue at the bottom in minimal solution. Immediately following this, 2 ml of Hibernate AB (Brainbits) was added. With a silanized Pasteur pipette, the tissue was triturated ~30× until 90% dispersed. Supernatant containing the dispersed cells was transferred to a sterile tube and spun down at 1,100 r.p.m. for 3 min. The pellet of cells was resuspended in 1 ml of culture media (NbActiv4 with 25 ng ml⁻¹ NGF, BrainBits).

Previously prepared HA-PEG microgels were resuspended, and 40 µl of the mixed solution was injected into a well plate, followed by 90 min of incubation at 37 °C to allow gels to anneal and form a microporous annealed particle scaffold¹³⁰. To incorporate the neurons, aliquots of neurons (4 µl, 50,000 cells) were injected into the porous scaffolds 45 min into gelation. Cell-laden hydrogel scaffolds were incubated for another 45 min at 37 °C to allow full annealing before addition of culture media (150 µl per well in a 96-well plate).

Calcium dye incubation and ultrasound stimulation.—Primary DRG neurons within porous hydrogel scaffolds were incubated with Fluo4 direct calcium assay kit with 250× 10 mM stock solution of probenecid. Briefly, 5 ml of calcium assay buffer was mixed and vortexed with 100 µl of probenecid stock solution to create a 2× loading dye solution. The dye solution was then added to the cells with media in a 1:1 ratio and incubated for 1 h before imaging to allow sufficient diffusion of the dye through the hydrogels. For experiments involving TTX (1 µM), ω-conotoxin-GVIA (1 µM), GsMTx4 (10 µM) and HC-030031 (10 µM), the chemical was added during calcium dye incubation (1 h). Incubated cells were observed under microscopy during pFUS stimulation. The ultrasound transducer, function generator and power amplifier system utilized for pre-clinical hepatic stimulation (and described above) were coupled to each individual culture well using a custom plastic fitting on the culture well plate. The plastic fitting allowed for filling of the culture plate with additional growth media and placement of the plastic standoff cone (described above) directly on top of this liquid layer for acoustic coupling. The height above the growth surface of the culture chamber was set to 12 mm to match the focal position of the transducer (and focal targeting used in the pre-clinical studies), and the ultrasound

stimulus was centred within each neuron culture well using the 20-mm-diameter hole in the centre of the transducer (previously used to insert a small imaging transducer for targeting in the pre-clinical studies described above).

Metabolomics and transcriptomic measurements.

Untargeted metabolomics.—Untargeted metabolomics from blood serum and liver were performed by Metabolon, Research Triangle Park, NC¹³¹. All samples were prepared at Metabolon using their automated MicroLab STAR system from Hamilton Company. Briefly, small molecules were extracted with methanol under vigorous shaking for 2 min (Glen Mills GenoGrinder 2000), followed by centrifugation. The extract was divided into five fractions: two for analysis by two separate RP/UPLC–MS/MS methods using positive ion mode ESI, one for analysis by RP/UPLC–MS/MS using negative ion mode ESI, one for analysis by HILIC/UPLC–MS/MS using negative ion mode ESI, and one reserved for backup. All methods utilized a Waters ACQUITY UPLC and a Thermo Scientific Q-Exactive high-resolution/accurate mass spectrometer interfaced with a heated electrospray ionization (HESI-II) source and Orbitrap mass analyser operated at 35,000 mass resolution. Quality control (QC) samples were introduced and spaced evenly with the randomized experimental samples across the platform run. The median relative standard deviation (RSD) for the internal standards spiked into each of the study samples before injection into the MS instrument was 3% for both the liver and blood serum runs. For the technical replicates created from the experimental samples, the RSD was 7% and 9% for the liver and serum, respectively. A total of 905 liver and 891 blood serum compounds that were within Metabolon’s QC specifications were quantified. These compounds were then identified by comparison to Metabolon’s library (4,500+) entries of purified standards or recurrent unknown entities with retention time/index (RI), mass to charge ratio (m/z) and chromatographic data (including MS/MS spectral data). Biochemical identifications were based on: retention index within a narrow RI window of the proposed identification, accurate mass match to the library ± 10 ppm, and the MS/MS forward and reverse scores computed from the ions present in the experimental spectrum relative to ions present in the library entry spectrum. Metabolon data analysts also used internally developed visualization and interpretation software to confirm and curate the data to ensure accurate identification of true chemical entities and remove those that are due to system artifacts, mis-assignments, redundancy and background noise. For some identified metabolites, a symbol at the end of the metabolite name indicates a specific footnote: *compounds that have not been officially confirmed on the basis of a standard, but Metabolon stated they were confident in its identity; **a compound that is a structural isomer of another compound in the Metabolon spectral library; ***a compound for which a standard is not available, but Metabolon was reasonably confident in its identity or the information provided. A total of 816 liver and 792 blood serum metabolites were identified from the Metabolon library. The metabolite peaks were quantified as AUC detector ion counts. For the liver samples, the quantified values were normalized to total protein (Bradford assay) to correct for systematic variation in metabolite levels due to differences in starting amounts of tissue. All metabolite measures were then re-scaled to have a median equal to 1. Missing values were imputed with the minimum scaled value.

RNA sequencing.—RNA extraction from tissues and RNA sequencing were performed at the Roswell Park Cancer Institute, Genomics Shared Resource, Buffalo, New York¹³². Extractions from tissues yield RNA amounts ranging from 11 to 256 μg (median 78 μg). Quality was assessed by the RNA integrity number (RIN) from a BioAnalyzer (Agilent Technologies). The RIN from all tissue samples ranged from 3 to 9.9 (median 7.4). Samples with low RIN came from two tissue types—pancreas (median 4.0 RIN) and adipose (median 4.5 RIN). Sequencing RNA libraries were prepared using the TruSeq stranded mRNA sample preparation kit (Illumina) according to the manufacturer's instructions, for the RNA from all tissues except the pancreas and adipose. For these samples, due to lower quality RIN scores, the TruSeq stranded total RNA sample preparation kit was used. Sequencing was performed on the Illumina NovaSeq 6000 sequencing platform that output 100 bp paired-end reads ranging from 14 to 55 (median 20) million reads per sample. The RNA-seq data were processed at GE Global Research using established bioinformatics software tools. Base quality control was checked and found to be excellent using Fast QC v0.10.1 from Babraham Bioinformatics^{133,134}. Sequencing reads were mapped (median 71%) to the annotated rat genome version, *Rattus norvegicus* Rnor 6.0.91, using STAR_2.5.3a aligner¹³⁴. Transcript abundance estimates were then generated using RNA-seq by expectation-maximization (RSEM)⁹⁰, which outputs the expected count for each transcript.

Differential transcript expression analysis.—Transcript count normalization and differential expression analysis were performed on all samples using the DESeq2 tool⁹¹. The *P* values attained by the Wald test were corrected for multiple testing using the Benjamini and Hochberg method. Transcripts with an adjusted $P < 0.1$ were counted as being differentially expressed. Outputs from DESeq2 included the median ratio normalization values for each transcript of each sample. These normalized values were used for gene set enrichment analysis (GSEA).

GSEA.—GSEA was performed using GSEA (version 3.0) tool⁹⁷ to identify functional pathways with the gene set collections of Gene Ontology (GO) biological processes (C5), Reactome and KEGG curated gene sets (C2) and the hallmark gene sets (H) available at the Molecular Signatures Database (MSigDB; C5, C2 and H are gene set names)¹³⁵. Diabetes-associated gene sets were assembled from public data sources, including genes associated with type-2 diabetes mellitus from genome-wide association studies (GWAS) and other genetic association datasets^{136–138}. For GSEA, the DESeq2 median ratio normalization values were inputted into the GSEA tool for each gene with a transcript having a log₂ fold change $P < 0.2$. Gene sets identified by the GSEA tool to have a familywise error rate (FWER) $P < 0.1$ were considered significant. The FWER was used over the alternatively provided false discovery rate (FDR) statistics to minimize false positive findings.

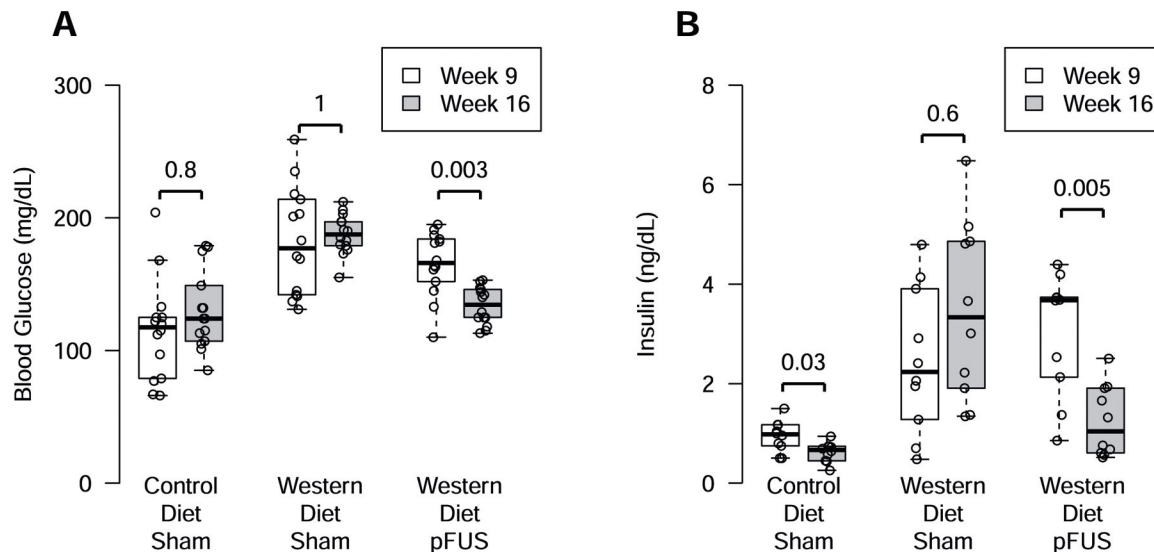
Statistical analysis.

All statistical analyses were conducted using the R software (version 3.6). The Wilcoxon rank-sum test, a nonparametric statistical hypothesis test, was used to compare any two related samples, unless otherwise stated.

Reporting Summary.

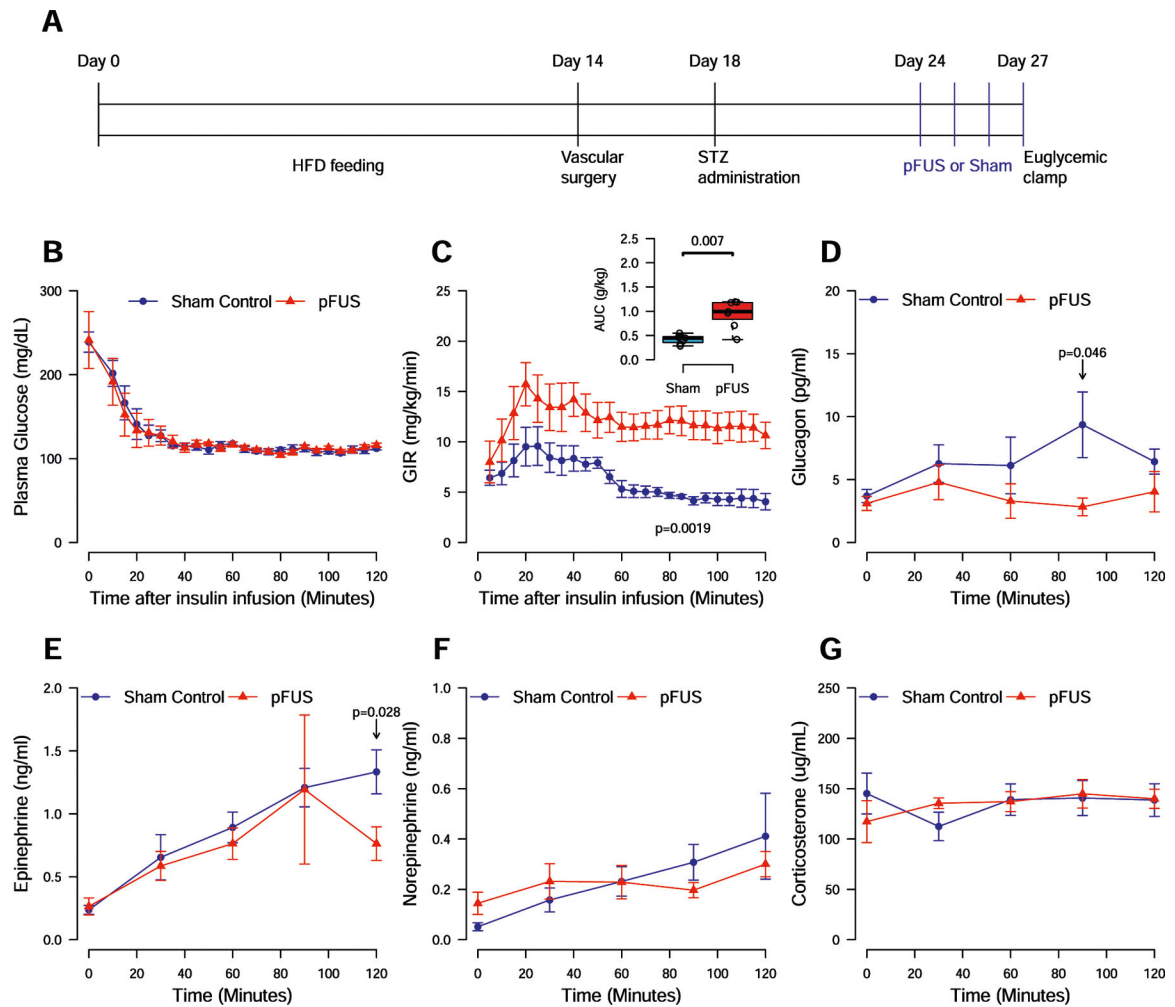
Further information on research design is available in the Nature Research Reporting Summary linked to this article.

Extended Data



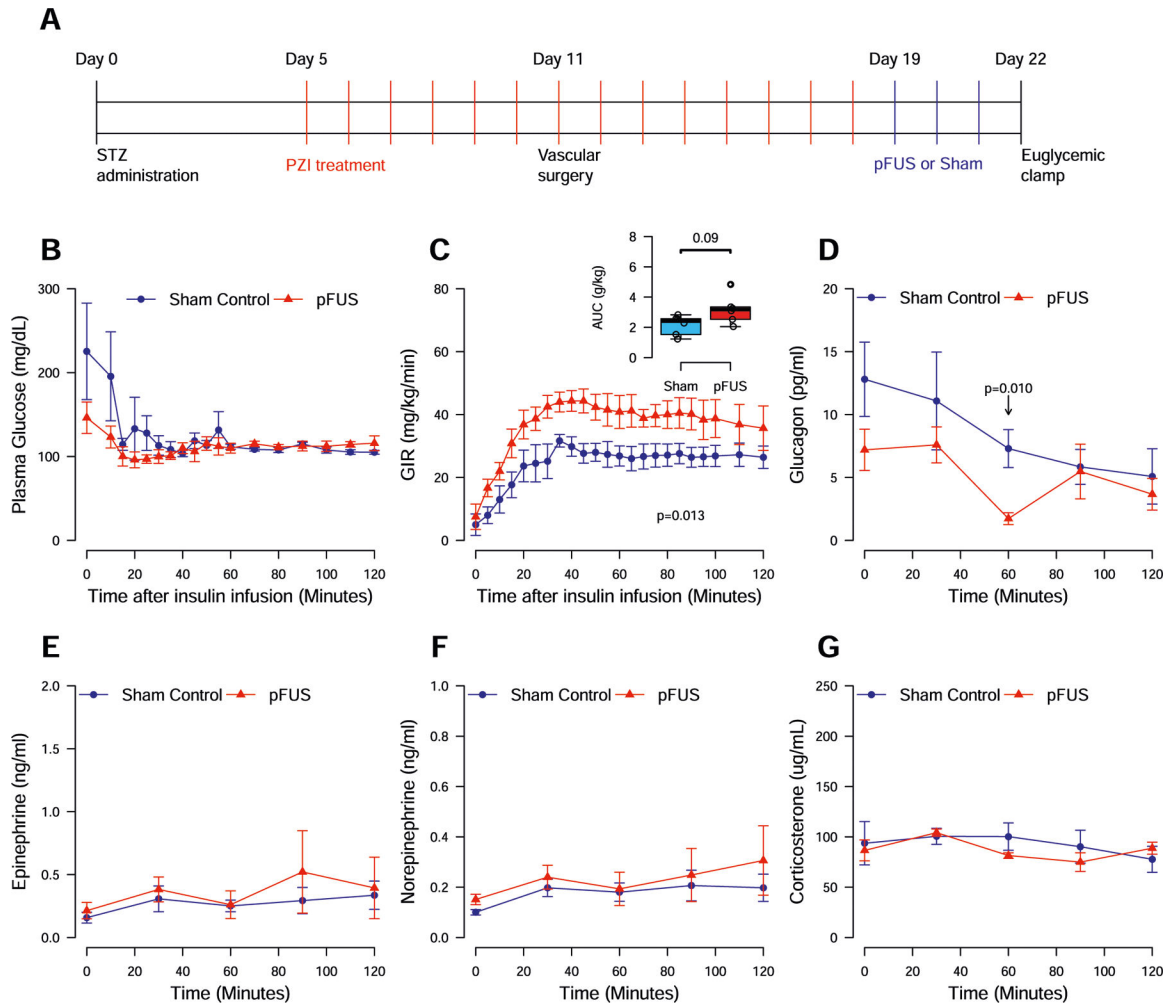
Extended Data Fig. 1 | Hepatic pFUS attenuates hyperglycemia in mice.

a. Hepatic pFUS attenuates hyperglycemia in western diet-fed mice. Blood glucose levels were measured at week 9 (white plots), prior to the stimulation period and week 16 (grey plots), post-stimulation period. Daily stimulated western diet-fed mice had significantly reduced blood glucose levels across the stimulation period (WD-pFUS, week 9 vs week 16; p-values shown are derived using nonparametric Wilcoxon rank-sum test and corrected using the Bonferroni method ($n = 14$ per group; Box plot presents the data median, first and third quartiles and the whiskers are the $1.5 \times$ range (IQR). If no points exceed $1.5 \times$ IQR distance, then the whiskers are simply the minimum and maximum values). **b.** Hepatic pFUS attenuates hyperinsulinemia in western diet-fed mice. Insulin levels were measured at week 9 (white plots), prior to the stimulation period, and at week 16 (grey plots), post-stimulation period. WD-pFUS mice had significantly reduced insulin levels across the stimulation period (WD-pFUS, week 9 vs week 16, p-values shown are derived using nonparametric Wilcoxon rank-sum test (two-sided) and corrected using the Bonferroni method ($n = 10$ per group; Box plot presents the data quartiles and whiskers are the minimum and maximum values unless value exceeds the $1.5 \times$ IQR distance).



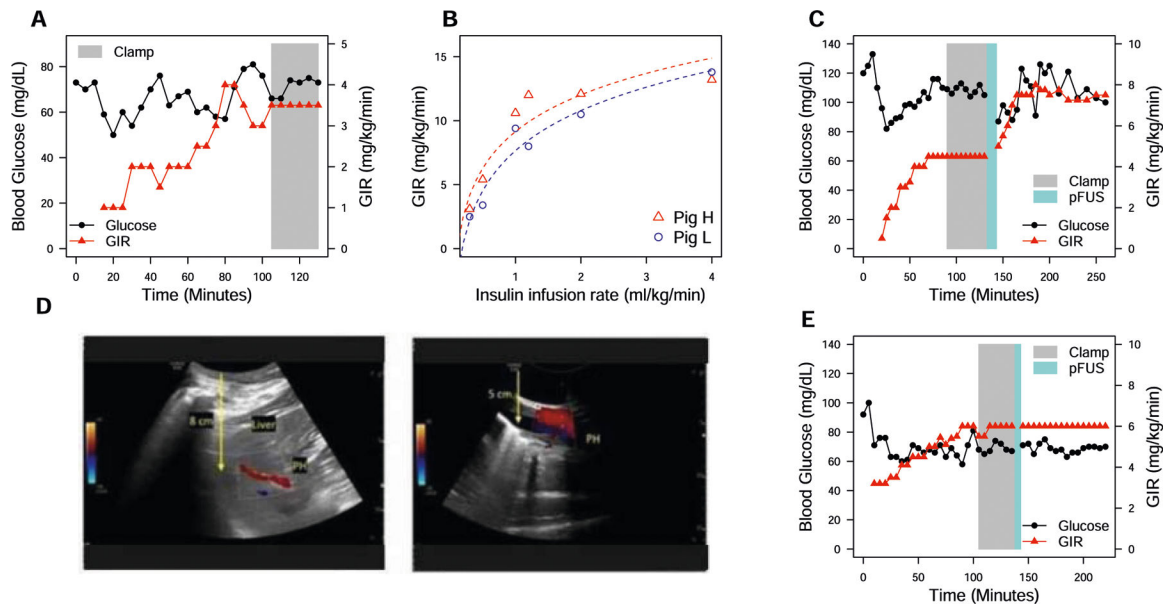
Extended Data Fig. 2 | Effect of pulsed focused ultrasound (pFUS) of the porta hepatis on insulin sensitivity in STZ-induced diabetic diet-induced obesity (DIO) rats, as quantified through hyperinsulinemic-euglycemic clamp¹²¹ (HEC).

a) Timeline of experimental interventions. Glucose infusion rate (GIR) during standardized hyperinsulinemic clamp (glucose values shown in **b**; $n = 7$) revealing higher steady state glucose infusion requirement after pFUS treatment and **c)** glucose infusion rate area under the curve (AUC) for steady state ($n = 7$; Box plot presents the data median, first and third quartiles and the whiskers are the $1.5 \times$ IQR distance, then the whiskers are simply the minimum and maximum values). Plasma hormone change during the clamp including **d)** glucagon **e)** epinephrine, **f)** norepinephrine and **g)** corticosterone. Values are mean \pm SEM; p-values from 2-way ANOVA (GIR); multiple t-tests (hormones); or Wilcoxon rank sum (AUC); $n = 6$ per measurement for D-G.



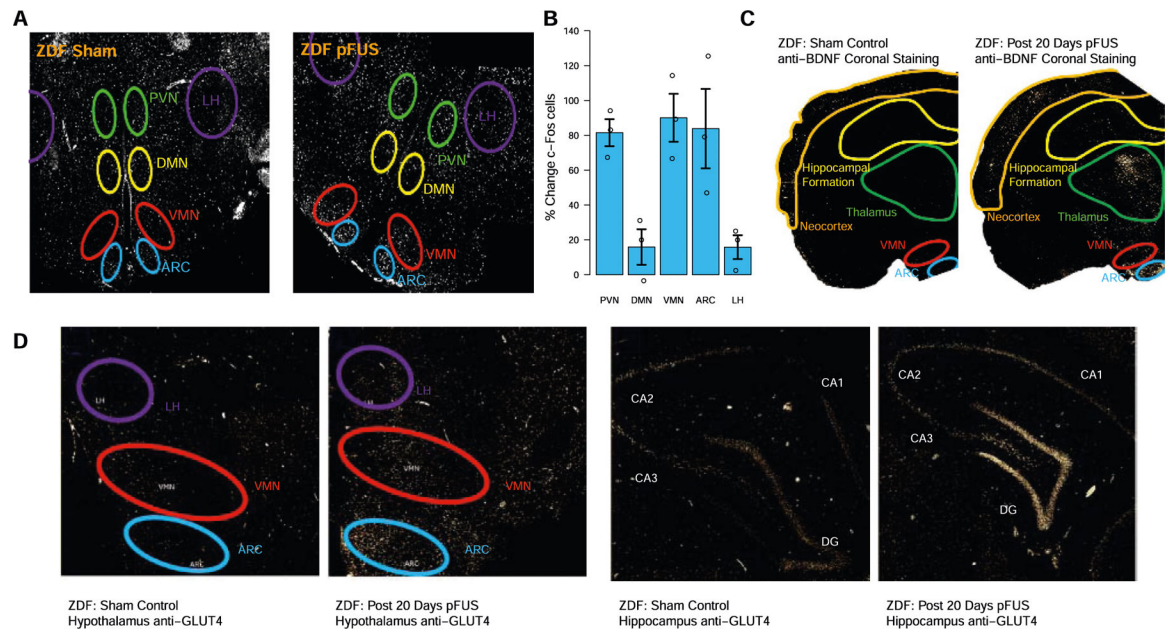
Extended Data Fig. 3 | Effect of pulsed focused ultrasound (pFUS) of the porta hepatis on insulin sensitivity in STZ-induced T1D rats, as quantified through hyperinsulinemic-euglycemic clamp¹²¹ (HEC).

a) Timeline of experimental interventions (see material and methods for experimental description). Glucose infusion rate (GIR) during standardized hyperinsulinemic clamp (glucose values shown in **b**; $n = 6$) revealing higher steady state glucose infusion requirement after pFUS treatment and **c**) glucose infusion rate area under the curve (AUC) for steady state ($n = 6$; Box plot presents the data median, first and third quartiles and the whiskers are the $1.5 \times$ range (IQR). If no points exceed $1.5 \times$ IQR distance, then the whiskers are simply the minimum and maximum values). Plasma hormone change during the clamp including **d**) glucagon, **e**) epinephrine, **f**) norepinephrine and **g**) corticosterone. Values are mean \pm SEM.; p-values from 2-way ANOVA (GIR); multiple t-tests (hormones); or Wilcoxon rank sum (AUC); $n = 5$ per measurement for D-G.



Extended Data Fig. 4 | Short-term effect of focused ultrasound (pFUS) of the porta hepatis on insulin sensitivity in healthy swine, as quantified through hyperinsulinemic-euglycemic clamp (HEC).

a. Representative data from an HEC experiment. Under continuous, constant infusion of insulin at a rate of 0.5 mU/kg/min, glucose infusion rate (GIR) was adjusted every 5 minutes according to a formula¹²¹ to achieve euglycemia (defined as baseline glucose concentration $\pm 10\%$) and maintained for 30 min (grey shaded area). In this example, GIR at euglycemic equilibrium was 3.5 mg/kg/min. The quality of the HEC was assessed by calculating the normalized coefficient of variation (CV) of the glucose concentration and GIR for the duration of euglycemic equilibrium. In this experiment, CV for glucose was 6.92% and for GIR was 6.51%. **b.** In step-clamp experiments, euglycemic equilibrium GIR values were calculated for different insulin infusion rates (IIR) in 2 animals. Based on this data, we decided to conduct pFUS experiments at IIR of 0.5 mU/kg/min, as the slope of the GIR curves, and therefore the sensitivity of the method to resolve changes in insulin sensitivity, decreased at higher IIRs. **c.** Example of a pFUS experiment, after establishing HEC (CV for glucose 2.85%, for GIR 0%). pFUS of the porta hepatis was applied for 4 minutes (blue shaded area), after which GIR was adjusted, just like before, to maintain euglycemia. Increase in GIR after pFUS reflects increased insulin sensitivity. **d.** Imaging of the porta hepatis in swine. Left: Noninvasive imaging (probe placed on skin). Right: Invasive imaging (probe placed on top of PH after it was surgically accessed). **e.** Example of a sham-stimulation experiment in an animal that previously underwent pFUS stimulation. In the sham-stimulation experiment, once HEC was established, the US probe was operated in imaging mode (with ultrasound power off). In the pFUS experiment (results previously shown in Fig. 3) performed in the same animal 3 days later, HEC was established like before and noninvasive pFUS stimulation was delivered. See Methods for experimental descriptions.



Extended Data Fig. 5 |. Histochemical analysis of hypothalamic neural pathways associated with response to pFUS after 20 days of daily stimulation in the ZDF model.

a. cFOS immunohistochemistry images show the number of activated neurons in unstimulated (left) versus pFUS stimulated (right) animals. Images were segmented on the paraventricular nucleus (PVN; green), dorsal medial nucleus (DMN; yellow), ventromedial nucleus (VMN; red), arcuate nucleus (ARC; blue), and lateral hypothalamus (LH; purple) Scale bar = 200 microns. **b.** Data showing the percent change in the number of cFos expressing cells with pFUS compared to sham controls in each segmented hypothalamic region (PVN, DMN, VMN, ARC, LH), images shown represent one set of sham versus stimulated paired ($n = 3$; data shown as mean \pm s.e.). **c.** Histochemical analysis of paraffin-embedded rat brain tissue labeling BDNF antibody showing the unstimulated control (left) and pFUS stimulated animals (right). As observed an increase in BDNF staining was visible in the hypothalamus (with prominence in the arcuate and ventromedial hypothalamus), thalamic and hippocampal brain regions. Images are included as partial coronal sections to demonstrate total BDNF activation by pFUS across a number of brain regions. **d.** Histochemical analysis of paraffin embedded rat brain tissue labeling GLUT-4 receptor antibody showing hypothalamic (left) and hippocampal (right) staining patterns. As observed an increase in both hypothalamic and hippocampal GLUT-4 translocation occurred following hepatic pFUS (right) as compared to unstimulated sham controls (left).

Supplementary Material

Refer to Web version on PubMed Central for supplementary material.

Acknowledgements

We thank G. Petter Fosse (University Hospital of Northern Norway) for helpful discussions on large-animal experiments. Experiments in this study were partially funded with Federal funds from the Defense Advanced Research Project Agency (United States Department of Defense; DARPA DoD; DARPA HR0011-18-C-0040). R.I.H. was supported by the NIH via UL1 TR001863; P30 DK045735; R01 DK101984; R01 DK020495; and

DARPA 401126008. The views, opinions and/or findings expressed herein are those of the authors and should not be interpreted as representing the official views or policies of the Department of Defense or the US Government.

Data availability

The main data supporting the results in this study are available within the manuscript and its Supplementary Information. Source data for the figures are provided with this paper. The RNA-sequencing datasets generated during the study are available in the US National Center for Biotechnology Information Search (NCBI) Gene Expression Omnibus (GEO) repository (series record: GSE197097). Source data are provided with this paper.

References

1. Shahriari D, Rosenfeld D & Anikeeva P Emerging frontier of peripheral nerve and organ interfaces. *Neuron* 108, 270–285 (2020). [PubMed: 33120023]
2. Pavlov VA & Tracey KJ The vagus nerve and the inflammatory reflex—linking immunity and metabolism. *Nat. Rev. Endocrinol* 8, 743–754 (2012). [PubMed: 23169440]
3. Tracey KJ Reflex control of immunity. *Nat. Rev. Immunol* 9, 418–428 (2009). [PubMed: 19461672]
4. Tracey KJ Reflexes in immunity. *Cell* 164, 343–344 (2016). [PubMed: 26824649]
5. Wang H et al. Nicotinic acetylcholine receptor $\alpha 7$ subunit is an essential regulator of inflammation. *Nature* 421, 384–388 (2002). [PubMed: 12508119]
6. Koopman FA et al. Vagus nerve stimulation inhibits cytokine production and attenuates disease severity in rheumatoid arthritis. *Proc. Natl Acad. Sci. USA* 113, 8284–8289 (2016). [PubMed: 27382171]
7. Birmingham K et al. Bioelectronic medicines: a research roadmap. *Nat. Rev. Drug Discov* 13, 399–400 (2014). [PubMed: 24875080]
8. Olofsson PS & Tracey KJ Bioelectronic medicine: technology targeting molecular mechanisms for therapy. *J. Intern. Med* 282, 3–4 (2017). [PubMed: 28621493]
9. Bonaz B et al. Chronic vagus nerve stimulation in Crohn’s disease: a 6-month follow-up pilot study. *Neurogastroenterol. Motil* 28, 948–953 (2016). [PubMed: 26920654]
10. Datta-Chaudhuri T et al. The Fourth Bioelectronic Medicine Summit ‘Technology Targeting Molecular Mechanisms’: current progress, challenges, and charting the future. *Bioelectron. Med* 7, 7 (2021). [PubMed: 34024277]
11. Puleo C & Cotero V Noninvasive neuromodulation of peripheral nerve pathways using ultrasound and its current therapeutic implications. *Cold Spring Harb. Perspect. Med* 10, a034215 (2020). [PubMed: 31138539]
12. Chen R, Romero G, Christiansen MG, Mohr A & Anikeeva P Wireless magnetothermal deep brain stimulation. *Science* 347, 1477–1480 (2015). [PubMed: 25765068]
13. Kim CK, Adhikari A & Deisseroth K Integration of optogenetics with complementary methodologies in systems neuroscience. *Nat. Rev. Neurosci* 18, 222–235 (2017). [PubMed: 28303019]
14. Ibsen S, Tong A, Schutt C, Esener S & Chalasani SH Sonogenetics is a non-invasive approach to activating neurons in *Caenorhabditis elegans*. *Nat. Commun* 6, 8264 (2015). [PubMed: 26372413]
15. Cotero V et al. Noninvasive sub-organ ultrasound stimulation for targeted neuromodulation. *Nat. Commun* 10, 952 (2019). [PubMed: 30862827]
16. Cotero V et al. Peripheral focused ultrasound stimulation (pFUS): new competitor in pharmaceutical markets? *SLAS Technol* 24, 448–452 (2019). [PubMed: 31226243]
17. Huerta TS et al. Targeted peripheral focused ultrasound stimulation attenuates obesity-induced metabolic and inflammatory dysfunctions. *Sci. Rep* 11, 5083 (2021). [PubMed: 33658532]
18. Cotero V et al. Peripheral focused ultrasound neuromodulation (pFUS). *J. Neurosci. Methods* 341, 108721 (2020). [PubMed: 32387189]

19. Akhtar K et al. Non-invasive peripheral focused ultrasound neuromodulation of the celiac plexus ameliorates symptoms in a rat model of inflammatory bowel disease. *Exp. Physiol* 106, 1038–1060 (2021). [PubMed: 33512049]
20. Malbert C-H, Picq C, Divoux J-L, Henry C & Horowitz M Obesity-associated alterations in glucose metabolism are reversed by chronic bilateral stimulation of the abdominal vagus nerve. *Diabetes* 66, 848–857 (2017). [PubMed: 28082456]
21. Meyers EE, Kronemberger A, Lira V, Rahmouni K & Stauss HM Contrasting effects of afferent and efferent vagal nerve stimulation on insulin secretion and blood glucose regulation. *Physiol. Rep* 4, e12718 (2016). [PubMed: 26884478]
22. Stauss H, Meyers E, Glab T & Rahmouni K Modulation of blood glucose concentration by vagal nerve stimulation. *FASEB J* 29, 828.6 (2015). [PubMed: 25411436]
23. Tanida M et al. Leptin receptor signalling in the hypothalamus regulates hepatic autonomic nerve activity via phosphatidylinositol 3-kinase and AMP-activated protein kinase. *J. Neurosci* 35, 474–484 (2015). [PubMed: 25589743]
24. Chen J, Pasricha PJ, Yin J, Lin L & Chen JDZ Hepatic electrical stimulation reduces blood glucose in diabetic rats. *Neurogastroenterol. Motil* 22, 1109–e286 (2010). [PubMed: 20618834]
25. Pocai A, Obici S, Schwartz GJ & Rossetti L A brain–liver circuit regulates glucose homeostasis. *Cell Metab* 1, 53–61 (2005). [PubMed: 16054044]
26. Burcelin R, Dolci W & Thorens B Glucose sensing by the hepatoportal sensor is GLUT2-dependent: in vivo analysis in GLUT2-null mice. *Diabetes* 49, 1643–1648 (2000). [PubMed: 11016447]
27. Lam TKT Neuronal regulation of homeostasis by nutrient sensing. *Nat. Med* 16, 392–395 (2010). [PubMed: 20376051]
28. Lam TKT et al. Hypothalamic sensing of circulating fatty acids is required for glucose homeostasis. *Nat. Med* 11, 320–327 (2005). [PubMed: 15735652]
29. Delaere F, Magnan C & Mithieux G Hypothalamic integration of portal glucose signals and control of food intake and insulin sensitivity. *Diabetes Metab* 36, 257–262 (2010). [PubMed: 20561808]
30. Delaere F et al. The role of sodium-coupled glucose co-transporter 3 in the satiety effect of portal glucose sensing. *Mol. Metab* 2, 47–53 (2013).
31. Cherrington AD Banting Lecture 1997. Control of glucose uptake and release by the liver in vivo. *Diabetes* 48, 1198–1214 (1999). [PubMed: 10331429]
32. Coate KC et al. Portal vein glucose entry triggers a coordinated cellular response that potentiates hepatic glucose uptake and storage in normal but not high-fat/high-fructose-fed dogs. *Diabetes* 62, 392–400 (2013). [PubMed: 23028137]
33. Mithieux G Metabolic effects of portal vein sensing. *Diabetes Obes. Metab* 16, 56–60 (2014). [PubMed: 25200297]
34. Pal A, Rhoads DB & Tavakkoli A Effect of portal glucose sensing on systemic glucose levels in SD and ZDF rats. *PLoS ONE* 11, e0165592 (2016). [PubMed: 27806092]
35. Burcelin R et al. GLUT4, AMP kinase, but not the insulin receptor, are required for hepatoportal glucose sensor-stimulated muscle glucose utilization. *J. Clin. Invest* 111, 1555–1562 (2003). [PubMed: 12750405]
36. Kraft G et al. Portal glucose delivery stimulates muscle but not liver protein metabolism. *Am. J. Physiol. Metab* 303, E1202–E1211 (2012).
37. Yi C-X, la Fleur SE, Fliers E & Kalsbeek A The role of the autonomic nervous liver innervation in the control of energy metabolism. *Biochim. Biophys. Acta* 1802, 416–431 (2010). [PubMed: 20060897]
38. Moore MC et al. Effect of hepatic nerves on disposition of an intraduodenal glucose load. *Am. J. Physiol* 265, E487–E496 (1993). [PubMed: 8214056]
39. Wasserman DH, Williams PE, Lacy DB, Bracy D & Cherrington AD Hepatic nerves are not essential to the increase in hepatic glucose production during muscular work. *Am. J. Physiol* 259, E195–E203 (1990). [PubMed: 2200275]
40. Chan O & Sherwin RS Is there cross talk between portal and hypothalamic glucose-sensing circuits? *Diabetes* 63, 2617–2619 (2014). [PubMed: 25060894]

41. Levin BE, Kang L, Sanders NM & Dunn-Meynell AA Role of neuronal glucosensing in the regulation of energy homeostasis. *Diabetes* 55, S122 LP–S122130 (2006).
42. Jo Y-H & Chua SC The brain–liver connection between BDNF and glucose control. *Diabetes* 62, 1367–1368 (2013). [PubMed: 23613551]
43. Uno K et al. Neuronal pathway from the liver modulates energy expenditure and systemic insulin sensitivity. *Science* 312, 1656–1659 (2006). [PubMed: 16778057]
44. Tahrani AA, Barnett AH & Bailey CJ Pharmacology, and therapeutic implications of current drugs for type 2 diabetes mellitus. *Nat. Rev. Endocrinol* 12, 566–592 (2016). [PubMed: 27339889]
45. Jokiah AJ, Donovan CM & Watts AG The rate of fall of blood glucose determines the necessity of forebrain-projecting catecholaminergic neurons for male rat sympathoadrenal responses. *Diabetes* 63, 2854–2865 (2014). [PubMed: 24740574]
46. Bohland M et al. Activation of hindbrain neurons is mediated by portal-mesenteric vein glucosensors during slow-onset hypoglycemia. *Diabetes* 63, 2866–2875 (2014). [PubMed: 24727435]
47. Fujita S & Donovan CM Celiac-superior mesenteric ganglionectomy, but not vagotomy, suppresses the sympathoadrenal response to insulin-induced hypoglycemia. *Diabetes* 54, 3258–3264 (2005). [PubMed: 16249453]
48. Randich A, Spraggins DS, Cox JE, Meller ST & Kelm GR Jejunal or portal vein infusions of lipids increase hepatic vagal afferent activity. *Neuroreport* 12, 3101–3105 (2001). [PubMed: 11568645]
49. Routh VH, Hao L, Santiago AM, Sheng Z & Zhou C Hypothalamic glucose sensing: making ends meet. *Front. Syst. Neurosci* 8, 236 (2014). [PubMed: 25540613]
50. Adachi A, Shimizu N, Oomura Y & Kobáshi M Convergence of hepatoportal glucose-sensitive afferent signals to glucose-sensitive units within the nucleus of the solitary tract. *Neurosci. Lett* 46, 215–218 (1984). [PubMed: 6738915]
51. Kandilis AN, Papadopoulou IP, Koskinas J, Sotiropoulos G & Tiniakos DG Liver innervation and hepatic function: new insights. *J. Surg. Res* 194, 511–519 (2015). [PubMed: 25555404]
52. Kalra SP Disruption in the leptin–NPY link underlies the pandemic of diabetes and metabolic syndrome: new therapeutic approaches. *Nutrition* 24, 820–826 (2008). [PubMed: 18725078]
53. Chee MJS, Myers MGJ, Price CJ & Colmers WF Neuropeptide Y suppresses anorexigenic output from the ventromedial nucleus of the hypothalamus. *J. Neurosci.* 30, 3380–3390 (2010). [PubMed: 20203197]
54. Loh K, Herzog H & Shi Y-C Regulation of energy homeostasis by the NPY system. *Trends Endocrinol. Metab.* 26, 125–135 (2015). [PubMed: 25662369]
55. Engström Ruud L, Pereira MMA, de Solis AJ, Fenselau H & Brüning JC NPY mediates the rapid feeding and glucose metabolism regulatory functions of AgRP neurons. *Nat. Commun.* 11, 442 (2020). [PubMed: 31974377]
56. Cowley MA et al. Leptin activates anorexigenic POMC neurons through a neural network in the arcuate nucleus. *Nature* 411, 480–484 (2001). [PubMed: 11373681]
57. Hahn TM, Breininger JF, Baskin DG & Schwartz MW Co-expression of Agrp and NPY in fasting-activated hypothalamic neurons. *Nat. Neurosci.* 1, 271–272 (1998). [PubMed: 10195157]
58. O’Hare JD & Zsombok A Brain-liver connections: role of the pre-autonomic PVN neurons. *Am. J. Physiol. Endocrinol. Metab.* 310, E183–E189 (2016).
59. Fenselau H et al. A rapidly acting glutamatergic ARC→PVH satiety circuit post-synaptically regulated by α -MSH. *Nat. Neurosci.* 20, 42–51 (2017). [PubMed: 27869800]
60. Van den Pol AN, Acuna C, Davis JN, Huang H & Zhang X Defining the caudal hypothalamic arcuate nucleus with a focus on anorexic excitatory neurons. *J. Physiol.* 597, 1605–1625 (2019). [PubMed: 30618146]
61. Wang P et al. A leptin-BDNF pathway regulating sympathetic innervation of adipose tissue. *Nature* 583, 839–844 (2020). [PubMed: 32699414]
62. Miki T et al. ATP-sensitive K⁺ channels in the hypothalamus are essential for the maintenance of glucose homeostasis. *Nat. Neurosci.* 4, 507–512 (2001). [PubMed: 11319559]

63. Murphy BA, Fakira KA, Song Z, Beuve A & Routh VH AMP-activated protein kinase and nitric oxide regulate the glucose sensitivity of ventromedial hypothalamic glucose-inhibited neurons. *Am. J. Physiol. Cell Physiol.* 297, C750–C758 (2009). [PubMed: 19570894]
64. Routh VH Glucose sensing neurons in the ventromedial hypothalamus. *Sensors* 10, 9002–9025 (2010). [PubMed: 22022208]
65. Cotero VE & Routh VH Insulin blunts the response of glucose-excited neurons in the ventrolateral-ventromedial hypothalamic nucleus to decreased glucose. *Am. J. Physiol. Endocrinol. Metab* 296, E1101–E1109 (2009). [PubMed: 19223652]
66. Cotero VE, Zhang BB & Routh VH The response of glucose-excited neurones in the ventromedial hypothalamus to decreased glucose is enhanced in a murine model of type 2 diabetes mellitus. *J. Neuroendocrinol* 22, 65–74 (2010). [PubMed: 20002964]
67. Gardemann A, Strulik H & Jungermann K A portal-arterial glucose concentration gradient as a signal for an insulin-dependent net glucose uptake in perfused rat liver. *FEBS Lett* 202, 255–259 (1986). [PubMed: 3522273]
68. Moore MC, Coate KC, Winnick JJ, An Z & Cherrington AD Regulation of hepatic glucose uptake and storage in vivo. *Adv. Nutr* 3, 286–294 (2012). [PubMed: 22585902]
69. Wang R et al. The regulation of glucose-excited neurons in the hypothalamic arcuate nucleus by glucose and feeding-relevant peptides. *Diabetes* 53, 1959–1965 (2004). [PubMed: 15277373]
70. Williams G et al. The hypothalamus and the control of energy homeostasis: different circuits, different purposes. *Physiol. Behav* 74, 683–701 (2001). [PubMed: 11790431]
71. Marty N, Dallaporta M & Thorens B Brain glucose sensing, counter-regulation, and energy homeostasis. *Physiology* 22, 241–251 (2007). [PubMed: 17699877]
72. Karnani M & Burdakov D Multiple hypothalamic circuits sense and regulate glucose levels. *Am. J. Physiol. Integr. Comp. Physiol* 300, R47–R55 (2010).
73. Ren H et al. Altered central nutrient sensing in male mice lacking insulin receptors in Glut4-expressing neurons. *Endocrinology* 160, 2038–2048 (2019). [PubMed: 31199472]
74. King BM The rise, fall, and resurrection of the ventromedial hypothalamus in the regulation of feeding behaviour and body weight. *Physiol. Behav* 87, 221–244 (2006). [PubMed: 16412483]
75. Muroya S, Yada T, Shioda S & Takigawa M Glucose-sensitive neurons in the rat arcuate nucleus contain neuropeptide Y. *Neurosci. Lett* 264, 113–116 (1999). [PubMed: 10320027]
76. Ibrahim N et al. Hypothalamic proopiomelanocortin neurons are glucose responsive and express K(ATP) channels. *Endocrinology* 144, 1331–1340 (2003). [PubMed: 12639916]
77. Moparthi L & Zygmunt PM Human TRPA1 is an inherently mechanosensitive bilayer-gated ion channel. *Cell Calcium* 91, 102255 (2020). [PubMed: 32717533]
78. Bae C, Sachs F & Gottlieb PA The mechanosensitive ion channel Piezo1 Is inhibited by the peptide GsMTx4. *Biochemistry* 50, 6295–6300 (2011). [PubMed: 21696149]
79. De Rutte JM, Koh J & Di Carlo D Scalable high-throughput production of modular microgels for in situ assembly of microporous tissue scaffolds. *Adv. Funct. Mater* 29, 1900071 (2019).
80. Motter AL & Ahern GP TRPA1 is a polyunsaturated fatty acid sensor in mammals. *PLoS ONE* 7, e38439 (2012). [PubMed: 22723860]
81. Kong X et al. Roux-en-Y gastric bypass enhances insulin secretion in type 2 diabetes via FXR-mediated TRPA1 expression. *Mol. Metab* 29, 1–11 (2019). [PubMed: 31668381]
82. Derbenev AV & Zsombok A Potential therapeutic value of TRPV1 and TRPA1 in diabetes mellitus and obesity. *Semin. Immunopathol* 38, 397–406 (2016). [PubMed: 26403087]
83. Li M et al. Transient receptor potential V channels are essential for glucose sensing by aldolase and AMPK. *Cell Metab* 30, 508–524.e12 (2019). [PubMed: 31204282]
84. Zsombok A & Derbenev AV TRP channels as therapeutic targets in diabetes and obesity. *Pharmaceuticals* 9, 50 (2016). [PubMed: 27548188]
85. Ahn J, Lee H, Im SW, Jung CH & Ha TY Allyl isothiocyanate ameliorates insulin resistance through the regulation of mitochondrial function. *J. Nutr. Biochem* 25, 1026–1034 (2014). [PubMed: 25034503]
86. Lee E et al. Transient receptor potential vanilloid type-1 channel regulates diet-induced obesity, insulin resistance, and leptin resistance. *FASEB J* 29, 3182–3192 (2015). [PubMed: 25888600]

87. Jönsson TJ, Schäfer H-L, Herling AW & Brönstrup M A metabolome-wide characterization of the diabetic phenotype in ZDF rats and its reversal by pioglitazone. *PLoS ONE* 13, e0207210 (2018). [PubMed: 30481177]
88. Ashburner M et al. Gene ontology: tool for the unification of biology. The Gene Ontology Consortium. *Nat. Genet* 25, 25–29 (2000). [PubMed: 10802651]
89. Mi H, Muruganujan A, Ebert D, Huang X & Thomas PD PANTHER version 14: more genomes, a new PANTHER GO-slim and improvements in enrichment analysis tools. *Nucleic Acids Res* 47, D419–D426 (2019). [PubMed: 30407594]
90. Li B & Dewey CN RSEM: accurate transcript quantification from RNA-seq data with or without a reference genome. *BMC Bioinformatics* 12, 323 (2011). [PubMed: 21816040]
91. Love MI, Huber W & Anders S Moderated estimation of fold change and dispersion for RNA-seq data with DESeq2. *Genome Biol* 15, 550 (2014). [PubMed: 25516281]
92. Subramanian A et al. Gene set enrichment analysis: a knowledge-based approach for interpreting genome-wide expression profiles. *Proc. Natl Acad. Sci. USA* 102, 15545–15550 (2005). [PubMed: 16199517]
93. Kalsbeek A, la Fleur S & Fliers E Circadian control of glucose metabolism. *Mol. Metab* 3, 372–383 (2014). [PubMed: 24944897]
94. Kettner N et al. Circadian dysfunction induces leptin resistance in mice. *Cell Metab* 10.1016/j.cmet.2015.06.005 (2015).
95. Li A-J et al. Leptin-sensitive neurons in the arcuate nuclei contribute to endogenous feeding rhythms. *Am. J. Physiol. Regul. Integr. Comp. Physiol* 302, R1313–R1326 (2012). [PubMed: 22492818]
96. Wiater MF et al. Circadian integration of sleep-wake and feeding requires NPY receptor-expressing neurons in the mediobasal hypothalamus. *Am. J. Physiol. Regul. Integr. Comp. Physiol* 301, R1569–R1583 (2011). [PubMed: 21880863]
97. Khan S, Duan P, Yao L & Hou H Shiftwork-mediated disruptions of circadian rhythms and sleep homeostasis cause serious health problems. *Int. J. Genomics* 2018, 8576890 (2018). [PubMed: 29607311]
98. Park S-J et al. DNA-PK promotes the mitochondrial, metabolic, and physical decline that occurs during aging. *Cell Metab* 25, 1135–1146.e7 (2017). [PubMed: 28467930]
99. Hvid H et al. Diabetic phenotype in the small intestine of zucker diabetic fatty rats. *Digestion* 94, 199–214 (2016). [PubMed: 27931035]
100. Kakimoto PA & Kowaltowski AJ Effects of high fat diets on rodent liver bioenergetics and oxidative imbalance. *Redox Biol* 8, 216–225 (2016). [PubMed: 26826574]
101. Karanth S et al. FOXN3 controls liver glucose metabolism by regulating gluconeogenic substrate selection. *Physiol. Rep.* 7, e14238 (2019). [PubMed: 31552709]
102. Mullins GR et al. Catecholamine-induced lipolysis causes mTOR complex dissociation and inhibits glucose uptake in adipocytes. *Proc. Natl Acad. Sci. USA* 111, 17450–17455 (2014). [PubMed: 25422441]
103. Dungan K 1,5-Anhydroglucitol (GlycoMark) as a marker of short-term glycemic control and glycemic excursions. *Expert Rev. Mol. Diagn* 8, 9–19 (2008). [PubMed: 18088226]
104. Prawitt J, Caron S & Staels B Bile acid metabolism and the pathogenesis of type 2 diabetes. *Curr. Diab. Rep* 11, 160–166 (2011). [PubMed: 21431855]
105. Bergman BC et al. Serum sphingolipids: relationships to insulin sensitivity and changes with exercise in humans. *Am. J. Physiol. Metab* 309, E398–E408 (2015).
106. Michalczyk A, Doł gowska B, Hery R, Chlubek D & Safranow K Associations between plasma lysophospholipids concentrations, chronic kidney disease and the type of renal replacement therapy. *Lipids Health Dis* 18, 85 (2019). [PubMed: 30947711]
107. Sandoval DA, Obici S & Seeley RJ Targeting the CNS to treat type 2 diabetes. *Nat. Rev. Drug Discov* 8, 386–398 (2009). [PubMed: 19404312]
108. Rykkje A, Carlsen JF & Nielsen MB Hand-held ultrasound devices compared with high-end ultrasound systems: a systematic review. *Diagnostics* 9, 61 (2019). [PubMed: 31208078]

109. Pashaei V et al. Flexible body-conformal ultrasound patches for image-guided neuromodulation. *IEEE Trans. Biomed. Circuits Syst* 14, 305–318 (2020). [PubMed: 31831437]
110. Al-Battal AF et al. A CNN segmentation-based approach to object detection and tracking in ultrasound scans with application to the vagus nerve detection Preprint at 10.48550/arXiv.2106.13849 (2021).
111. Scarlett JM et al. Central injection of fibroblast growth factor 1 induces sustained remission of diabetic hyperglycemia in rodents. *Nat. Med* 22, 800–806 (2016). [PubMed: 27213816]
112. Scarlett JM et al. Peripheral mechanisms mediating the sustained antidiabetic action of fgf1 in the brain. *Diabetes* 68, 654–664 (2019). [PubMed: 30523024]
113. Kuhre RE et al. Bile acids are important direct and indirect regulators of the secretion of appetite- and metabolism-regulating hormones from the gut and pancreas. *Mol. Metab* 11, 84–95 (2018). [PubMed: 29656109]
114. Kraft G et al. Sympathetic denervation of the common hepatic artery lessens glucose intolerance in the fat- and fructose-fed dog. *Diabetes* 68, 1143–1155 (2019). [PubMed: 30936143]
115. Shimizu N, Oomura Y, Novin D, Grijalva CV & Cooper PH Functional correlations between lateral hypothalamic glucose-sensitive neurons and hepatic portal glucose-sensitive units in rat. *Brain Res* 265, 49–54 (1983). [PubMed: 6850320]
116. Jensen JFIELD A program for simulating ultrasound systems. *Med. Biol. Eng. Comput* 34, 351–352 (1996). [PubMed: 8945858]
117. Jensen JA & Svendsen NB Calculation of pressure fields from arbitrarily shaped, apodized, and excited ultrasound transducers. *IEEE Trans. Ultrason. Ferroelectr. Freq. Control* 39, 262–267 (1992). [PubMed: 18263145]
118. Nykonenko A, Vávra P & Zon a P Anatomic peculiarities of pig and human liver. *Exp. Clin. Transplant* 15, 21–26 (2017).
119. Morley LA, Gomez TH, Goldman JL, Flores R & Robinson MA Accuracy of 5 point-of-care glucometers in C57BL/6J mice. *J. Am. Assoc. Lab. Anim. Sci* 57, 44–50 (2018). [PubMed: 29402351]
120. Mlinar B, Marc J, Janež A & Pfeifer M Molecular mechanisms of insulin resistance and associated diseases. *Clin. Chim. Acta* 375, 20–35 (2007). [PubMed: 16956601]
121. DeFronzo RA, Tobin JD & Andres R Glucose clamp technique: a method for quantifying insulin secretion and resistance. *Am. J. Physiol* 237, E214 (1979). [PubMed: 382871]
122. O’Connor KA et al. Effect of diazepam and yohimbine on neuronal activity in sham and hemiparkinsonian rats. *Neuroscience* 351, 71–83 (2017). [PubMed: 28385635]
123. Sutton AC, O’Connor KA, Pilitsis JG & Shin DS Stimulation of the subthalamic nucleus engages the cerebellum for motor function in parkinsonian rats. *Brain Struct. Funct* 220, 3595–3609 (2015). [PubMed: 25124274]
124. Sutton AC et al. Deep brain stimulation of the substantia nigra pars reticulata improves forelimb akinesia in the hemiparkinsonian rat. *J. Neurophysiol* 109, 363–374 (2012). [PubMed: 23076106]
125. Gee LE, Walling I, Ramirez-Zamora A, Shin DS & Pilitsis JG Subthalamic deep brain stimulation alters neuronal firing in canonical pain nuclei in a 6-hydroxydopamine lesioned rat model of Parkinson’s disease. *Exp. Neurol* 283, 298–307 (2016). [PubMed: 27373204]
126. Paxinos G & Watson C *The Rat Brain in Stereotaxic Coordinates* (Academic Press, 1982).
127. Quiroga RQ, Nadasdy Z & Ben-Shaul Y Unsupervised spike detection and sorting with wavelets and superparamagnetic clustering. *Neural Comput* 16, 1661–1687 (2004). [PubMed: 15228749]
128. Gennisson J-L, Deffieux T, Fink M & Tanter M Ultrasound elastography: principles and techniques. *Diagn. Interv. Imaging* 94, 487–495 (2013). [PubMed: 23619292]
129. Sandrin L et al. Transient elastography: a new noninvasive method for assessment of hepatic fibrosis. *Ultrasound Med. Biol* 29, 1705–1713 (2003). [PubMed: 14698338]
130. Griffin DR, Weaver WM, Scumpia PO, Di Carlo D & Segura T Accelerated wound healing by injectable microporous gel scaffolds assembled from annealed building blocks. *Nat. Mater* 14, 737–744 (2015). [PubMed: 26030305]
131. Metabolon Reporting and Interpretation (Metabolon, 2021); <https://www.metabolon.com/solutions/reporting-interpretation/>

132. Roswell Park Cancer Center - Shared Genomics Resource (Roswell Park Cancer Center, 2021); <https://www.roswellpark.org/shared-resources/genomics>
133. Andrews S FastQC: A Quality Control Tool for High Throughput Sequence Data <http://www.bioinformatics.babraham.ac.uk/projects/fastqc> (2010)
134. Dobin A & Gingeras TR Mapping RNA-seq reads with STAR. *Curr. Protoc. Bioinformatics* 51, 11.14.1–11.14.19 (2015).
135. Liberzon A et al. The molecular signatures database hallmark gene set collection. *Cell Syst.* 1, 417–425 (2015). [PubMed: 26771021]
136. Flannick J et al. Exome sequencing of 20,791 cases of type 2 diabetes and 24,440 controls. *Nature* 570, 71–76 (2019). [PubMed: 31118516]
137. Li MJ et al. GWASdb: a database for human genetic variants identified by genome-wide association studies. *Nucleic Acids Res* 40, D1047–D1054 (2012). [PubMed: 22139925]
138. Rouillard AD et al. The harmonizome: a collection of processed datasets gathered to serve and mine knowledge about genes and proteins. *Database* 2016, baw100 (2016). [PubMed: 27374120]
139. Ruud J, Steculorum SM & Brüning JC Neuronal control of peripheral insulin sensitivity and glucose metabolism. *Nat. Commun* 8, 15259 (2017). [PubMed: 28469281]
140. Myers MGJ & Olson DP Central nervous system control of metabolism. *Nature* 491, 357–363 (2012). [PubMed: 23151578]

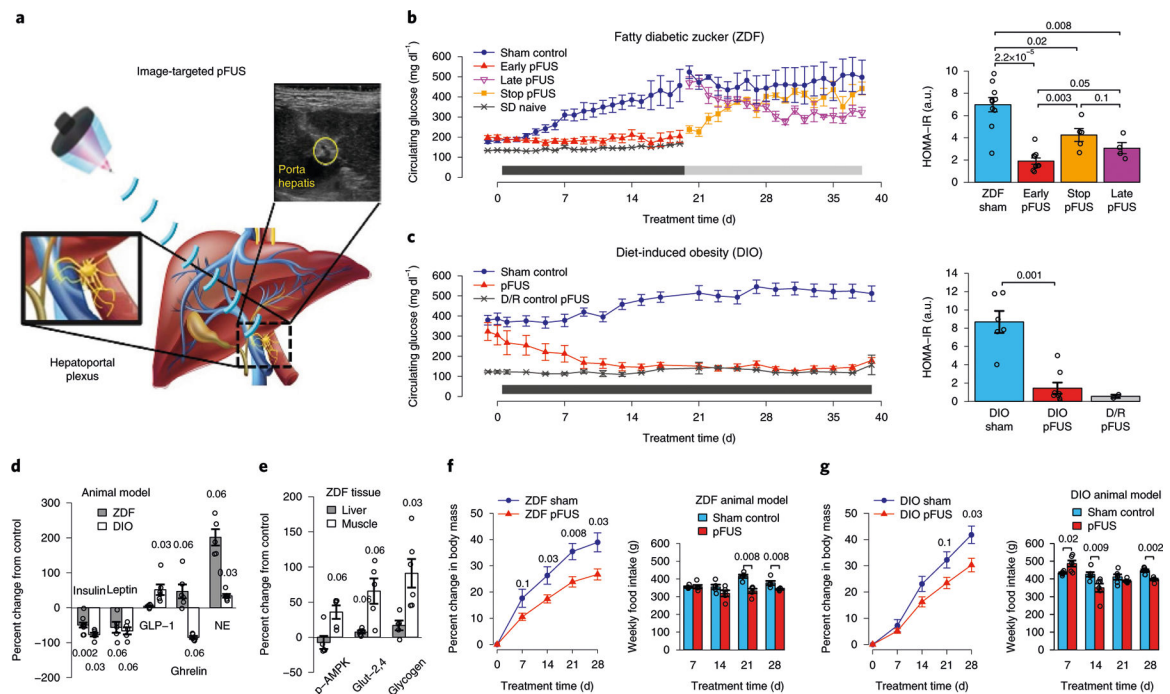


Fig. 1 | Daily ultrasound stimulation of the liver–brain neural pathway prevents or reverses the onset of hyperglycaemia in multiple animal models of T2D.

a. A schematic and ultrasound image of the pFUS^{15,16,18} target at the porta hepatis, known to contain the hepatoportal glucose sensing system^{25,26,28–34}. Neurons at this location are known to communicate through the IML and NTS, and modulate specific hypothalamic metabolic nuclei^{45–48,114,115}. **b,c.** Daily (3 min) pFUS treatment was performed and shown to prevent or reverse the onset of hyperglycaemia in multiple animal models of T2D. **b.** Left: daily non-fasted circulating glucose measurements from ZDF animals after daily pFUS (red; $n = 15$; early pFUS) or sham control (blue; $n = 20$; sham control) treatment versus naïve SD controls (grey; $n = 4$; SD naïve) over 20 d (horizontal black bar; age 55 to 75 d of ZDF cohorts). Cross-over experiments were then performed between the previously stimulated cohort (yellow; $n = 5$; stop pFUS) and previous sham cohort (pink; $n = 5$; late pFUS), and the sham control treatment was maintained in a subset of animals (blue; $n = 5$; sham control) for an additional 20 d (horizontal grey bar; age 76 to 95 d of ZDF cohorts). Right: terminal (age 95 d) HOMA-IR scores for animals randomly assigned from the sham control ($n = 10$), early pFUS ($n = 10$), late pFUS ($n = 4$) and stop pFUS ($n = 5$) cohorts. **c.** Left: daily blood glucose measurements in DIO animals undergoing daily pFUS (red; $n = 8$) or sham control (blue; $n = 9$) pFUS treatment for 40 d. Right: terminal (day 40) HOMA-IR scores for animals randomly assigned from the sham control ($n = 6$), pFUS ($n = 8$) and diet resistant (D/R) control (+pFUS) cohorts. **d.** The percent change in the concentration of circulating markers (insulin, leptin, GLP-1, ghrelin and NE) between stimulated ($n = 5$; day 20) and sham control ($n = 5$; day 20) ZDF rats, and stimulated ($n = 5$; day 40) and sham control ($n = 5$; day 40) DIO rats. **e.** Percent change in activated AMPK, GLUT2 in hepatic and GLUT4 in skeletal muscle tissue, and glycogen from the ZDF rats following daily stimulation between stimulated ($n = 5$) and sham control ($n = 5$) cohorts after 20 d treatment. **f.** Left: overall rate of weight gain in pFUS-treated ($n = 5$; red line) ZDF rats as compared

to their sham-stimulated littermates ($n = 5$; blue line). Right: weekly food intake observed in the pFUS ($n = 5$) and sham-stimulated ($n = 5$) ZDF cohorts. **g**, Left: overall rate of weight gain in pFUS-treated ($n = 5$; red line) DIO rats as compared to their sham-stimulated littermates ($n = 5$; blue line). Right: weekly food intake observed in pFUS- ($n = 6$) and sham- ($n = 6$) stimulated DIO cohorts. All P values shown were derived using nonparametric Wilcoxon rank-sum test (two-sided). Data shown are mean \pm s.e.m. The schematic images contained in the manuscript and supplemental data were custom drawn around the istock 36250716 picture of the liver.

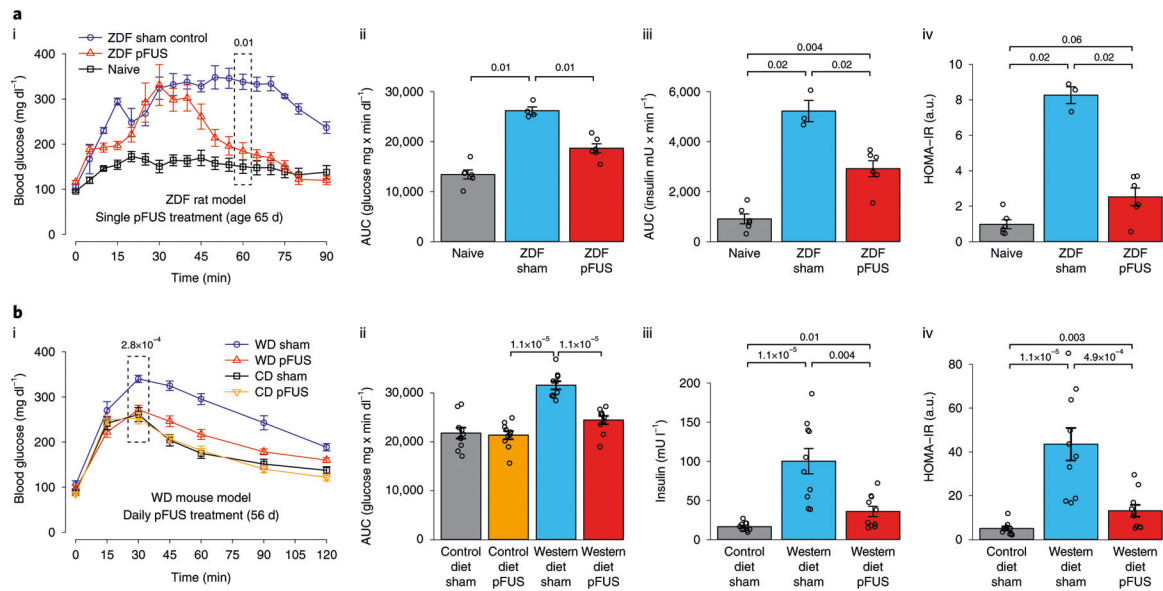


Fig. 2 | pFUS improves glucose tolerance after acute and chronic stimulation exposure.

a, A single pFUS stimulus was applied immediately before OGTT to fasted ZDF rats at age 65 d with no previous treatment. **(i)** The single stimulus improved glucose tolerance, resulting in an observable decrease in blood glucose 45 min following oral glucose administration as compared with sham control rats. At 60 min after oral glucose administration (2 g kg^{-1}), pFUS-treated animals presented significantly lower blood glucose levels ($170 \pm 8.8 \text{ mg dl}^{-1}$), within the expected range for a normal rat following glucose ingestion ($n = 6$ for ZDF-pFUS and naive; $n = 4$ for ZDF sham). **(ii)** Calculation of incremental AUCs showed a significant reduction in glucose as compared with sham-stimulated controls. **(iii)** Insulin measurements taken during GTT demonstrate a significant reduction in the pFUS-stimulated group compared with controls (AUC). **(iv)** These results suggest a notable improvement in whole-body insulin sensitivity after the single treatment, as determined by HOMA-IR scoring. **b**, Daily hepatic pFUS resulted in a sustained improvement in glucose tolerance and attenuated insulin resistance in WD mice after 56 d of treatment. **(i)** Hepatic pFUS significantly reduced peak glucose response in the obese mice (WD-pFUS) compared with sham-stimulated mice (WD sham; 30 min, $n = 10$ per group). There was no change in glucose tolerance in cohorts receiving the control (normal) diet (CD). **(ii)** A significant reduction in AUC was observed in WD-pFUS mice as compared with WD sham mice. **(iii)** pFUS measurements (112 d) also showed a significant reduction in insulin levels in the stimulated versus the sham control. **(iv)** The pFUS treatment also resulted in a significant reduction in insulin resistance as measured by HOMA-IR score in WD animals as compared with the sham controls. Dashed rectangles in **a(i)** and **b(i)** show the data points used for the statistical test. All P values shown were derived using nonparametric Wilcoxon rank-sum test (two-sided). Data shown are mean \pm s.e.m.

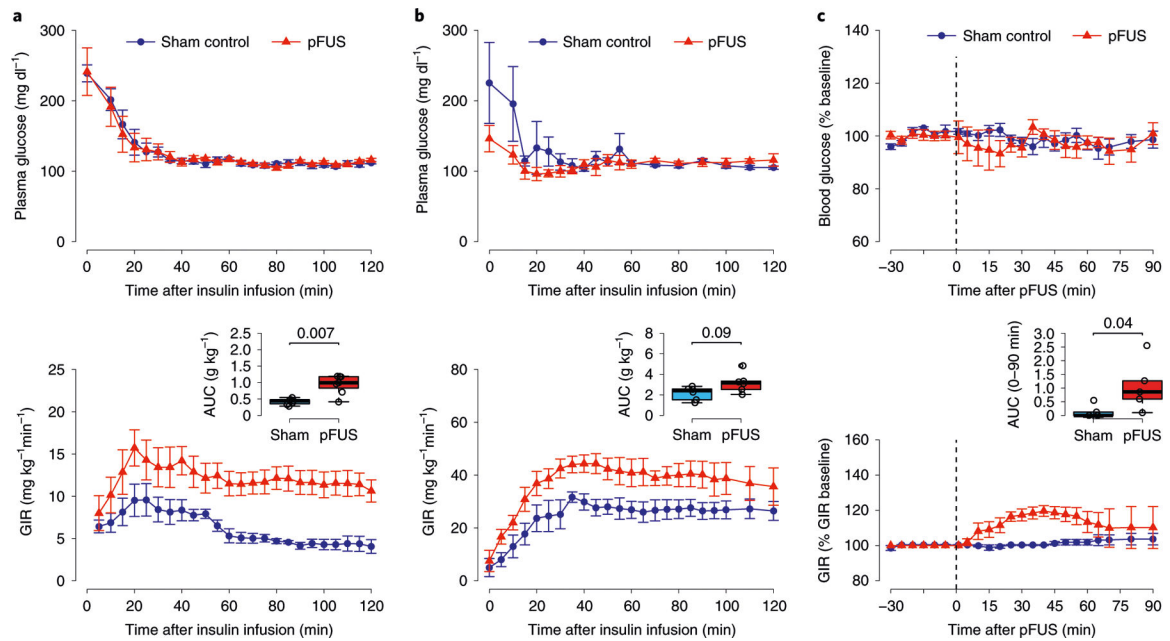


Fig. 3 | pFUS alters glucose kinetics in small- and large-animal models.

a, HEC was performed 1 d following 3 consecutive days of pFUS treatment in the DIO rat model ($25 \text{ mU kg}^{-1} \text{ min}^{-1}$ for the first 30 min and $15 \text{ mU kg}^{-1} \text{ min}^{-1}$ for the remaining 90 min continuous insulin infusion rate). Top: plasma glucose levels during HEC in pFUS (red; $n = 7$) and sham-treated (blue; $n = 7$) DIO rats. Bottom: the corresponding GIR. Inset: the GIR AUC at steady state ($n = 7$ per group; boxplot presents the data median, first and third quartiles, and the whiskers are $1.5 \times$ interquartile range (IQR); if no points exceeded $1.5 \times$ IQR distance, then the whiskers are simply the minimum and maximum values). **b**, HEC was performed 1 d following 3 consecutive days of pFUS treatment in the STZ-induced T1D rat model ($25 \text{ mU kg}^{-1} \text{ min}^{-1}$ for the first 30 min and $10 \text{ mU kg}^{-1} \text{ min}^{-1}$ for the remaining 90 min continuous insulin infusion rate; 110 mg ml^{-1} target plasma glucose). Top: plasma glucose levels during HEC in pFUS (red; $n = 6$) and sham-treated (blue; $n = 6$) STZ-induced T1D rats. Bottom: the corresponding GIR. Inset: the GIR AUC at steady state ($n = 6$ per group; boxplot presents the data quartiles, and whiskers are the minimum and maximum values, unless value exceeds $1.5 \times$ IQR distance). **c**, Euglycaemic clamps were performed in healthy swine at $0.5 \text{ mU kg}^{-1} \text{ min}^{-1}$ continuous insulin infusion rate. Time 0 (dashed vertical line) denotes the start time of the 3 min pFUS stimulus applied to the porta hepatis using ultrasound image targeting (Extended Data Fig. 4) and using a commercial clinical ultrasound system (LOGIQ E10 with C1-6 abdominal probe). Top: pFUS was applied after achieving $<10\%$ variation in blood glucose levels, which were then monitored and clamped at 110 mg dl^{-1} during both pFUS- (red) and sham-control (blue) treatments. Bottom: time course of the acute effects of pFUS during clamp on GIR in both pFUS- (red) and sham-control (blue) cohorts ($n = 5$; each animal tested with both sham and pFUS). Inset: the GIR AUC at steady state ($n = 5$ per group; boxplot presents the data quartiles, and whiskers are the minimum and maximum values, unless value exceeds $1.5 \times$ IQR distance). All P values shown were derived using nonparametric Wilcoxon rank-sum test (two-sided). Data shown are mean \pm s.e.m.

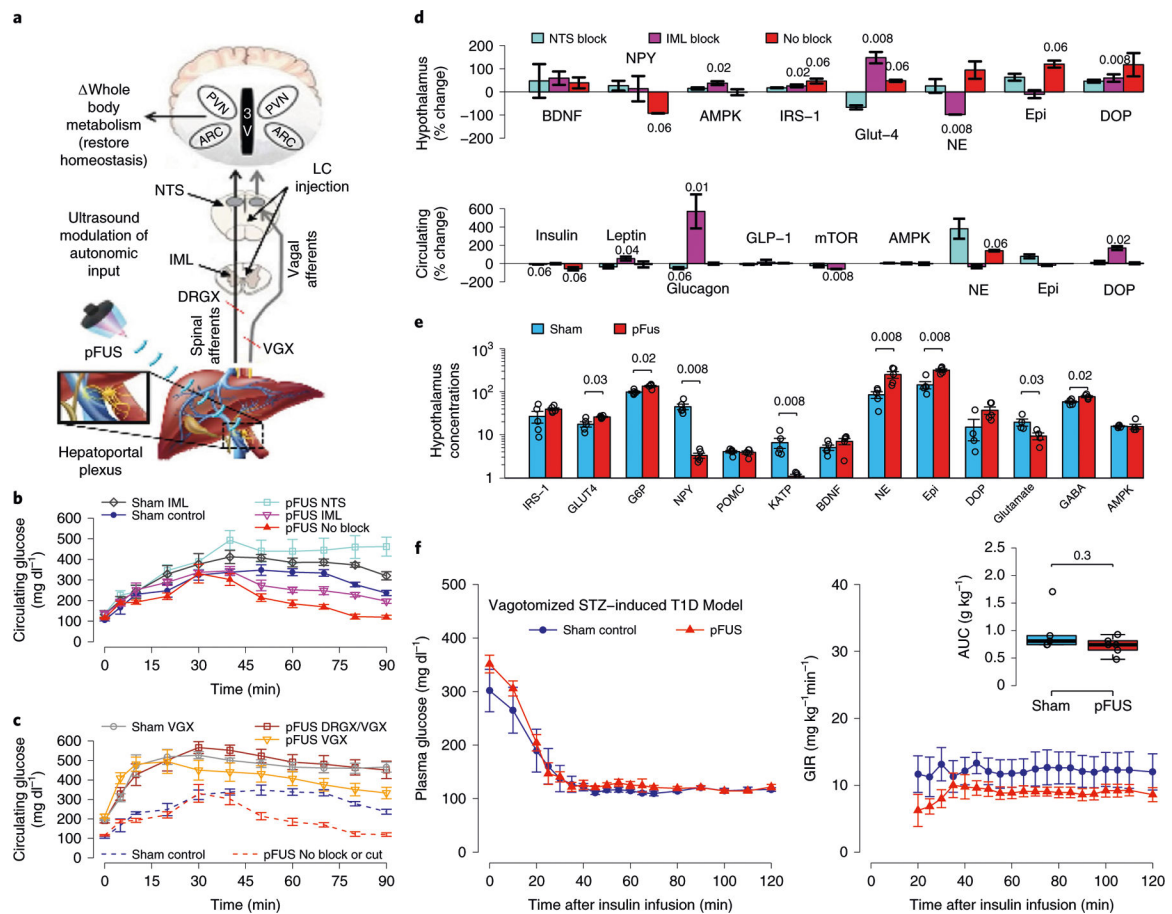


Fig. 4 | pFUS effect is dependent on liver-brain nerve pathways.

a, Schematic of the nerves enabling communication between the hepatoportal plexus and metabolic nuclei in the hypothalamus (for example, the ARC and the PVN)^{29,40,41,45–49,52,58,62,107,114,115,139,140}, and location of dissections (red lines) and lidocaine (LC) injections performed (details in Methods). **b**, Microinjection of lidocaine into the NTS abolished the effects of pFUS stimulus on blood glucose during GTT (ZDFs; light blue squares; $n = 4$), as compared with pFUS alone (red triangles; $n = 6$). In contrast, lidocaine injection into the IML nucleus attenuated, but did not completely block the effects of pFUS (pink inverted triangles; $n = 5$). Lidocaine injection at the IML (black diamonds; $n = 4$) resulted in increased glucose excursion (AUC: 31,443) compared with ZDF sham-treated animals without block (AUC: 26,087; $P < 0.057$; $n = 4$). No sham NTS experiments were performed. **c**, Hepatic vagotomy and dorsal root ganglion resection at the T1 vertebrae (VGX/DRGX) abolished the effects of pFUS on blood glucose during GTT in ZDFs (brown boxes; $n = 4$), as compared with pFUS alone (red dashed line). In contrast, VGX alone attenuated, but did not completely block the effects of pFUS (yellow inverted triangles; $n = 4$; AUC: 37,336 vs grey circles; $n = 5$; AUC: 42,074; $P < 0.19$). Hepatic vagotomy in the absence of pFUS (grey circles) led to an increase in circulating glucose as compared with standard ZDF sham-treated animals (dark blue dashed line; replotted from 4.C. for comparison). **d**, Top: lidocaine in the NTS abolished the effects pFUS on hypothalamic NPY, IRS, GLUT4 and NE. No significant effect was seen with NTS inhibition on BDNF

and AMPK (light blue bar ($n = 4$) versus red bars ($n = 4$)). In contrast, lidocaine in the IML abolished the effects of pFUS on epinephrine (Epi) and NE, but attenuated the effects of pFUS on hypothalamic NPY, IRS and dopamine (DOP) (pink bars ($n = 8$) versus red bars ($n = 4$)). Interestingly, augmented effects on AMPK and GLUT4 were observed with pFUS stimulus following IML inhibition. No significant effect was seen with IML inhibition on BDNF. Bottom: lidocaine in the NTS produced a significant increase in circulating NE (light blue bars ($n = 5$) vs red bars ($n = 5$)). In contrast, administration into the IML had no effect on NE, but produced a significant increase in glucagon release (pink bars ($n = 8$) vs red bars ($n = 5$)). **e**, Changes in hypothalamic nutrient sensing, insulin signalling and neurotransmitters for pFUS-treated ($n = 5$) and sham controls ($n = 5$) after 20 d of treatment (glucose values for these animals previously reported in Fig. 1b(left)). Concentrations are in ng mg^{-1} , except for BDNF (pg mg^{-1}) and for glutamate, GABA, AMPK (nmol mg^{-1}). **f**, HEC was performed 1 d following 3 d of pFUS in the STZ-induced T1D model 14 d after hepatic vagotomy. Left: plasma glucose levels during HEC in pFUS- (red; $n = 6$) and sham-treated (blue; $n = 5$) vagotomized STZ-induced T1D rats. Right: the corresponding GIR. Inset: the GIR AUC for the steady state component of the clamp (NS, not significant; boxplot presents the data median, first and third quartiles, and the whiskers are $1.5 \times$ IQR. If no points exceed $1.5 \times$ IQR distance, then the whiskers are simply the minimum and maximum values). All P values shown were derived using nonparametric Wilcoxon rank-sum test (two-sided). Data shown are mean \pm s.e.m. The schematic images contained in the manuscript and supplemental data were custom drawn around the istock 362507163 picture of the liver.

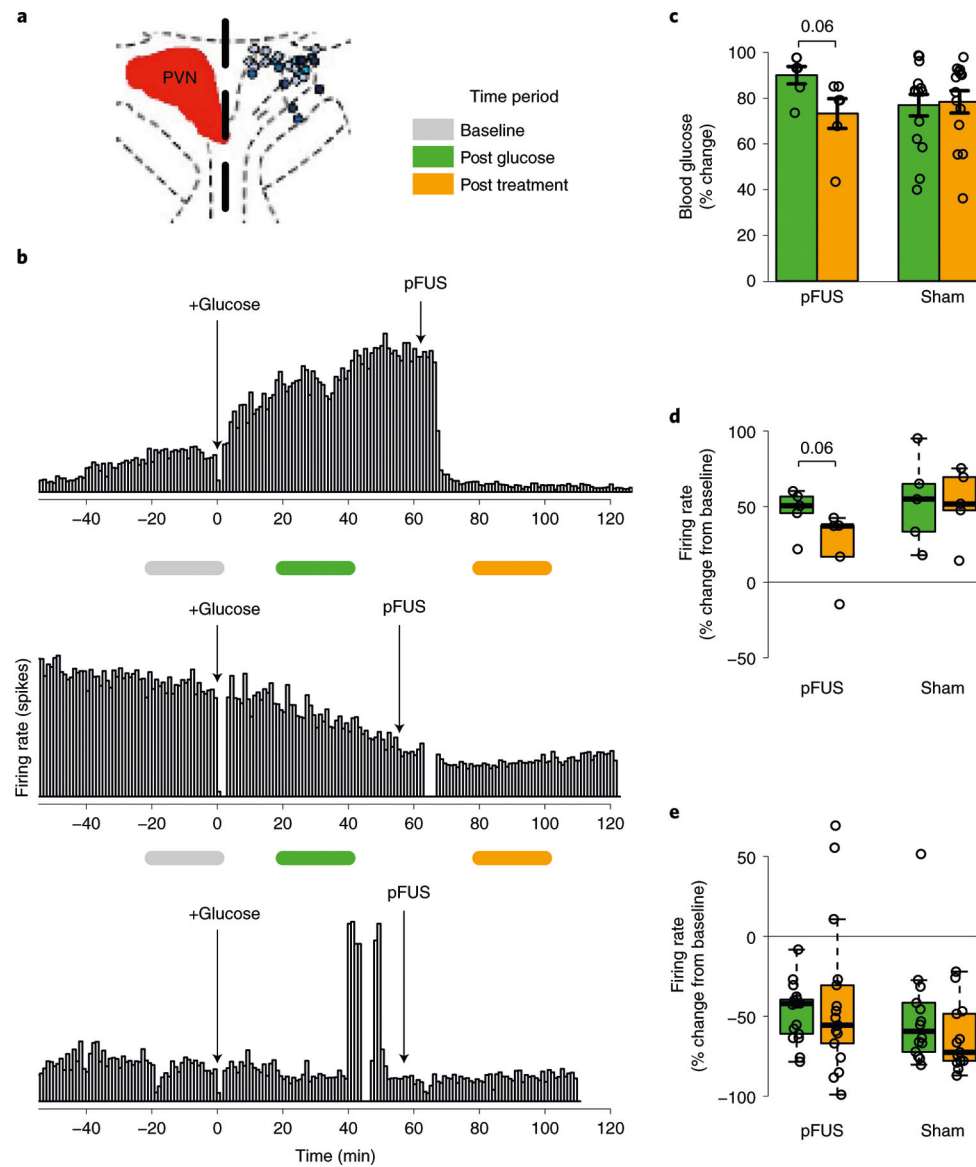


Fig. 5 | Hepatoportal pFUS modulates firing rates of hypothalamic GE neurons.
a, Schematic position of electrodes inserted into the PVN to measure single-neuron firing rates in response to glucose injection (bold dashed line represents the midline in the hypothalamus). Coloured circles represent depths of the inserted electrodes (within the 2D picture): grey/blue, 2.12 mm; blue, 1.88 mm; dark blue, 1.6 mm; light blue, 1.4 mm. **b**, Example firing rates (spikes) from GE (top), glucose-inhibited (middle) or glucose-insensitive (bottom) neurons before glucose injection (baseline), after glucose injection and after pFUS. **c**, Final blood glucose measurements were increased compared with the baseline in both pFUS-stimulated (pFUS $n = 6$) and non-stimulated (sham $n = 14$) animals. However, pFUS was associated with a decrease in circulating blood glucose compared with the sham treatment. **d**, GE neurons showed elevated firing rates post-glucose injection compared with the baseline, and pFUS resulted in a significant change in firing rate in these neurons (pFUS $n = 5$). However, in the absence of pFUS, GE neurons maintained an elevated firing rate

compared with the baseline throughout the experiment (sham $n = 5$; boxplot presents the data median, first and third quartiles, and the whiskers are $1.5 \times \text{IQR}$. If no points exceed $1.5 \times \text{IQR}$ distance, then the whiskers are simply the minimum and maximum values). **e**, GI neurons showed a significant change from baseline post-glucose injection. However, pFUS did not change GI firing rates ($n = 16$; NS; boxplot presents the data quartiles, and whiskers are the minimum and maximum values, unless value exceeds $1.5 \times \text{IQR}$). All P values shown were derived using nonparametric Wilcoxon rank-sum test (two-sided). Data shown are mean \pm s.e.m.

Author Manuscript

Author Manuscript

Author Manuscript

Author Manuscript

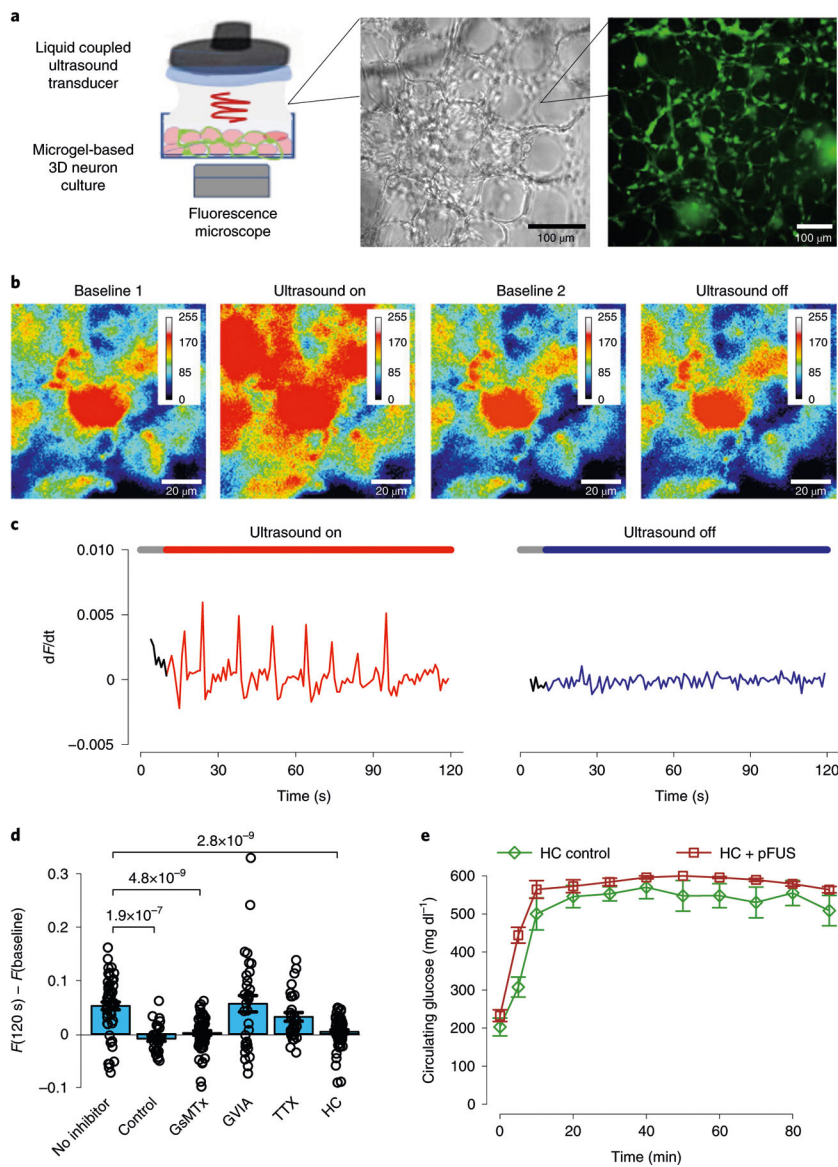


Fig. 6 | pFUS effect is dependent on the activity of mechanically activated ion channels in both in vitro and in vivo models.

a, Schematic of the 3D peripheral neuron culture system, and experimental setup (left; details in Methods) used to capture images of DRG neuron cells before and after pFUS stimulation. The DRG neuron culture has previously been shown^{18,79} to create active axonal networks through the pores formed between hydrogel particles (bright-field (middle) and fluorescence (right) images are shown). **b**, The zoomed-in fluorescence images show a time lapse of calcium (Ca^{2+}) imaging during pFUS stimulation (colour bars, fluorescence intensity units). pFUS stimulation was turned on at 10 s (ultrasound on) following a brief period of time for collecting baseline images (baseline 1) and turned off again at 120 s. The ultrasound remained off for 2 min before retaking a second baseline (baseline 2) and measurement period (ultrasound off). Calcium concentrations of DRG neurons increased after ultrasound stimulation and returned to baseline levels upon pFUS cessation. **c**, pFUS excitation of DRG neurons led to large changes in Ca^{2+} -

dependent fluorescence (F). The rate of change, dF/dt , remained small without application of ultrasound stimulus (ultrasound off) compared with the significant dF/dt increases shown during pFUS stimulation (ultrasound on; at 0.83 MPa peak-positive pressure without any ion-channel blocker added to the culture with $N > 30$ cells per condition). **d**, Observed fluorescence change before/after ultrasound stimulation using multiple ion-channel blockers ($N > 30$ cells per condition). TTX is a specific inhibitor of voltage-gated sodium channels involved in action potential propagation, ω -conotoxin-GVIA is an N -type Ca^{2+} channel inhibitor, and HC-030031 (HC) is a sensitive TRPA1 channel inhibitor. When piezo- or TRP-family blockers GsMTx and HC-030031 were added to the culture, pFUS-induced activity was significantly suppressed. **e**, HC-030031 is shown to inhibit the pFUS effect on glucose in vivo when locally injected at the porta hepatis in ZDF rats ($n = 4$ per group; GTT performed after overnight fast at age 65 d). The GTT was performed in both pFUS-treated (HC + pFUS) and control animals given the HC injection but no pFUS (HC sham control). Unlike ZDF rats without HC treatment (Fig. 2a), no statistical difference in circulating blood glucose was observed in animals treated with the TRPA1 blocker. All P values shown were derived using nonparametric Wilcoxon rank-sum test (two-sided). Data shown are mean \pm s.e.m.

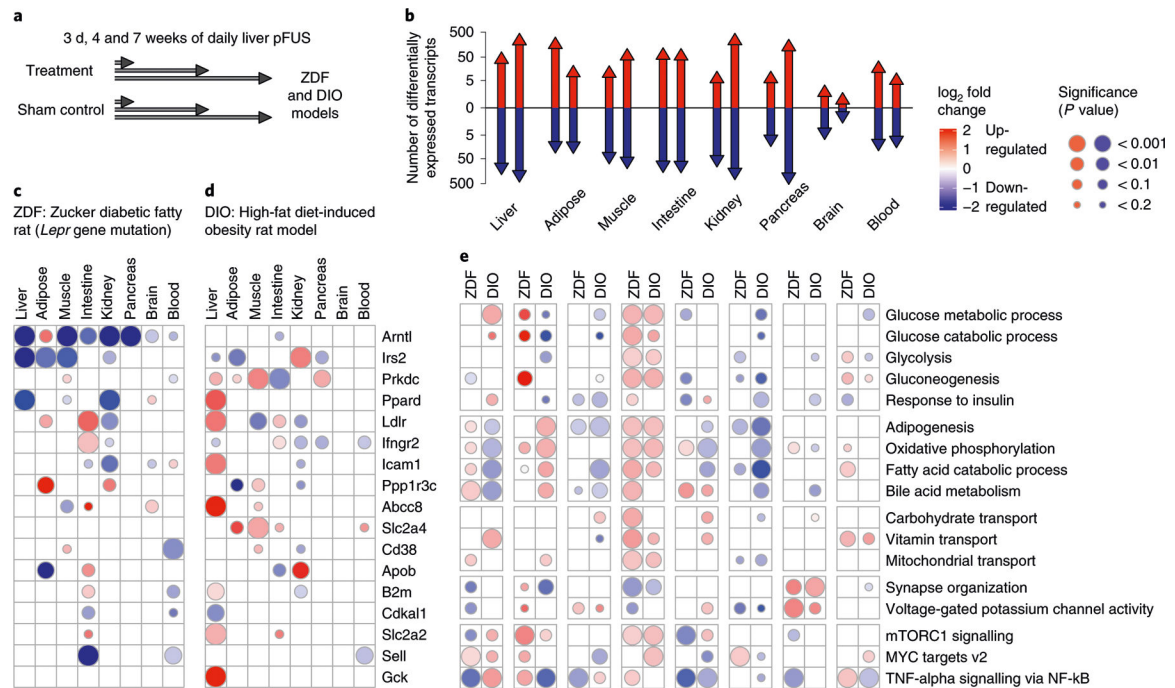


Fig. 7 |. Tissue-specific transcriptomic and metabolomic changes after pFUS treatment of multiple animal models of T2D.

a, Genetic (ZDF) and DIO animal models underwent 7 weeks of daily pFUS stimulation along with sham-treated control animals ($n = 5$ per treatment group). **b**, The number of differential RNA transcripts that are upregulated (red arrows) and downregulated (blue arrows) across eight tissues between the pFUS-stimulated vs sham controls in both ZDF and DIO animal models. **c,d**, The top diabetes genes that are significantly upregulated (red) or downregulated (blue) across eight tissues in ZDF (**c**) and DIO (**d**) animal models. The size of each circle represents the P value of differentiation between the pFUS-stimulated group ($n = 5$) vs sham-treated controls ($n = 5$). **e**, Biological processes found to be significant (familywise error rate $P < 0.1$) from gene set enrichment analysis across tissues in the ZDF and DIO animal models. Biological processes are highlighted as being activated (red) or repressed (blue) if the median value of the \log_2 -transformed fold changes for the set of genes was positive or negative, respectively. The biological processes include glucose metabolic process (GO:0006006), glucose catabolic process (GO:0006007), glycolysis (broad hallmark), gluconeogenesis (Reactome R-HSA-70263), response to insulin (GO:0032868), adipogenesis (broad hallmark), oxidative phosphorylation (broad hallmark), fatty acid catabolic process (GO:0009062), bile acid metabolism (Broad Hallmark), carbohydrate transport (GO:0008643), vitamin transport (GO:0051180), mitochondrial transport (GO:0006839), synapse organization (GO:0050808), voltage-gated potassium channel activity (GO:0005244), mTORC1 signalling (broad hallmark), MYC targets v2 (broad hallmark) and TNF-alpha signalling via NF-kB (broad hallmark). P values were derived using the Wald test for transcriptomic data (except for **b** in which $P < 0.1$ using the Wald test and corrected for multiple testing using the Benjamini and Hochberg method).

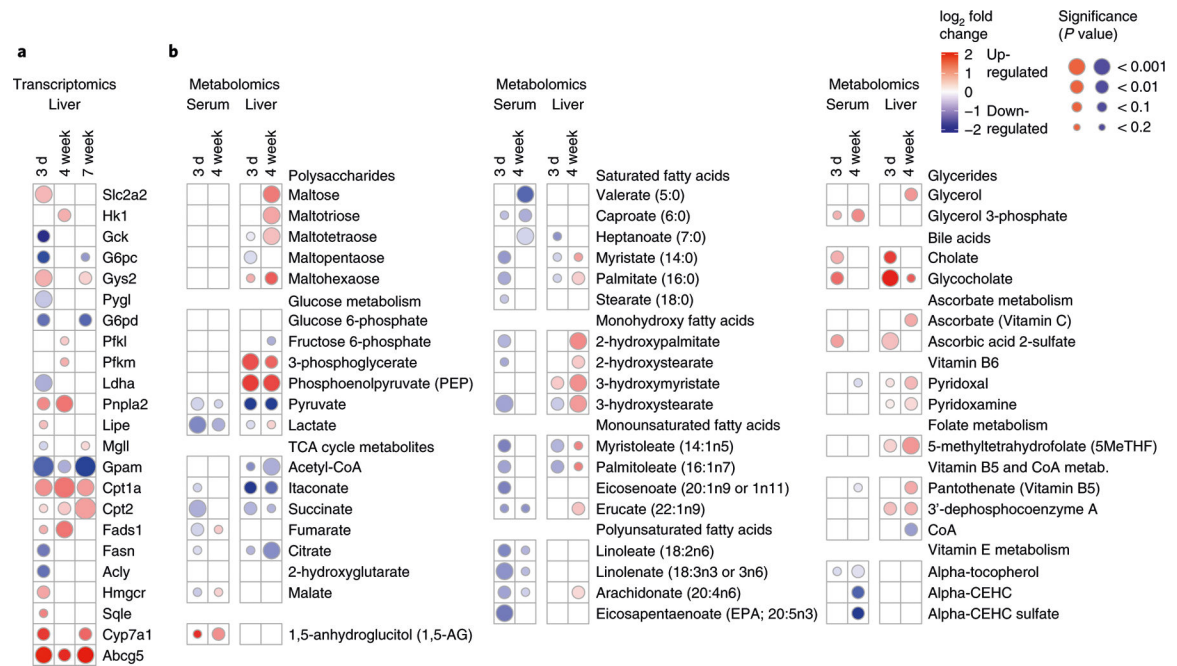


Fig. 8 | Tissue-specific transcriptomic and metabolomic changes at multiple timepoints during 7 weeks of daily pFUS treatment of multiple animal models of T2D.

a. Differential RNA transcripts from liver of ZDF animals undergoing 3 d, 4 weeks or 7 weeks of daily pFUS stimulation vs sham controls. The protein encoded by these differentially expressed genes are presented in the schematic diagrams in Supplementary Figs. 13–15. **b.** The changes in metabolites in blood serum or liver tissue at 3 d and 4 weeks between ultrasound treatment vs controls. The size of each circle represents the P value of differentiation between the pFUS-stimulated group ($n = 5$) vs sham controls ($n = 5$). The colour intensity and size of the circle represent the degree of being upregulated (red) or downregulated (blue). For differential transcript analysis, P values shown were derived from the Wald test. For metabolomic data, P values were derived using nonparametric Wilcoxon rank-sum test (two-sided).